Atomic scale simulations of Pt and Au adatom diffusion and interlayer transport

Abid Ali

Faculty of Physical Sciences
University of Iceland
2022

Atomic scale simulations of Pt and Au adatom diffusion and interlayer transport

Abid Ali

Dissertation submitted in partial fulfillment of a
Philosophiae Doctor degree in Chemistry

Advisor
Prof. Hannes Jónsson

PhD Committee
Prof. Hannes Jónsson
Prof. Egill Skúlason
Dr. Elvar Örn Jónsson

Opponents
Prof. Nigel Mason
Dr. Gísli Hólmar Jóhannesson

Faculty of Physical Sciences
School of Engineering and Natural Sciences
University of Iceland
Reykjavik, May 2022

Atomic scale simulations of Pt and Au adatom diffusion and interlayer transport
Modeling surface diffusion and growth
Dissertation submitted in partial fulfillment of a *Philosophiae Doctor* degree in Chemistry

Faculty of Physical Sciences
School of Engineering and Natural Sciences
University of Iceland
Duhangi 5
107, Reykjavik
Iceland

Telephone: 525-4000

Bibliographic information:
Abid Ali, 2022, *Atomic scale simulations of Pt and Au adatom diffusion and interlayer transport*, PhD dissertation, Faculty of Physical Sciences, University of Iceland, 110 pp.

ISBN XXISBN

Printing: XXPrinter
Reykjavik, Iceland, May 2022

Abstract

The research described in this thesis is part of a network project involving the growth of metal nanostructures on surfaces of solids, a Horizon 2020 project titled ELENA. The part of the project described here involved the use of various approaches including density functional theory (DFT), semi-empirical potential functions, and machine learned Gaussian approximation potentials (GAP) for determining the mechanism of adatom migration on surfaces of solids and interlayer transport. Minimum energy paths for the various elementary processes were calculated using the nudged elastic band method in order to identify the transition mechanisms and evaluate the corresponding activation energy. Particular focus was on processes involving the descent of adatoms that land on top of a growing close packed layer on platinum and gold crystals. These are the key transitions determining whether the surface grows layer-by-layer or forms three-dimensional islands. The optimal mechanism for such interlayer transport was identified taking into account the surface morphology, in particular the presence of kinks on the step edges. Also, calculations of Au adatom diffusion on the Si(100) surface were carried out. While exploratory calculations on all these systems were first carried out using semi-empirical potential functions, the principal results presented are based on more accurate DFT calculations that were carried out subsequently using the PBEsol electron density functional.

The principal result for the Pt/Pt(111) and Au/Au(111) systems is that downstepping occurs most readily when there is a kink on the step edge, and the preferred mechanism involves a concerted two atom process that places an atom near but not into the kink sites. This is important for explaining the re-entrant layer-by-layer growth which has been experimentally observed previously for Pt(111) growth. The calculations for Au/Au(111) presented here predict similar behavior for the growth of the Au(111) surface. The importance of choosing a single reference point for the energy of the adatom, here chosen to be the adatom on an extended flat surface, is demonstrated. Also, two effects are identified leading to a depletion zone near the step edges, which has previously been observed experimentally.

The calculations of a Au adatom on the Si(100)-2×1 surface reveal an unusual diffusion path. While the optimal binding site is in between the Si dimer rows, as has been deduced previously from experimental measurements, the optimal diffusion path involves promotion of the adatom to higher energy binding sites on top of a dimer row and then rapid skidding along the row before the adatom drops back down in between dimer rows to a low energy site. As a result, dimers of Au adatoms and possibly larger adatom clusters are predicted to form on top of dimer rows, rather than in between rows. On the basis of the calculations of binding sites and migration paths, kinetic Monte Carlo simulations of long time evolution were carried out and an effective activation energy for diffusion evaluated.

Útdráttur

Here, the Icelandic version of the abstract will be placed.

Dedication

This thesis is dedicated to my father, Allah Bachayo Channa, my sister, Najma Kawish Channa, and specially my mother, Mst. PK.

Preface

This thesis is submitted in candidacy for a Ph.D. degree in Chemistry from the University of Iceland. The work has been conducted between September 2017 and February 2022 at Faculty of Physical Sciences, Science Institute supervised by Prof. Hannes Jónsson.

This work is part of a European Marie Sklodowska-Curie Innovative Training Network (MSCA-ITN) named **ELENA** - Low Energy **ELE**ctron driven chemistry for the advantage of emerging **NA**no-fabrication methods `https://elena.hi.is`. This work has received funding from the European Union's Horizon 2020 research and innovation programme under the Marie Sklodowska Curie grant agreement No. 722149.

Table of Contents

List of Figures

List of Original Articles

I: Abid Ali, Vilhjálmur Ásgeirsson, Grace S. Sun, Hannes Jónsson. Mechanism of Low Temperature, Re-entrant 2D Growth of Pt(111). *To be submitted to Nanoscale.*

II: Abid Ali, Hannes Jónsson. Mechanism of Interlayer Transport on a Growing Au(111) Surface: 2D vs. 3D Growth. *Surfaces and Interfaces, 31(2022), 101944.*

III: Alejandro Peña-Torres, Abid Ali, Michail Stamatakis, Hannes Jónsson. Indirect Mechanism of Au adatom Diffusion on the Si(100)2$\times$1 surface. *Physical Review B, 105, 205411 (2022)*

Abbreviations

ELENA Low energy ELEctron driven chemistry for the advantage of emerging NAno-fabrication techniques

FEBID Focused electron beam induced deposition

DFT Density functional theory

EMT Effective medium theory

NEB Nudged elastic band

FCC Face centered cubic

HCP Hexagonal closed packed

MEP Minimum energy path

PES Potential energy surface

LDA Local density approximation

GGA Generalized gradient approximation

IS Initial state

FS Final state

TS Transition state

TST Transition state theory

PBE Perdew-Burke-Eernzerhof

PBEsol Perdew-Burke-Eernzerhof functional for solids

HF Hartree-Fock

BE Binding energy

PE Potential energy

KE Kinetic energy

STM Scanning tunneling microscope

AFM Atomic force microscopy

RLS Rate limiting step

EAM Embedded atom method

cNEB Climbing-image nudged elastic band

VASP	Vienna ab-initio simulation package
ASE	Atomic simulation environment
KS	Kohn-Sham
aKMC	Adaptive kinetic Monte Carlo
ES	Ehrlich-Schwoebel
LAMMPS	Large-scale molecular massively parallel simulator
MD	Molecular dynamics
E_a	Activation energy
k_0	Rate constant
E_{coh}	Cohesive energy
E_{xc}	Exchange correlation energy
ψ	Wave function
$\widehat{H}$	Hamiltonian operator
HK	Hohenberg-Kohn
K_B	Boltzmann constant
a_0	Lattice constant
GAP	Gaussian approximation potential
BDR	Between dimer rows
TDR	Top of dimer row
ADP	Angular dependent potential

Acknowledgments

I would like to express my special thanks to my thesis supervisor Prof. Hannes Jónsson for his guidance, encouragement, and support throughout this project. I would like to thank Prof. Egill Skúlason and Dr. Elvar Örn Jónsson for serving as Ph.D. committee members. I would like to thank Dr. Vilhjálmur Ásgeirsson who has been a mentor for me.

A special acknowledging goes to Prof. Nigel Mason (University of Kent, UK) and Dr. Gísli Hólmar Jóhannesson (Keilir Academy, Iceland) for agreeing to serve as opponents of my Ph.D. thesis and defence.

My special thanks to Prof. Oddur Ingólfsson (University of Iceland) as the coordinator our Marie Curie "ELENA" network for helpful discussions on my progress and for organizing training schools, conferences, secondments, and industrial visits in the network. I would like to thank Prof. Nigel Mason (University of Kent) for his guidance and academic support during my four month (secondment) visit at University of Kent, UK. It is my pleasure to thank Brynja Dís Guðmundsdóttir (**ELENA** project manager at University of Iceland) for providing guidance on the submission of my monthly and yearly work progress reports, deliverables, etc., and for making arrangements for my travel throughout the **ELENA** project.

I am also thankful to all the members of **ELENA** consortium, Ali Kamali, Reza Tafrishi, Rene Alejandro Cartaya, Maria Pintea, Ching-Chung Huang, Elif Bilgilisoy, Cristiano Glessi, Hoang Linh Le, Aya Mahgoub, Jakub Jurczyk, Najmeh Sadegh, Ashish Rathore, Dominik Marko, Po-Yuan Shih for giving wonderful time during ELENA meetings and specially thanks to my Ph.D supervisor Prof. Hannes Jónsson for giving me opportunity to be a member of the ELENA consortium.

I would like to thank to all my colleagues in VR-III for their good company during my Ph.D. years, both present and former members, especially Dr. Javed Hussain, Dr. Donato Fantauzzi, Dr. Younes Abghoui, Dr. Maxime Van den Bossche, Dr. Asmus Ougaard Dohn, Dr. Ming Geng, Dr. Kuber Singh Rawat, and Dr. Aleksie V.Ivanov. I also thank to Dr. Hemanadhan Myneni, Siri Harsha Pulumati, Narges Atrak, André P. Wark, Barði Benediktsson, Benedikt Orri Birgisson, Dr. Gianluca Levi, Dr. Björn Kirchhoff, Rohit Goswami, Dr. Kusse Sukuta Bersha, Yorick Leonard, Mohammad Hussein Ali Badarneh, and Robert Brevik for having wonderful times in VR-III building. I also would like to thank Dr. Alejandro Pena Torres for helping me in the project on Au adatom diffusion on the Si(100)-2x1 surface.

1 Introduction

1.1 Introduction and motivation

The ordering of atoms to form a crystal, a transformation from a disordered phase (typically liquid or gas) to a highly regular sequence is interesting in many ways. In various technological applications it is important to obtain the right growth mechanism, in some cases layer-by-layer growth, but in others the formation of nanoscale islands. An understanding of the processes that determine the morphology of the growing surface and the way external conditions such as temperature and growth rate is, therefore, of significant importance.

During crystal growth, atoms typically land on flat facets of the surface and diffuse around until they get attracted to steps. If the atoms can diffuse along the step edge they can get attracted to kinks on the step. Those are the natural sites for layer-by-layer growth as they offer the highest coordination and therefore largest binding energy. But, this growth scheme only holds if the adatoms have enough mobility (Jonsson, 2000). In the past few decades there has been rapid progress in atomic-scale crystal growth studies due, in particular, to the development of powerful experimental tools for the studies of surfaces. These include the scanning tunneling microscopy (STM) (Brune, 1998) and scattering of He atoms (Poelsema and Comsa, 1989) and electrons (Van Hove et al., 1983) as they provide valuable information regarding the morphology of the surface during the growth process. Field ion microscopy (FIM) experiments have also given important information about surface diffusion processes.

The STM was developed in the 1990s and the inventors, Binnig and Rohrer, received the Nobel prize in Physics for its development in 1986. It provides the most detailed and direct information about surface morphology. Images of low index surfaces, such as (100) and (111), show that terraces are separated by steps that are typically not straight but include kinks. STM images can also show vacancies representing missing surface atoms (Pimpinelli and Villain, 1999). Most often a system under study is quenched to low temperature for STM imaging in between growth periods at elevated temperature. The atom and electron scattering approaches can, however, be applied during growth and probe the surface on a larger length scale. Higher spatial resolution can be obtained using scanning electron microscopy (SEM) as it produces an image of a smaller region of the surface. Atomic force microscopy (AFM) is also a powerful tool in order to study the morphology of a growing surface.

Crystal growth from a solution or melt is difficult to measure, but growth from vapor can be monitored more easily. Fig. 1.1 shows an image of a Si(001)-2x1 surface grown by molecular beam epitaxy (MBE).
The principle behind MBE is quite simple. A beam of atoms or molecules is directed to a solid surface under high vacuum conditions. In colliding with the surface, the atoms loose their kinetic energy and adsorb on the surface, forming so-called adatoms. On

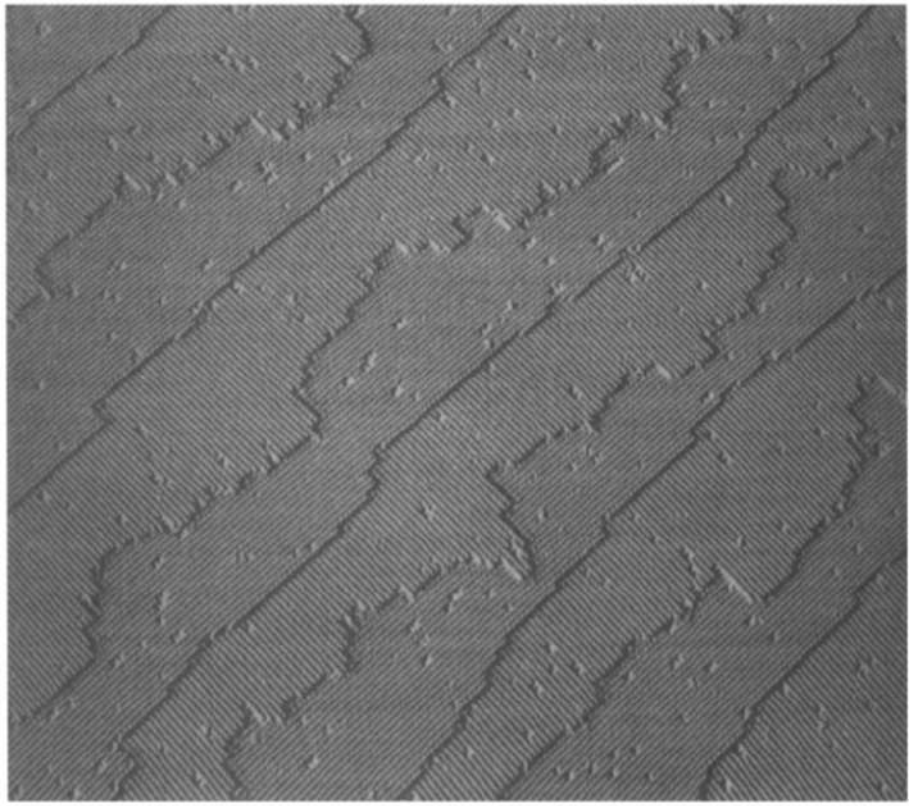

Figure 1.1. [110] steps on a (001) vicinal silicon face. Terrace width: about 100 Å (Pimpinelli and Villain, 1999).

a low index surface, the most likely site of impact is a flat facet but if the adatoms are mobile they eventually get incorporated at a step and then possibly a kink site on the step (Pimpinelli and Villain, 1999). Adatom diffusion events cannot be observed directly in STM because of the short time scale of the transitions. An STM microscope involves a metal tip close to the surface from which or to which electrons can flow by tunneling. The presence of the STM tip can disturb the motion of an adatom but if the imaging is done at low temperature the diffusion is too slow and the structure is frozen. Individual adatoms can also be visualized by FIM (Wang and Ehrlich, 1991) but the technique is limited to small surface area at the end of a tip (Pimpinelli and Villain, 1999).

At a finite temperature, there will be some equilibrium density of adatoms on the crystal surface, defined as the number of occupied sites divided by the number of surface sites At thermal equilibrium the density is given by the Boltzmann distribution as

$$\rho = \exp\ (-\beta\ W_a) \tag{1}$$

where β = 1/k$_B$T, k$_B$ is the Boltzmann constant and W$_a$ is the free energy required to extract an atom from a kink site on a step and turn it into an adatom on a flat terrace (Stoltze, 1994). For a metal surface, the value of W$_a$ is quite high, as can be seen in Table 1.1.

Table 1.1. Typical energy values (in degrees Kelvin) for four FCC metals (Stoltze 1994)

	Ni	**Cu**	**Ag**	**Au**
Adatom energy W_a (001)	8700 K	5900 K	4200 K	3550 K
Step energy W_1 (001)	2200 K	1450 K	1000 K	750 K
Kink energy W_0	1800 K	1250 K	950 K	800 K
Advacancy energy (001)	8400 K	5500 K	3850 K	2900 K
Adatom energy W_a (111)	11650 K	8300 K	6450 K	6600 K
Cohesive energy $-W_{coh}$	51600 K	40800 K	34400 K	44000 K

The table gives values of the basic parameters that are needed for the prediction of thermodynamic equilibrium. The values of these parameters can be estimated using electronic structure calculations, such as density functional theory (DFT) (Kley et al., 1997) or simpler semi-empirical approximations for example tight binding (TB), embedded atom method (EAM), or effective medium theory (EMT) approaches (Desjonqueres and Spanjaard, 1996; Lannoo and Friedel, 1991; Jacobsen et al., 1994). The estimates for Ni(111) given in Table 1.1 as an example. They show that at room temperature one can expect an equilibrium density of about one adatom per square centimetre, i.e. a very low density. On the (001) face of Cu, the proportion of lattice sites occupied by adatoms is about 10^{-9} at room temperature, which is higher, but still very low.

Under growth conditions, the density of adatoms is much higher than the thermodynamic equilibrium value and the morphology of a growing surface is governed by kinetic processes rather than thermodynamic equilibrium. The growth process typically leads to the formation of islands as shown in Fig.1.2. Each island represents a new terrace surrounded by steps. A surface of a crystal always has some steps anyway for two reasons: firstly, because it is not possible to prepare a perfect crystal, and secondly

because of thermal excitations that create steps (roughening). Furthermore, real crystals always have some dislocations and when a dislocation comes to the surface a deviation from a flat terrace is formed (Wolf et al., 1991).

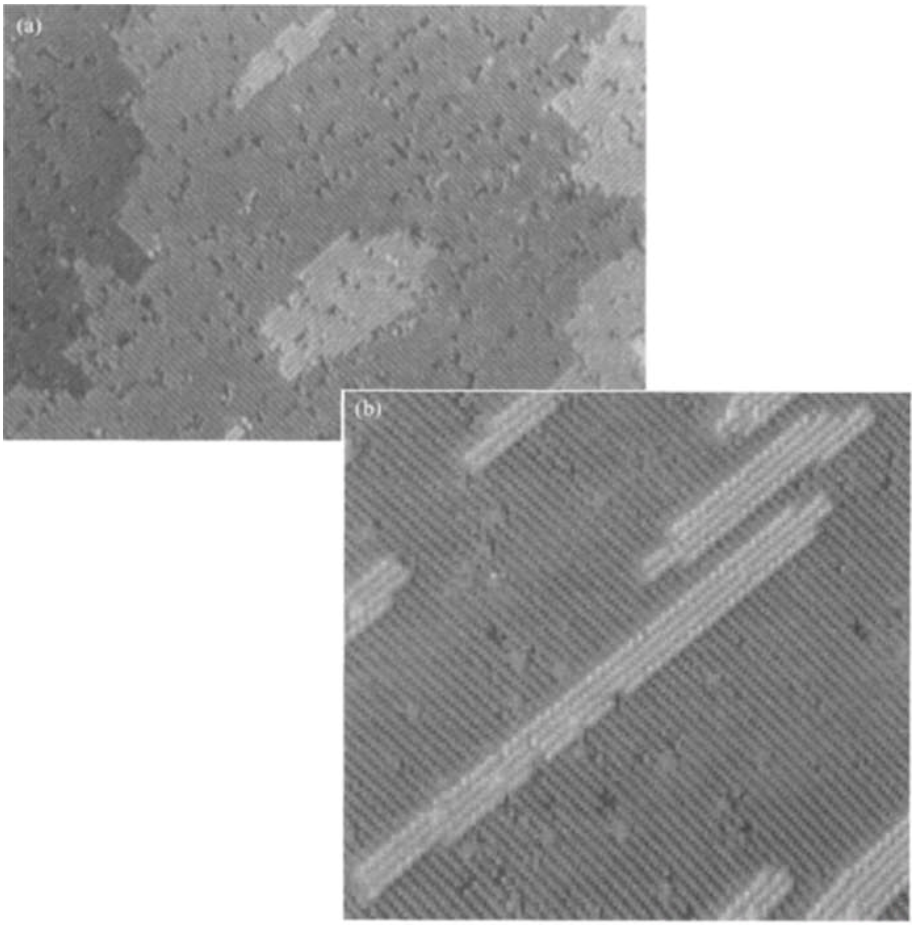

Figure 1.2. STM images of Si(001)-2x1 surfaces formed by MBE growth at room temperature. (a) After annealing at 625 K. (b) Without annealing. Figures taken from (Pimpinelli and Villain, 1999). Note the islands and the steps. The elongated islands in (a) indicate the presence of anisotropy in adatom sticking to steps leading to non-equilibrium shape. The annealed surface in (b) is closer to the equilibrium shape.

Theoretical studies have played an important role in the identification of the atomic-scale processes that are responsible for the surface structure observed experimentally. Several questions are addressed, such as: Is the growing crystal surface smooth or rough? What are the critical atomic scale mechanisms that determine the growth mode? Under what conditions is amorphous solid obtained rather than a crystal? In some technological applications in materials processing the goal is to form a thin crystalline film on the surface at as low temperature as possible to restrict interlayer diffusion.

The growth mode depends on the type of atoms involved and growth conditions so as to achieve the right balance between various competing atomic-scale processes. A theoretical prediction of the growth processes requires accurate description of the atomic interactions and estimates of the rates of several atomic-scale transitions and ultimately a simulation of the growth on the timescale of the experiments. This task is harder than it may seem Jonsson (2000).

The interaction between atoms can be described at various levels of theory. The most accurate practical approach is DFT (Kohn et al., 1996) where no parameter values are fitted to reproduce information about the chemical bonds in the system studied. The common error bar in such calculations is typically taken to be 0.1 eV. However, when the energy of similar configurations of the atoms is compared, there can be cancellation of errors and the energy difference can have smaller error bar. At room temperature, the thermal energy, k_BT is 0.025 eV.

Given some description of the atomic interactions, the main problem in the theoretical studies of crystal growth is the identification of the important atomic-scale processes. What is the transition mechanism and what types of processes are essential? It might seem at first that numerical simulations of the classical dynamics, as a finite difference solution of Newton's equation of motion, could be used to reproduce the laboratory growth process. Such classical dynamics simulations of atoms and molecules have provided important insight and improved knowledge of atomic-scale processes in various areas of science (Berne et al., 1998). But, direct classical dynamics simulations are limited to very short timescale, the time increment per iteration being limited by the need to reproduce atomic vibrations. As a result, a nanosecond of real time requires weeks of computations. As a result, there is a serious limitation of the kinds of phenomena that can be observed in such simulations. The most essential crystal growth processes such as diffusion and changes in the shape of islands are usually "rare events" on the time scale of vibrations. For example, in order for a classical dynamics simulation to show an atomic transition with activation energy of 0.5 eV and typical pre-exponential factor in the Arrhenius expression of the rate constant a millisecond of real time at room temperature would need to be simulated. This would require impossibly long computations.

The activation energy of several important transitions is estimated to be even higher, for example the diffusion of a Pt adatom along the edge of a Pt step (Jonsson, 2000; Bassett and Webber, 1978) is ca. 0.7 eV, and diffusion of a Si adatom on top of the Si (100) surface (Mo et al., 1992; Jonsson, 2000) is ca. 0.6 eV. These diffusion events occur several times per second at room temperature and are active on the laboratory experimental timescale. Between these diffusion events there are on the order of 10^{10} vibrational periods. A direct classical dynamics simulation tracking this vibrational motion would require on the order of 10^5 years of computer calculations on the fastest present-day computer before a single diffusion event can be expected to occur. Clearly, useful crystal growth simulations cannot be carried out simply by carrying out calculations of the classical dynamics of the atoms. It is essential to reach much longer simulated timescale. The timescale problem is one of the most important challenges in computational chemistry, material science, and condensed matter physics.

1.2 Outline

The main focus of the thesis to explore the descent of adatoms from on top of platinum and gold isaland into the growing layer. This is the key issue determining whether a crystal surface grows layer-by-layer or forms three-dimensional islands. The optimal mechanism for such interlayer transport was identified taking into account the surface morphology, in particular presence of kinks on the step edges. These kinks affect the mobility of the atoms across the surface. The Thesis describes the several theoretical approaches such as density functional theory (DFT), semi-empirical potential functions, and machine learned Gaussian approximation potentials (GAP) for descending the atomic interactions. Chapter 3 focuses on the theory and methodology, where a brief introduction of each theoretical technique is given and a discussion given on how these methods were applied on Pt and Au systems. These techniques were used for determining the mechanism of adatom migration on surfaces of solids and interlayer transport. Minimum energy paths for the various elementary processes were calculated using the nudged elastic band method in order to identify the transition mechanisms and evaluate the corresponding activation energy. Particular focus was on processes involving the descent of adatoms that land on top of a growing close packed layer on platinum and gold crystals. Chapter 4 gives an overview of surface growth mechanism and interlayer transport. In this chapter the Ehrlich-Schwoebel barrier is introduced and the Re-entrant layer-by-layer growth discussed. The focus is on interlayer transport of a Pt or a Au adatom on a stepped, close-packed surface of the corresponding crystal has been explained where all the relevant processes such as downstepping of Au/Au (111) and Pt/Pt(111) using EMT calculations, DFT/PBEsol calculations, and GAP calculations are described in a comprehensive way. A description of the mechanism of Au adatom diffusion on Si(100) surface is also part of this chapter. Chapter 5 corresponds to the results and discussions that have been reported in publications. Chapter 6 consist of summary of three articles and chapter 7 describes the conclusion and outlook.

2 Introduction to Metal Nanostructures

2.1 Introduction

2.2 Properties of Metal Nanostructures

Rapid development in the techniques for synthesis of metal nanostructures with controlled morphology has made it possible to study their unique properties in a more controlled way (Mulvaney, 2001). It is clear that the shape and size of metal nanostructures strongly affect their properties. The high surface to volume ratio is one of the most important properties. Table. 2.2 shows the relationships between particle size and the percentage of surface atoms for Pt nanoparticles with cuboctahedral shape (An and Somorjai, 2012). As the size of Pt nanoparticles decreases, a dramatic increase in the ratio of surface atoms is obtained. This is an important aspect in many applications, especially for chemical catalysis (Lewis, 1993). The shape of a metal nanoparticle also affects its catalytic, optical, and magnetic properties.

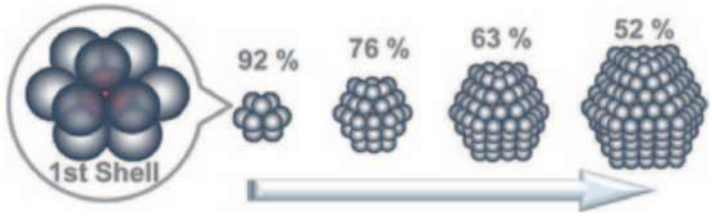

Figure 2.3. Cuboctahedral Pt nanoparticles of various size and the corresponding percentage of surface atoms.
(Niu and Lu, 2015).

Table 2.2. Cuboctahedral Pt nanoparticles of various size and the corresponding percentage of surface atoms

No. of shells	Surface atoms	Total atoms	% of surface atoms	Pt NP size in nm.
1	12	13	92	0.8
2	42	55	76	1.4
3	92	147	63	1.9
4	162	309	52	2.4
5	252	561	45	3.0
6	362	923	39	3.5
7	492	1415	35	4.1
8	642	2057	31	4.6
9	812	2869	28	5.1

2.2.1 Optical properties

The colors of Au and Ag nanoparticles have intrigued people for thousands of years. They originate from localized surface plasmon resonances (LSPR). LSPR is the resonant collective oscillation of nearly free electrons in the particles under light irradiation (Willets and Van Duyne, 2007; Chen et al., 2013; Zhao et al., 2006). As a result, the particles can absorb or scatter light, and there can be enhanced local electromagnetic field at the particle surface. As a result, plasmonic excitations in nanostructures have found broad applications in biological sensing and imaging, photochemical processes, and solar energy harvesting (Zhao et al., 2006; Atwater and Polman, 2011; Haes and Van Duyne, 2004; Ueno and Misawa, 2013). The metal nanostructures used for absorbing light in the visible range are typically made of gold, silver or copper (Willets and Van Duyne, 2007). An important characteristic of LSPR is that it is strongly dependent on the size, shape, and composition of the metal particle. By varying the particle size through the synthesis method, the LSPR properties can be tuned. Another characteristic of LSPR is that it is very sensitive to the refractive index of the surrounding medium (Willets and Van Duyne, 2007). Marked red shifts using the LSPR spectral position can be seen when the refractive index of the surrounding medium increases. Due to this property, LSPR has been used for ultra-sensitive sensing (Sepúlveda et al., 2009).

2.2.2 Catalytic properties

The development of metal nanostructures has had impact on the field of heterogeneous catalysis (Zaera, 2013; Cheong et al., 2010; Wu et al., 2012). By controling size and shape of metal nanostructures in model systems the structure-function relationship in heterogeneous catalysis can be studied and in principle this can lead to significant advances in efficiency and selectivity (Li and Somorjai, 2010). A particularly impressive example is the discovery of Au nanocluster catalysis for low temperature CO oxidation Haruta (2005); Haruta et al. (1989). While the surface of a Au crystal is unreactive and does not catalyse CO oxidation, Au nanoparticles in the size range of 3-4 nm

are highly active for CO oxidation reaction. Larger as well as smaller particles are less active per surface site. Control of the size of metal nanostructures has made it possible to reduce to cost of metal catalysts (Xiong et al., 2007). Furthermore, by controlling the surface crystal facets of Pt nanocrystals, the catalytic activity can be increased (Zhou et al., 2009). Fig. 2.4 illustrates the atomic arrangement in several crystal facets of FCC crystals (Tian et al., 2008). As an example, the high index facets can have up to 400 fold increase in the catalytic activity in electro-oxidation of small organic fuels compared with commonly used polycrystalline Pt catalysts (Tian et al., 2007). Also, control of the shape of metal nanostructures can influence the selectivity in the catalytic reaction (An and Somorjai, 2012). Somorjai et al. have found that in benzene hydrogenation reactions, cyclohexane and cyclohexene products are formed on cuboctohedral Pt nanocrystals with both (111) and (100) facets, while only cyclohexene is produced on Pt nanocubes with (100) facets (Bratlie et al., 2007).

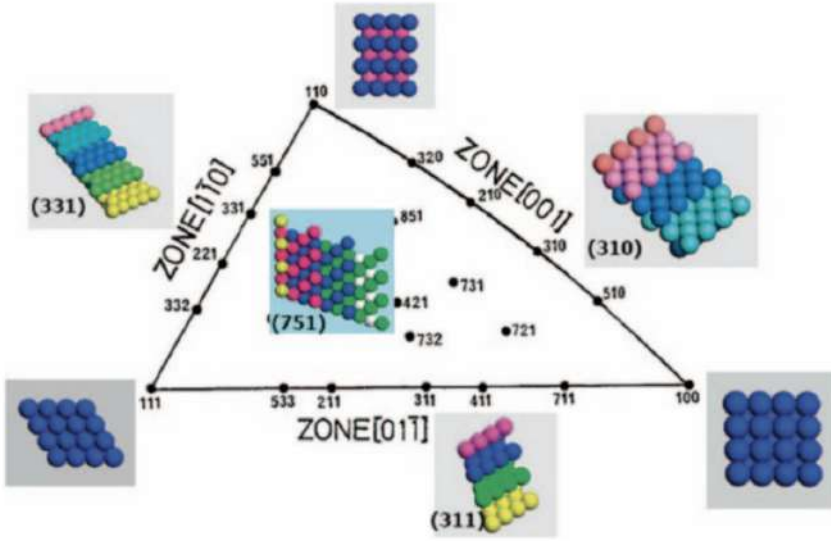

Figure 2.4. Unit stereographic triangle of the face-centered cubic (FCC) crystal and models of the surface atomic arrangements (Tian et al., 2008).

.

2.2.3 Magnetic Properties

The shape and size of ferromagnetic metal nanostructures can have significant effect on their magnetic properties (Jun et al., 2008). For small enough clusters, thermal energy can invert the direction of the magnetic moments of the atoms and due to such magnetic fluctuation the total magnetization then becomes zero. This is referred to as superparamagnetism (Gubin, 2009). The transition from ferromagnetism to superparamagnetism is temperature dependent since the energy barrier for reorientation of the magnetic moments can be overcome more easily as the temperature is increased.

(Guimarães and Guimaraes, 2009). The transition temperature strongly depends on the size because the energy barrier is higher the larger the nanostructure is. For example, the transition from ferromagnetism to superparamagnetism in cobalt nanoparticles of size 2, 4, 6, 8, and 13 nm occurs at 10, 20, 100, 180, and 370 K, respectively (Jun et al., 2007). The magnetic coercivity of a cobalt nanoparticles also depends on its size. For single magnetic domain Co nanoparticles, the magnetic coercivity increases with size. However, for Co nanoparticles with more than one magnetic domain, the magnetic coercivity decreases as the size of the Co nanoparticle increases (Park et al., 2002). The shape and composition of metal nanostructures also affects the magnetic coercivity (Choi et al., 2005; Park et al., 2004; Park and Cheon, 2001). For example, Co nanowires with larger aspect ratio have higher coercivity than those with small aspect ratio (Choi et al., 2005).

2.3 Experimental methods studying surface morphology

Various experimental techniques have been developed for studying the morphology of metal nanostructures. A few of them are described below.

2.3.1 Transmission Electron Microscope

Transmission Electron Microscope (TEM) is one of the most commonly used methods to characterize the morphology of metal nanostructures (Williams and Carter, 1996). TEM can be used to identify the shape, size, and atomic ordering in nanostructures. TEM follows the similar working principles as the light microscope except that TEM is based on an electron beam instead of light to probe the samples. The electrons can have wavelength that is four orders of magnitude smaller than that of visible light, leading to better spatial resolution (Hawkes, 2003). In TEM the high energy electron beam is correlated and focused by electrostatic and electromagnetic lenses and transmitted through the sample (Schmidt and Wetzig, 2012). The electron beam is magnified and focused by an objective lens and appears on a screen (Bozzola and Russell, 1999).

2.3.2 Scanning Electron Microscope

Scanning Electron Microscope (SEM) is one of the most advanced instruments available for the study of the 3D morphology of metal nanostructures (Reimer, 2000). SEM generates images of a sample by scanning the sample with a focused beam of electrons. As the electron beam comes in contact with the electrons of the sample, secondary electrons are generated and a signal produced giving information about the surface morphology and structure (Zweben, 1998). As a sample is scanned with an electron beam, the secondary electrons that escape and make it to the detector only come from a thin layer near the sample surface. Therefore, the method gives information about surface topography (Sharma, 2004). However, the resolution of the SEM is lower than that of the TEM.

2.3.3 Atomic Force Microscopy

Atomic Force Microscopy (AFM) is a type of scanning probe microscopy technique for imaging the surface of materials (Haugstad, 2012). It gives information about the force acting between atoms at the surface of the sample and those in the AFM tip (Breuer, 2005). In this way, it gives direct visualization of the surface structure. While scanning the AFM tip at the end of a cantilever over the sample surface, the force between surface atoms and the tip atoms is measured and the data used to provide an image of the surface (Kelsall et al., 2005). One advantage of the AFM over SEM is that it can be used in ambient air and liquid environment. A major disadvantage of AFM is the limited area that AFM can scan, typically on the order of a micrometer (Tong, 2011).

2.4 Crystal Structure and Composition Analysis

2.4.1 X-ray diffraction

X-ray diffraction (XRD) is a commonly used technique for characterizing the crystallographic structure, size, and orientation of crystals (Quate et al., 1986). It is also be used to characterize heterogeneous solid mixtures to quantify, for example, the relative amount of crystalline material (Tong, 2011). In XRD a monochromatic X-ray beam is directed to the sample and the interaction with the atoms in different crystal planes of the sample gives rise to the diffraction (Durán and Marcato, 2012). XRD can also be used to measure the particle size in nanocrystalline materials using Scherrer approach where the size of sub-micrometer crystallites is related to the broadening of the diffraction peaks (Saravanan and Rani, 2012). XRD can also determine the size of crystalline nanoparticles in powder samples.

2.4.2 X-ray Photoelectron Spectroscopy

X-ray photoelectron spectroscopy (XPS) can be used to explore the chemical composition of a sample (Hofmann, 2012). XPS can detect elements with atomic number larger than 3 with parts per million (ppm) detection limit (Singh et al., 2012). In an XPS measurement, the system is irradiated with a monochromatic X-ray beam to generate emission of photoelectrons from the surface atoms (Vajtai, 2013). These emitted photoelectrons are then collected and further analyzed using an electron spectrometer. XPS spectra show the number of photoelectrons detected as a function of the binding energy obtained as the difference between the energy of the incident beam and the measured kinetic energy of the electrons (Hosokawa et al., 2012).

2.4.3 Field ion microscopy (FIM)

The diffusion of an adatom on a solid surface is the key process determining thin film and crystal growth mode and sintering of surface islands. It also strongly affects corrosion and other chemical reactions at the surface. FIM has been an important tool for investigating surface diffusion, since it is capable of resolving individual adatoms. Pioneering surface diffusion studies utilizing FIM were carried out by Ehrlich and

coworkers (Ehrlich and Hudda, 1966). Subsequently, several important FIM diffusion studies have been carried out. These experiments have included studies of a few metals: tungsten (Ehrlich and Hudda, 1966; Bassett and Parsley, 1969; Graham and Ehrlich, 1975; Tsong et al., 1975), rhodium (Liu et al., 1991), platinum (Bassett, 1976; Liu et al., 1991), nickel (Tung and Graham, 1980), and iridium (Tsong and Kellogg, 1975; Wang and Ehrlich, 1989, 1990).

3 Theory and Methodology

The calculations presented here are all within the Born-Oppenheimer approximation where the motion of the electrons is separated from the motion of the nuclei. First, the energy of the electronic subsystem is evaluated for fixed positions of the atomic nuclei. This defines a potential energy surface (PES) for the position of the nuclei. Then, the displacement of the nuclei, such as classical dynamics and minimum energy paths for thermally activated transitions, are obtained using the energy and atomic forces derived from the PES. The Born-Oppenheimer approximation is based on the fact that the mass of atomic nuclei is much larger than the mass of an electron. As a result of the large difference in mass, the motion of the nuclei is much slower than that of the electrons.

The studies presented in this thesis involve theoretical calculations where several different approaches are used to describe the PES and thereby the atomic interactions. The metal atom interactions are described by DFT using the PBEsol functional, the EMT empirical many-body potential function, and Gaussian approximation potential (GAP) approaches. The transition mechanisms are studied by finding minimum energy paths (MEPs) using the nudged elastic band (NEB) method in order to evaluate the activation energy barriers. The main focus is on interlayer transport, i.e. down-stepping of adatoms. Different types of surfaces are studied, including straight, stepped and kinked surfaces of both Pt(111) and Au(111). Also, the diffusion of Au adatom on the Si(100)-2x1 surface are studied. For the DFT/PBEsol calculations, the Vienna ab initio simulation package (VASP) is used in combination with the VTSTtools while the calculations based on the EMT potential and GAP potential make use of the atomic simulation environment (ASE). The time evolution of the systems is simulated over a short time scale with classical molecular dynamics (MD) and on a long time scale with kinetic Monte Carlo using the EON and Zacros software.

In the studies presented there, the mechanisms for interlayer transport of adatoms on Au(111) and Pt(111) surfaces have been studied using the various levels of description of the atomic interactions. The mechanism has been identified by which an adatom that lands on top a metal island can descend to a lower layer. This is known to be a central issue determining whether the metal grows layer-by-layer or forms three-dimensional islands. Various downstepping mechanisms have been studied for both the Pt/Pt(111) and the Au/Au(111) system.

Another part of the thesis deals with the diffusion of a Au adatom on the Si(100)-2×1 surface. There DFT/PBEsol is used as well as empirical potential functions. Classical molecular dynamics (MD) simulations are carried out as well as long timescale simulations of Au deposition and annealing process. The long time scale simulations reveal an unusual diffusion mechanism that can lead to island nucleation in unexpected parts of the surface.

The various levels of estimating the interaction between the atoms will now be described.

3.1 Empirical Potentials

One of the approaches for estimating the interatomic forces is to parametrize a potential energy function based on input from experiment and/or electronic structure calculations. A great deal of work has been done to model metals using such empirical potentials, for example effective medium theory (EMT) (Hansen et al., 1991; Kitagawa et al., 1997) and embedded atom method (EAM) (Daw and Baskes, 1984; Voter and Chen, 1987). For semiconductors, the focus has mostly been on Si (Stillinger and Weber, 1985; Tersoff, 1988). When these approaches are successful, they make the simulation of large systems and thorough exploration of mechanisms of relevant processes possible. A great deal of work has gone into the development of such potential energy functions and many properties can be reproduced quite well. But since these potential functions are typically parametrized to reproduce bulk properties, the description of surfaces, and even more so adatoms on surfaces, can be outside the range of validity. Nevertheless, studies of adatom diffusion using such potential functions has proven to be useful even though the estimated energy barriers are only a rough qualitative estimate. This turns out, for example, to be the case for Pt (Liu et al., 1991). Important quantitative differences between DFT results and these approaches have, however, been found (Feibelman, 1999, 1998).

3.1.1 Effective Medium Theory

EMT (Jacobsen et al., 1987) is an attempt to capture the fundamental physics related to the interaction between atoms in metallic systems in a simple way. EMT is a hierarchy of approximations based in principle on DFT (Jacobsen et al., 1987). In the following, we consider a one-component metallic systems and the basic level of EMT. (Jacobsen et al., 1987). A more elaborate form is the *corrected effective medium theory* (Yang and DePristo, 1994). Other approaches are referred to as glue model (Bilalbegović et al., 1993), and approaches based on tight binding (Rose et al., 1981; Finnis and Sinclair, 1984). Essentially, the potential energy of the system of is approximated as

$$E = \sum_i E_c(i) + \Delta E_{AS}(i) \tag{2}$$

where E_c is the energy of embedding atom i in a homogeneous electron gas and ΔE_AS is an atomic sphere correction term. The summation runs over all atoms in the system.

3.2 Gaussian Approximation Potential (GAP)

Recently, there has been great interest in using machine learning approaches to represent the PES. based on the energy of some input configurations but without an assumed form of the potential energy function. Typically, the input is some thousands of DFT calculations and the machine learning is a way to interpolate between those data points to predict the energy of new configurations of the atoms (Deringer et al., 2019). Here, a PES for platinum atoms modeled with Gaussian process regression in the so-called Gaussian approximation potential (GAP) (Bartók et al., 2010; Bartók and Csányi, 2016; Deringer et al., 2021) approach is used. GAP performs a non-parametric regression of training points, i.e. it does not rely on a predetermined functional form to describe the PES but, obtains this rather from the available data, here DFT calculations with the PBEsol exchange-correlation functional (Perdew et al., 1996).

The DFT calculations used as training set were carried out using a plane-wave basis set for the valence electrons and projector augmented-wave (Blöchl, 1994) description of the inner electrons. The VASP (Kresse and Furthmüller, 1996; Kresse and Joubert, 1999) software was used. The GAP potential involves a combination of 2-body (2B) and many-body (MB) descriptors. The 2B descriptors are based on interatomic distances up to a certain cutoff, whereas the MB descriptors use a revised smooth overlap of atomic positions (SOAP) representation (Bartók et al., 2017; Caro, 2019). SOAP provides information about the chemical environment of a given atom up to a given cutoff distance. GAP relies on an approximation of locality and smoothness of the PES, and thus performs an optimal (in the least-square sense) decomposition of the total energy into a sum over local (atomic) contributions. The expression for the GAP energy contribution of atom i is

$$\varepsilon_i = \delta^{2\mathrm{b}^2} \sum_{r_{ij}<r_{\mathrm{cut}}} \sum_{s=1}^{N_{\mathrm{sparse}}^{2\mathrm{b}}} \alpha_s^{2\mathrm{b}} k^{2\mathrm{b}}(r_s, r_{ij}) + \delta^{\mathrm{mb}^2} \sum_{s=1}^{N_{\mathrm{sparse}}^{\mathrm{mb}}} \alpha_s^{\mathrm{mb}} k^{\mathrm{mb}}(\mathbf{q}_s, \mathbf{q}_i), \tag{3}$$

where the α are the fitting coefficients, the k are the kernel functions, which have different forms and take different arguments depending on the type of descriptor, r_{ij} is the distance between atom i and its neighbor j, $\mathbf{q}_i$ is the SOAP descriptor of atom i and δ gives the energy scale of the interactions (which are different for the 2B and MB parts). The index s runs over the *sparse set* descriptors, a subset of all descriptors in the training set. Sparsification is used to reduce the computational cost of evaluating the GAP potential (Bartók and Csányi, 2016).

For the GAP potential to give a good estimate of the energy of a given system it is essential that the training database includes atomic arrangements that are similar to the input configuration. The GAP potential for Pt used in this work is trained from a comprehensive database including relaxed and distorted crystal structures (FCC, HCP, BCC, and SC), dimers and trimers, surfaces (with various step-terrace configurations and edges), nanoparticles and liquid Pt configurations. An exhaustive characterization of this potential, which is freely accessible online from . Use of the potential requires the QUIP-GAP or TurboGAP codes, which are free for non-commercial research. It can also be used with LAMMPS (Plimpton, 1995) through its QUIP interface.

3.3 Density Functional Theory

DFT is based on two theorems proved by Kohn and Hohenberg and a practical implementation by Kohn and Sham presented in the mid 1960s. The first theorem essentially states that the *ground state energy given by the Schr/"odinger equation is a unique functional of the electron density* up to an arbitrary constant. The theorem shows that there exits a one-to-one mapping between the ground-state wave function and the ground-state electron density. The ground state energy is, thereby a functional of the ground state electron density. A functional is analogous to the well known concept of a function. While a function has a variable or variables as input and delivers a number, a functional has a function as input and delivers a number. An example of a functional is

$$F[f] = \int_1^1 f(x)dx. \tag{4}$$

F is a functional of the function $f(x)$. The Hohenberg and Kohn theorem shows that the ground state energy, E, can be expressed as $E[\mathrm{n}(\mathbf{r})]$, where $\mathrm{n}(\mathbf{r})$ is the ground state electron density. Therefore the name density functional theory.

The Hohenberg and Kohn theorem shows, furthermore, that all properties of the ground state, not only the energy, can be obtained from the ground-state electron density Why is this statement important? The reason is that the electron density is a much simpler function than the wave function. It only depends on three spatial variables, while the wave function depends on 3N variables. As an example, the wave function for the electrons in a nanocluster of 100 Al atoms involves 3900 variables while the electron density involves only 3 variables. This represents a tremendous simplification.

The first Hohenberg-Kohn theorem shows that a functional of the electron density exits but it does not provide any information as to what this functional is, apart from a full solution of the Schr/"odinger equation. The second Hohenberg-Kohn theorem, however, describes an important characteristic of the functional: *The electron density that minimizes the energy obtained from the functional is the true electron density and corresponds to an exact solution of the Schrodinger equation* (Sholl and Steckel, 2011).

The Kohn-Sham formalism provides a practical implementation of these results. In order to estimate the ground state properties of a system of N interacting electrons subject to an external local potential $V(\mathrm{r})$ the problem is mapped onto a fictitious system of N non-interacting electrons. Each electron is then described by an orbital, a one-electron wave function. The total electron density is the sum over the electron density obtained from each orbital. The Hamiltonian is written as

$$H|\psi>=[T+V_{ee}+V]|\psi>=\left[\sum_{i=1}^{N}-\frac{1}{2}\nabla_i^2+\sum_{i<j}^{N}\frac{1}{r_i-r_j}+\sum_{i=1}^{N}V(r_i)\right]|\psi>=E|\psi> \tag{5}$$

were T is an operator for the kinetic energy, V_{ee} is the classical Coulomb interaction and V is the external potential, corresponding to the Coulomb interaction between an electron and the positive atom nuclei, and possible also an additional applied potential. The ground state energy is E and the index i indicates the individual electrons. Equation (4) represents a differential equation of second order and the number of independent

variables is $3N$ but they are described separately by the orbitals, a great simplification compared with the full wave function.

The Ritz variational principle can be used to obtained the optimal wavefunction $|\psi>$. The expectation value of the Hamiltonian operator should be minimized

$$E_0 = min_{\psi \to N} < \psi|H|\psi > = < \psi|T + V_{ee} + V\psi > \tag{6}$$

Here, the notation a search over all allowed, antisymmetric and normalizable N-electron wave function is carried out subject to the constraint that the given electron density is obtained

$$\rho(r) = N \int d\sigma dX_2 ... dX_N |\psi(r, \sigma, X_2, ..., X_N)|^2 \tag{7}$$

and corresponds to the given number of electrons, N. The quantity X_i = (r_i, σ) adds the spin variable σ to the spatial variables. In general, separate spin-up and spin-down electron densities need to be determined, but for singlet states where all the electrons are paired, an electron density that only depends on the spatial coordinates is sufficient (Rohra, 2006).

3.4 Hohenberg-Kohn theorems

The basic idea behind the first Hohenberg and Kohn theorem (Hohenberg and Kohn, 1964) is to show that the electronic density of a system is sufficient to determine its energy and thereby replace the wave function as the central quantity for characterizing the system.

The first Hohenberg-Kohn theorem states that apart from an arbitrary constant, the external potential V(r) can be determined from the ground state electron density ρ(r). From the electron density one can obtain the corresponding Hamiltonian operator and thereby also the ground state wave function $|\psi[\rho]>$ and all electronic properties of the system. The kinetic energy, T, of the electrons and the electron-electron interaction energy, V_{ee} has the same expression for all systems. The only term in the expression for the energy that is specific for a given system is the external potential, V(r). The total energy can be written as

$$E[\rho] = T[\rho] + V_{ee}[\rho] + \int drV(r)\rho(r) = F[\rho] + \int drV(r)\rho(r) \tag{8}$$

where the HK-functional $F[\rho]$ is defined as

$$F[\rho] \equiv T[\rho] + V_{ee}[\rho] = < \psi[\rho]|T + V_{ee}|\psi[\rho] > \tag{9}$$

The electron-electron term is separated into two terms

$$V_{ee}[\rho] \equiv U[\rho] + E_x c[\rho] \tag{10}$$

by defining the classical Coulomb energy as

$$U[\rho] = \frac{1}{2} \int \int dr dr' \frac{\rho(r)\rho(r')}{|r - r'|}. \tag{11}$$

The functional $E_{xc}[\rho]$ then describes the non-classical term to the electron-electron interaction. $E_{xc}[\rho]$ contains quantum mechanical exchange and as well as a correction for the self-interaction contained in U and all correlation effects. All intrinsic properties of the electronic system are absorbed in the HK functional $F[\rho]$.

The second Hohenberg-Kohn theorem states that the functional $E[\rho]$ of the total energy is subject to a variational principle with regards to the density. More accurately, the minimal value of the total energy $E[\rho]$ with respect to all variations of ρ that corresponds to the given number of electrons,N, is obtained for the correct ground state density ρ_0

$$E_0 = min_{\rho \to N} E[\rho] = E[\rho_0] \tag{12}$$

The symbol "$\rho \to N$" denotes variation over all ground state densities corresponding to N-electron systems.

The first Hohenberg-Kohn theorem shows that for any arbitary density ρ(r) the external potential V(r) is unique to within an arbitrary constant. But, such a potential may actually not exist. The assumption that such a potential exists is referred to as V-representability. It is indeed possible to generate densities that cannot be related to any external potential V(r).

3.5 Nudged elastic band method

When studying rearrangements of atoms in theoretical chemistry and condensed matter physics the challenge is to identify the optimal reaction path connecting the initial state to the final state. Since the probability distribution for a system connected with a heat bath at well defined temperature is given by the Boltzmann distribution where the probability distribution drops as the potential energy increases, the optimal transition path corresponds to a minimum energy path (MEP), i.e. a path for which the energy is at a minimum with respect to all perpendicular degrees of freedom. The MEP is typically used as a reaction coordinate (Marcus, 1966) for a transition, such as chemical reactions, conformational changes of molecules, diffusion events in solids, etc. The maximum energy along the minimum energy path (MEP) is a first order saddle point on the PES and gives the activation energy for the transition, a quantity of central importance of estimating the transition rate within harmonic transition state theory (Vineyard, 1957).

When the initial and final state of a transition is known, a robust method can be used to find the MEP and thereby the activation energy of the transition from the point of maximum energy along the MEP (Jonsson, 2000). A string of replicas of the system is created by applying some interpolation between the initial and final state of the transition (most simply a linear interpolation). The replicas are connected with springs so as to generate a connected path. Then an optimization algorithm is applied where the atomic force component perpendicular to the path plus the spring force along the path is zeroed. This makes the position of the intermediate replicas move to the nearest minimum energy path (Mills et al., 1995; Jónsson et al., 1998). When the same spring constant is used between all the adjacent replicas, the optimization results in even spacing of the images along the MEP. While the saddle point is the only point needed for the harmonic TST rate estimate, in addition to the initial point, the MEP gives a useful, extended view

of the most relevant part of the PES.

3.6 Kinetic Monte Carlo

Classical molecular dynamics simulations can only represent a very short time scale in the evolution of the system. A typical time step is on the order of a femtosecond for atomic systems at around room temperature and simulations on present day computers are, therefore, typically limited to nanoseconds. This holds when fast, empirical potential functions are used. If, however, the atomic forces are obtained from electronic structure calculations, the time scale of practical trajetory calculations is further reduced to picoseconds. This creates a gap of several orders of magnitude between what one can simulate with classical dynamics and the time scale that is relevant for interpreting experimental measurements. Many important thermally activated transitions occur on a much longer time scale so there is need for theoretical methods to model these important rare event dynamics.

The most commonly used method for modeling state-to-state dynamic is kinetic Monte Carlo (KMC) (Bortz et al., 1975; Gillespie, 1976). If all the possible transitions in the system and their rates are already known, one can use KMC to simulate a time ordered sequence of events and and thereby long time scale evolution of the system. For specified reaction mechanisms, the rates can be obtained from a PES using transition state theory (TST) (Voter, 1986). The key challenge is to come up with the list of possible transitions and their atomic scale mechanism. KMC can easily include large number of events with modest computational effort. The time scale that can be represented is, however, limited by the fastest event in the system, it essentially sets the time increment per transition simulated. The most serious limitation is that all the transition mechanisms need to be specified before the simulation starts. The events are considered to be local movements of one or a few atoms (Hansen and Neurock, 2000). Another disadvantage of KMC is that the atomic configurations must be matched with a regular lattice in order to be able to write the table of possible events. Even in simulations of crystals, there can be defects where atoms are not placed near regular lattice positions.

3.7 Adaptive Kinetic Monte Carlo

Several of the limitations of KMC described above are lifted in the adaptive KMC (AKMC) method (Henkelman and Jónsson, 2001). AKMC is similar to KMC but extends it in two important ways: (1) The possible reaction mechanisms are determined during the simulation and do not need to be decided on beforehand; and (2) the atoms need not be assigned to a lattice. In AKMC unexpected transitions can occur that would be hard to include in a predefined event catalog (Henkelman and Jónsson, 2003). The method is termed "adaptive" because the list of possible events is not fixed, it can adapt to a particular configuration of the atoms found during the simulation. Since there is no need to assign the atoms to a lattice, the method can be used to simulate amorphous materials.

An AKMC simulation involves finding all relevant transitions from a given initial state by searching for first order saddle points on the energy rim surrounding the initial state energy well. For each saddle point found, the harmonic approximation to transition state theory (HTST) (Wert and Zener, 1949; Vineyard, 1960) is used to estimate the transition rate. The saddle point search is carried out with the minimum mode following (MMF) algorithm (Henkelman and Jónsson, 1999; Malek and Mousseau, 2000). There, the lowest curvature mode is found, i.e. the eigenvector corresponding to the lowest eigenvalue of the Hessian. The force acting on the atoms is then reversed in the direction of the minimum mode and the system advanced step by step in the direction of the revised force. This essentially transforms the force field in the vicinity of a first order saddle point to a force field corresponding to a minimum. After a saddle point has been found, the rate of the corresponding event is calculated as

$$k^{HTST} = \frac{\prod_{i=1}^{3N} \nu_i^{init}}{\prod_{i=1}^{3N-1} \nu_i^*} e^{-(E^* - E^{init})} / k_B T \tag{13}$$

where ν_i^{init} and ν_i^* are the ith stable normal-mode frequencies at the initial and saddle points, N is the number of movable atoms moving in the system, E^* is the saddle point energy, and E^{init} is the energy of the initial state. After the event table has been created, a random number is used is used to select the next transition analogous to the KMC algorithm, and the system is relaxed to the corresponding final state. The AKMC method relies on HTST and the transitions are therefore associated with saddle points on the PES (Xu and Henkelman, 2008).

3.7.1 Saddle point searches in AKMC simulations

An AKMC simulation starts from an initial local minimum energy configuration and from there saddle point searches are used to identify transitions that can occur in the system. The MMF method (Henkelman and Jónsson, 1999) is usually used in AKMC simulations to find saddle points. Several extensions have been made to the MMF method since it was originally developed. This includes the use of a forward instead of central-difference approximation (Heyden et al., 2005; Olsen et al., 2004), a rotational force criterion to neglect unnecessarily tight convergence of the lowest mode (Olsen et al., 2004; Heyden et al., 2005), a large finite-difference rotation to improve stability with noisy forces obtained from electronic structure calculations (Heyden et al., 2005), the limited memory Broyden-Fletcher-Goldfarb-Shanno optimizer (Nocedal, 1980), and internal coordinates for faster convergence rate (Kästner and Sherwood, 2008). With these improvements, saddle points can be found from a local minimum in a few hundred energy and force evaluations - not significantly more than a minimization (Xu and Henkelman, 2008).

3.7.2 How many saddle searches are needed?

For a perfect AKMC simulation, all saddle points with low energy, and thereby corresponding to transitions with high rate, need to be found. A dynamical stopping criterion based on the history of previous searches can be used to estimate the probability that an important saddle point has been missed. This has two advantages: (i) this criterion

gives a confidence level for the accuracy of the simulation, and (ii) states with a small number of processes need a small number of searches, whereas states with many more processes need more to satisfy the criterion. The chosen confidence level should give a reasonable balance between the simulation effort and the accuracy of the simulation (Xu and Henkelman, 2008). The number of saddle points likely increases exponentially with the size of the system. Most of these correspond to high energy and are not important for the construction of the event table. The range of relevant energy barriers depends on the thermal energy k_BT. A barrier that is $20k_BT$ higher in energy than the lowest saddle point is e^{-20} times as likely to occur as lower barrier event, assuming the two have similar pre-exponential factors. Even if the pre-exponential factors vary by several orders of magnitude, e^{-20} 10^{-9} is such a small number that $20k_BT$ is a safe criterion for determining which saddle points are relevant (Xu and Henkelman, 2008).

Figure 3.5. Reaction mechanisms with barriers within mk_BT of the lowest saddle point energy are considered relevant. For a choice of m = 20, the chance of a higher barrier process occurring in the dynamics is approximately e^{-20} (Xu and Henkelman, 2008).

.

4 Surface growth mechanism and interlayer transport

4.1 The Ehrlich-Schwoebel barrier

The crucial characteristic of the energy landscape that determines whether the growth of a crystal surface is 2D or 3D is the energy barrier for descent of adatoms from atop islands. This is referred to as interlayer transport. Bond counting can be used to illustrate why such a barrier is likely to exist. If an adatom on a close-packed surface moves by hopping over an island edge, it needs to break one of the three bonds it forms with the underlying atoms before it can reform bonds in the lower layer, thereby creating a high-energy transition state. Several theoretical calculations as well as experimental observations show, however, that the adatom does not descent by a hop over the edge but rather by a concerted two-atom process involving also a step edge atom. Nevertheless, the energy barrier for such a downstepping event is higher than the energy barrier for the diffusion on a flat terrace so there is an added energy penalty for getting down to the lower layer. An atom that lands on top of an island, therefore, faces an energetic wall along the edge of the island. At low enough temperature, adatoms that land on top of an island cannot descend to the lower layer and eventually a new island on top of the existing island forms, leading to 3D growth. The presence of such an energy barrier was predicted by Schwoebel & Shipsey (Schwoebel and Shipsey, 1966) and was, furthermore, deduced from experimental measurements by Ehrlich & Hudda (Ehrlich and Hudda, 1966). The difference between the energy barrier for descent and the energy barrier for diffusion on the flat terrace is now generally referred to as the Ehrlich-Schwoebel (ES) barrier.

4.2 Re-entrant layer-by-layer growth

A most remarkable observation has been made from experimental crystal growth studies where layer-by-layer, i.e. 2D, growth is obtained as the temperature is lowered below a temperature range where the growth is 3D. Since the growth is 2D also at even higher temperature, this is referred to as re-entrant layer-by-layer growth. This has been studied most extensively for Pt(111) growth (Kunkel et al., 1990). Initially, this was deduced from the reflectivity of a thermal He atom beam during vapor deposition of Pt atoms. At a high temperature of 621 K layer-by-layer growth was observed as evidenced by regular oscillations of the intensity of the reflected beam in out-of-phase conditions. This corresponds to the step-flow mechanism where the surface is nearly flat and highly reflective all the time, but destructive interference is obtained when the growing layer covers half the surface. As the temperature was lowered to 424 K, the reflectivity

dropped exponentially with time, showing that a rough surface is formed corresponding to three dimensional growth. At this lower temperature the adatoms cannot overcome the ES barrier and new islands nucleate on top of existing ones.

Normally one would expect that the morphology of the growing surface becomes even rougher as the temperature is lowered further. However, an unexpected observation was made, namely the re-appearance of near 2D growth at 275 K. The first two layers appear from the He reflectivity to spread on the surface nearly as well as in the high-temperature step-flow region. It is known from nucleation theory that nucleation of new islands starts at a lower density at lower temperature, thereby creating more and smaller islands. Kunkel and coworkers stated that the cause of the re-entrant 2D growth could be found in "the reduced island size and/or their rough shape, both because of the reduced adatom mobility at lower temperature" (Kunkel et al., 1990). However, the experimental measurements could not provide a more specific explanation of this unexpected behavior. The question therefore remained what feature of the energy landscape and transition mechanism makes this re-entrant layer-by-layer growth possible and for what materials can such growth behavior be expected.

4.3 Interlayer transport

In the first part of this thesis, the focus is on interlayer transport of a Pt or a Au adatom on a stepped, close-packed surface of the corresponding crystal. The goal is to identify the key mechanism that can be active for interlayer transport at low temperature. This requires calculations of the mechanism and rate of the various atomic rearrangements that can take place on the surface. In the initial calculations, the interaction between the atoms is described using the EMT approximation, but in subsequent calculations the more accurate DFT approach is used. A non-intuitive mechanism has been identified by which a Pt atom that lands on top of a metal island can descend to a lower layer near a kink site. This is known to be a central issue determining whether the metal grows layer-by-layer or forms three-dimensional islands. A great deal of experimental and theoretical effort has gone into the study of these issues for Pt growth (Jonsson, 2000).

4.3.1 EMT calculations

The initial calculations described here were done with the EMT empirical potential function for describing the interactions between the atoms. In order to identify the MEP for a transition from an initial state to a given final state, the NEB method is used. Large enough systems are used to get convergence in the activation energy with respect to system size. All the systems are generated from Pt crystal structure where the calculated lattice constant is found to be 3.92 Å by using standard EMT parameters, in nice agreement with the experimental value of 3.92 Å. We use the periodic stepped and kinked systems with higher miller indices for both A and B types of steps. Steps that locally have a (111)-like microfacet formed by the step atoms and the adjacent lower layer atoms are referred to as B-type steps. Those with (100)-like microfacet are referred to as A-type steps. Even higher miller indices are used for generating these stepped surfaces with larger terraces. The MEPs are calculated from the middle of the

terrace between the steps.

Similarly, periodic configurations of kinks on steps are generated to study their influence on the interlayer transport. In order to minimize the initial and final configurations, the L-BFGS optimizer was used until the magnitude of the atomic forces dropped below fmax = 0.01 eV/Å. When a Pt adatom lands on top of an island, it diffuses around and eventually can reach the edge of the island. The question then becomes whether the downstepping process will occur or whether the adatom is reflected back into the interior of the island. A third option is that the adatom diffuses along and above the step edge and eventually comes to the vicinity of a kink on the step. The purpose of the calculations is to estimate the rate of these various processes to provide input for simulations of growth at given conditions, such as temperature. The key question is whether the metal surface grows layer-by-layer or forms three-dimensional islands.

4.3.2 DFT/PBEsol calculations

Subsequently, DFT calculations for the downstepping of a Pt adatom at a step on the Pt(111) surface were carried out using the VASP software and the PBEsol functional. As in the EMT calculations, all the systems were generated from perfect crystal structure and the calculated lattice constant for Pt was found to be 3.91 Å in good agreement with the experimental value. Surfaces with larger Miller indices are used in order to generate periodic steps with kinks. The Miller indices for the surface with B-straight step is (221), with A-straight steps is (322), surfaces with kinks on B-type steps (985), and surfaces with kinks on A-type steps (956). The cut-off energy in the plane wave expansion of the valence electron wave function in Pt calculations was 400 eV, and the Brillouin zone was sampled with a 2x2x1 Monkhorst-Pack k-point mesh. Initial and final states were minimized using velocity projection optimization. Smaller samples were used than in the EMT calculations since the DFT calculations are computationally much more demanding. The atoms in the bottom two layers are kept fixed to avoid artificial surface effects due to the missing crystal atoms below. Minimum energy paths for the descent of a Pt adatom were calculated at straight steps, at kinks and near kinks for both A- and B-type steps using the climbing image NEB (CI-NEB) method. The calculations were considered converged when the maximum force magnitude drops below 0.02 eV/Å .

4.3.3 GAP calculations

Calculations were also carried out using a Gaussian approximation potential (GAP) potential for Pt. The systems included both A- and B-type steps and kinks and were generated from perfect crystal structure and the energy then minimized. The lattice constant was found to be 3.95 Å , in a reasonable agreement with the experimental value. The same systems were used as in the DFT/PBEsol calculations to make close comparison. The activation energy barriers were calculated using the CI-NEB method.

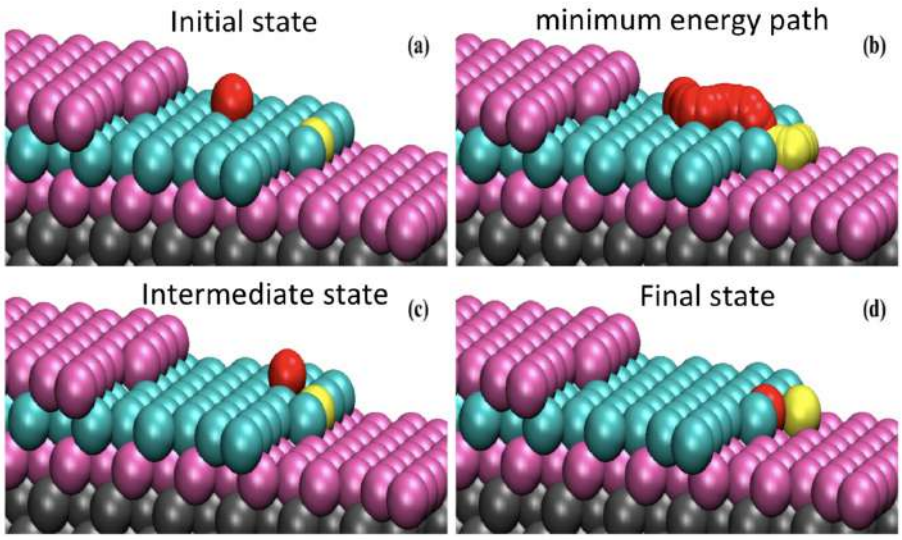

Figure 4.6. Three dimensional side view of a periodic stepped Pt surface with kinks. (a) Initial configuration where the Pt adatom (Red) sits in the middle of the terrace. (b) Minimum energy path for migration of the adatom towards a kink and concerted displacement downstepping event involving an atom adjacent to the kink (yellow). This turns out to be the mechanism with lowest activation energy. (c) The initial state for the downstepping event. (d) The final state of the downstepping event.

4.4 Downstepping of Au adatom on Au(111)

While Pt growth has been extensively studied experimentally and is therefore of particular focus in the calculations presented here, there is also great deal of interest in growing Au nanostructures on surfaces for various technological purposes. Calculations analogous to those described above for Pt have, therefore, been carried out for a the downstepping of a Au adatom via exchange mechanisms at straight A- and B-type steps, near kinks and at kinks.

4.4.1 EMT calculations

As for Pt, the calculations for Au were carried out with semi-empirical EMT potential function and the interactions between atoms described by the EMT potential function. The NEB method was used to find the minimum energy paths for the various atomic rearrangements. Larger systems (of large enough size to get convergence) were used in the EMT calculations. All the systems were generated from Au crystal structure and the calculated optimized lattice constant for Au was found to be 4.05 Å by using EMT standard parameters, in good agreement with the experimental value of 4.07 Å. Higher miller indices were used for generating stepped and kinked surfaces with larger size of terraces. In order to minimize the initial and final configurations, BFGS optimizer was used to find the local minima at each state and the magnitude of atomic forces was below 0.01 eV/A at convergence. The energy paths were found for Au adatom landing on a terrace and then migrating towards the step atoms until it replaces the edge/kink atom and descends via exchange in a downstepping process. The purpose of these calculations is to determine whether the Au metal with the close-packed (111) surface exposed grows layer-by-layer or forms three-dimensional islands.

4.4.2 DFT/PBEsol calculations

Subsequent calculations of downstepping events for a Au adatom a were done with DFT and the PBEsol functional (Perdew et al., 2008) using the VASP software (Hafner and Kresse, 1997). As in the EMT calculations, all the systems were generated from crystal structure and the calculated lattice constant for Au was found to be 4.08 Å , in a good agreement with the experimental value. Larger miller indices numbers are used in order to generate periodic stepped and kinked surfaces. The samples with miller indices values for B-straight edge (221), A-straight edges (322), B-kinked samples (985), and A-kinked samples (956) were used. The recommended cut-off energy in the plane wave expansion for Au, 300 eV was used for all calculations and Brillouin zone was sampled with a 2x2x1 Monkhorst-Pack k-point mesh. Initial and final states were minimized by velocity project optimization relaxation in all calculations. Smaller samples were used than in the EMT calculations. In the DFT/PBEsol calculations, only the last descent exchange mechanism was calculated. Minimum energy paths for the descent of a Au adatom were calculated for straight edges, at kinks and near kinks for both A- and B-type steps using the CI-NEB method (Henkelman et al., 2000). The calculations were considered converged when the maximum magnitude of the atomic forces had dropped below 0.02 eV/Å .

4.5 Diffusion of a Au adatom on the Si(100)-2×1 surface

To model the Si(100)2×1 surface, we constructed a periodic 4×4 supercell represented by a six layer slab. Hydrogen atoms were added to the bottom layer in order to passivate the dangling silicon bonds. During the DFT/PBEsol calculations, the three upper layers were allowed to relax while the rest were kept frozen at their crystal positions. A vacuum space of 15 Å was used to avoid interaction between periodic images of the simulation cell. The plane wave cutoff energy was set to 350 eV and the first Brillouin zone was sampled using a uniform mesh with 7×7×1 k-points. The optimization of atomic coordinates was carried out until the magnitude had dropped below 0.01 eV/Å.

Calculations were also carried out using two empirical Si-Au energy functions that were recently developed by Starikovet al.. These are reffered to as ADP18 (Starikov et al., 2018) and ADP20 (Starikov et al., 2020). The implementation in the LAMMPS software (Plimpton, 1995) was used for the calculations. Since electronic degrees of freedom are not included, the passivating H-layer was not needed here.

We obtained a lattice constant of 5.43 Å for the crystal in the DFT/PBEsol calculations, in excellent agreement with the experimental value of 5.43 Å. For the ADP18 and ADP20, the values of 5.41 and 5.46 Å were obtained in acceptable agreement with the experiment. The image dependent pair potential (IDPP) method (Henkelman and Jónsson, 2000) with six intermediate images was used to generate the initial path for the CI-NEB calculations of the various diffusion hops of the Au atom on the surface.

Classical dynamics simulations based on Newton's equation of motion were is to simulate sequential deposition of Au atoms on the Si(100)-2×1 surface. For each deposition event, starting from random lateral position, a nanosecond is simulated before another atom is deposited. Due to the limitation of short time scale, direct classical simulations are not allowing for diffusion and annealing so, we used long time scale simulations to represent the time period in between deposition events. These long time scale simulations using adaptive Kinetic Monte Carlo (AKMC) method and classical dynamics simulations were performed with the EON software package (Chill et al., 2014).

5 Results and Discussion

5.1 Calculations of Pt adatom migration using EMT potential

Fig. 5.7 shows results of EMT calculations for finding the lattice constant of the Pt crystal. The optimal lattice constant was found to be 3.92 Å in good agreement with experimental value. The cohesive energy for Pt was calculated 3.80 eV, in a acceptable agreement with experimental value of 3.93 eV.

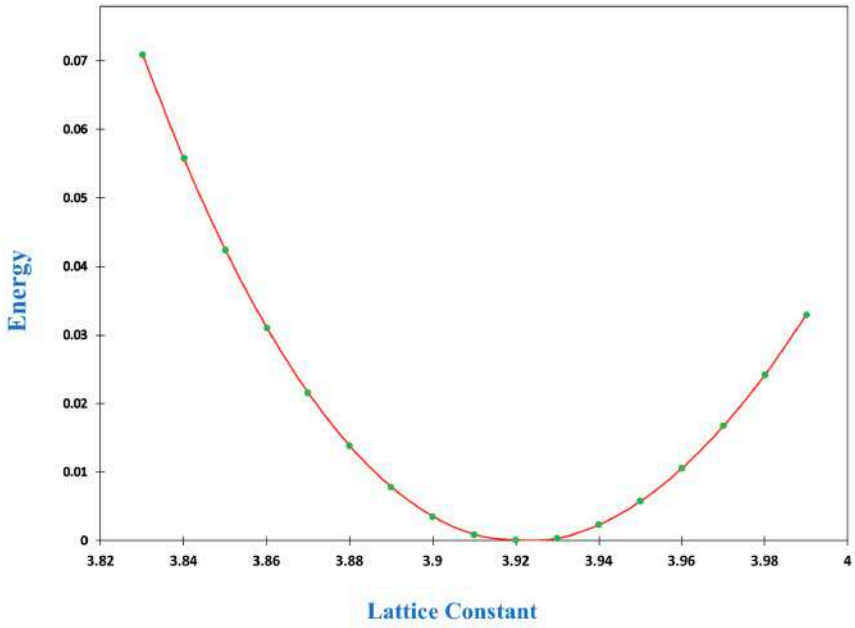

Figure 5.7. Calculation of the energy of the Pt FCC crystal as a function of lattice constant for using the EMT potential. The optimal lattice constant corresponding to minimum energy is found to be 3.92 Å.

5.2 EMT results for Pt/Pt (111)

5.2.1 Downstepping of a Pt adatom at A- and B-steps

The energy barriers for the downstepping of a Pt adatom at both A- and B-type of steps on Pt(111) were calculated using EMT potential function. The results are shown in Fig.5.8. For the B-step, the energy barrier was found to be 0.39 eV at the straight step, 0.45 eV for at a kink, and 0.29 eV Fig.5.8 near a kink. This shows that downstepping near a kink where an atom is at the end sitting next to the corner atom of a kink is significantly faster than downstepping into a kink site. The energy along all three paths are shown in order to allow clear comparison between the mechanisms in Fig.5.9. A similar trend was found for the A-type step as shown in Fig.5.10, although here the two mechanisms involving the kink site have similar activation energy. The activation energy for downstepping at an A-step is higher than at B-type step.

The activation energy for moving around the corner atom at a kink was also calculated. Both hopping and exchange mechanisms were calculated. This mechanism is important if the downstepping is such that an atom lands near but not at a kink site. If the atom cannot move into the kink site, then such downstepping events lead to the formation of more kinks and can contribute to re-entrant layer-by-layer growth mode. The energy barriers moving around the corner atom at a kink on B-step via the hopping mechanism was calculated to be 0.48 eV, as shown in Fig. 5.12(a), while for the exchange mechanism a barrier of 0.70 eV was found, as shown in Fig. 5.12(b). The activation energy for moving around kink within a layer significant, so down-stepping near a kink will likely promote the formation of more kink sites.

Similar calculations of motion around the corner atom at a kink on A-step gave similar results. For the hopping mechanism the activation energy was found to be 0.50 eV as shown in Fig.5.13 (a), while the exchange mechanism has activation energy of 0.69 eV as shown in Fig.5.13(b).

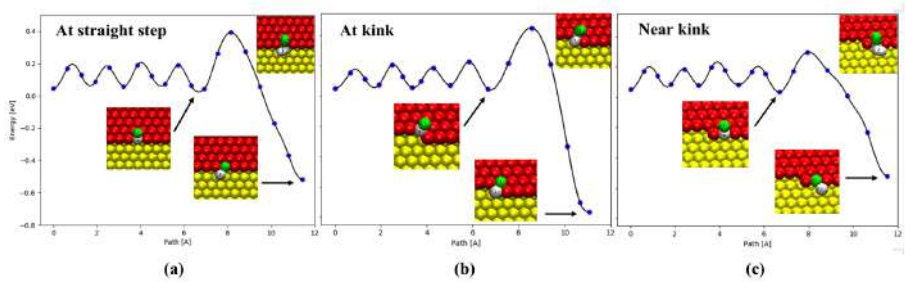

Figure 5.8. Downstepping of Pt adatom at B-step calculated using the EMT potential function. Energy along minimum energy paths for descent of an adatom at straight step, at kink site and near a kink on B-step. (a) At the end of downstepping at a straight step, a step atom has been pushed to a fivefold coordinated site. (b) At the end of downstepping at a kink site, an atom has been placed in the sixfold coordinated kink site. (c) At the end of downstepping near a kink, a step atom has been pushed to a fivefold coordinated site. Even though this process has higher final state energy than that in (b), it has lower activation energy and the final state promotes the formation of additional kink sites.

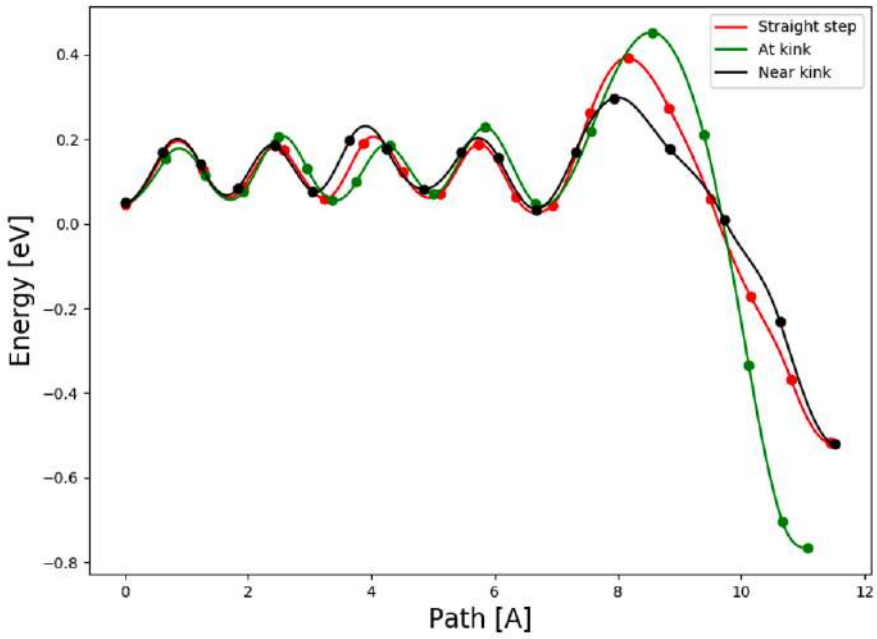

Figure 5.9. The three graphs in Fig.5.8 merged together in order to better compare the energy barriers. Red line represents the minimum energy path for descent of Pt adatom at straight B-type step, black line represents the descent path near a kink while the green line represents path for descent at a kink. The activation energy for descent near a kink is lower even though the final state has higher energy than descent at a kink.

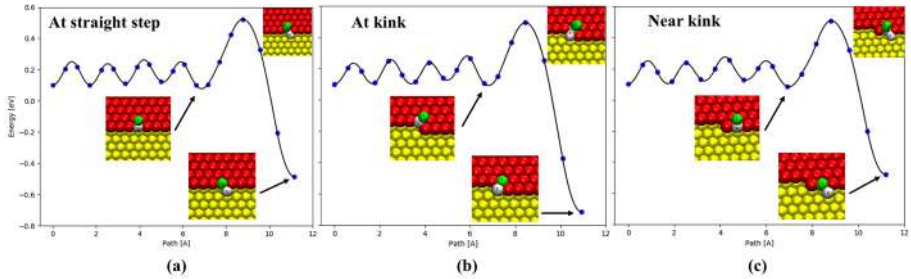

Figure 5.10. Downstepping of Pt adatom at A-step calculated using the EMT potential function. Energy along minimum energy paths for descent of an adatom at straight step, at kink site and near a kink on B-step. (a) At the end of downstepping at a straight step, a step atom has been pushed to a fivefold coordinated site. (b) At the end of downstepping at a kink site, an atom has been placed in the sixfold coordinated kink site. (c) At the end of downstepping near a kink, a step atom has been pushed to a fivefold coordinated site. Even though this process has higher final state energy than that in (b), it has lower activation energy and the final state promotes the formation of additional kink sites.

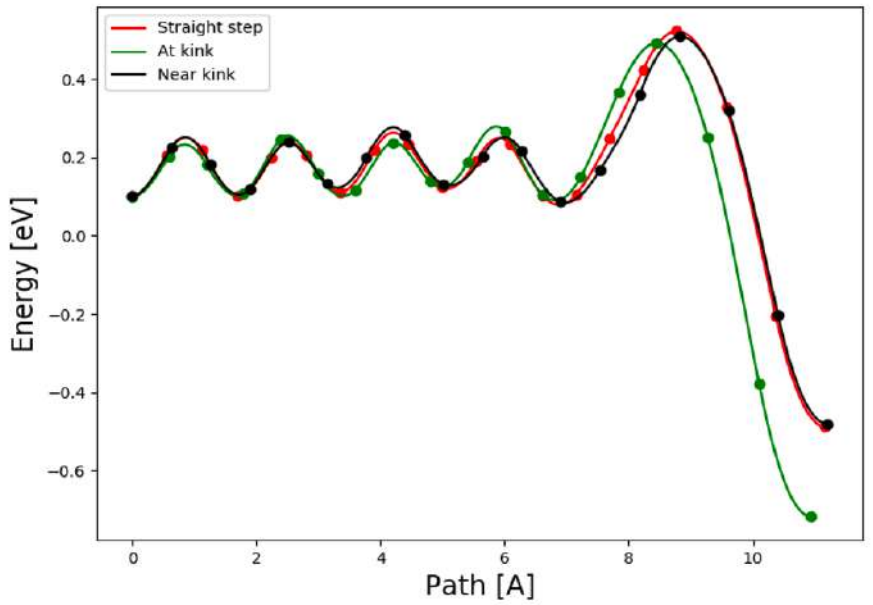

Figure 5.11. The three graphs in Fig.5.10 merged in order to compare the energy barriers. Red line represents the minimum energy path for descent of Pt adatom at straight A-type step, black line represents descent near a kink while green line represents descent at a kink. The activation energy barrier near kinks is lower than at kinks or straight edges, similar to the trend found for B-type step.

5.2.2 Rounding the corner at a kink

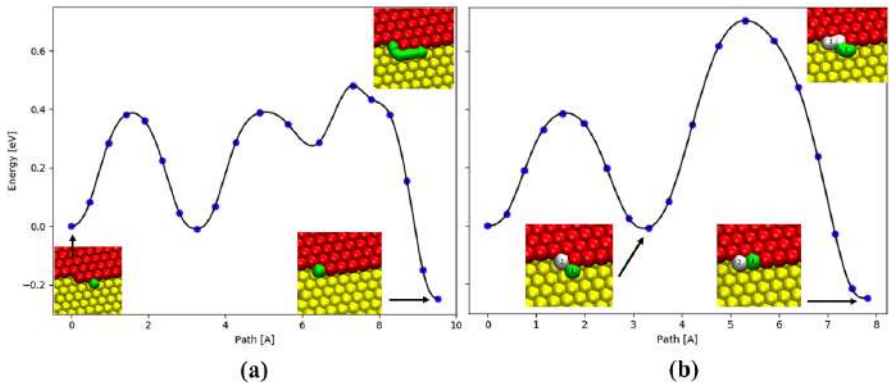

Figure 5.12. Calculations of the hopping (a) and exchange (b) processes of Pt adatom moving around the corner atom at a kink on B-type step, using the EMT potential function. Two paths are shown. In both cases the adatom starts from a fivefold coordinated site. The energy barrier for the exchange mechanism is calculated to be 0.70 eV which is higher than the barrier of 0.48 eV for the hopping process.

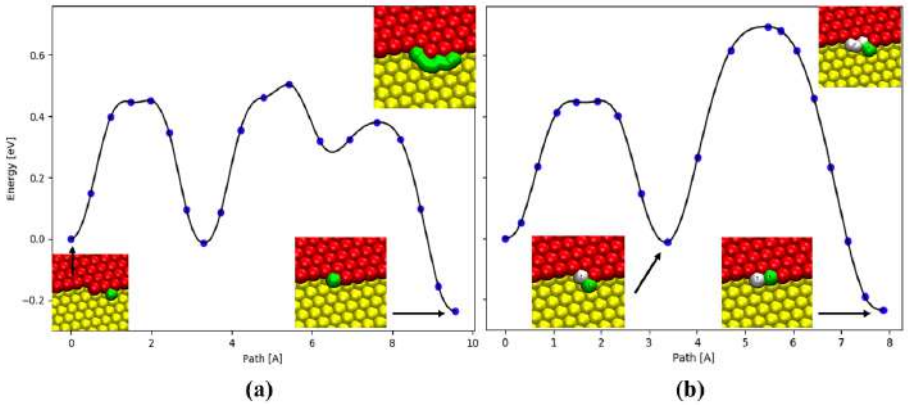

Figure 5.13. Hopping (a) and exchange (b) processes of Pt adatom moving around the corner atom at a kink on A-type step on Pt (111) calculated using the EMT potential function. Two paths are shown. In both cases the adatom starts from a fivefold coordinated site. The energy barrier for the exchange mechanism is calculated to be 0.69 eV which is higher than the barrier of 0.50 eV for the hopping process.

5.3 DFT/PBEsol results for Pt adatom downstepping

In order to study these processes with higher accuracy, DFT/PBEsol calculations were carried out for all the processes discussed above. There, the system was smaller due to the larger computational effort in the electronic structure calculations. The energy barrier was calculated to be 0.45 eV for descent at straight B-step as shown in Fig. 5.14(a), while it was 0.30 eV for downstepping near kink as shown in Fig. 5.14(c) and 0.38 eV for downstepping at a kink as shown in Fig. 5.14(b). Consistent with the EMT calculations, these results show that downstepping near kinks is significantly faster than downstepping at kinks or at straight steps. The results are qualitatively similar.

Simmilar trend was found for A-type steps. The energy barrier was calculated to be 0.44 eV at straight A-type step (see Fig. 5.15(a)), 0.33 eV for downstepping near kink (see Fig. 5.15(c)), and 0.35 eV for downstepping at kink (see Fig. 5.15(b)). The difference between downstepping near and at kinks is not significant, but the activation energy for downstepping at a straight step is clearly higher. The lowest downstepping process of all six paths studied is near a kink on the B-type step. These results are sumarized in Table 5.3.

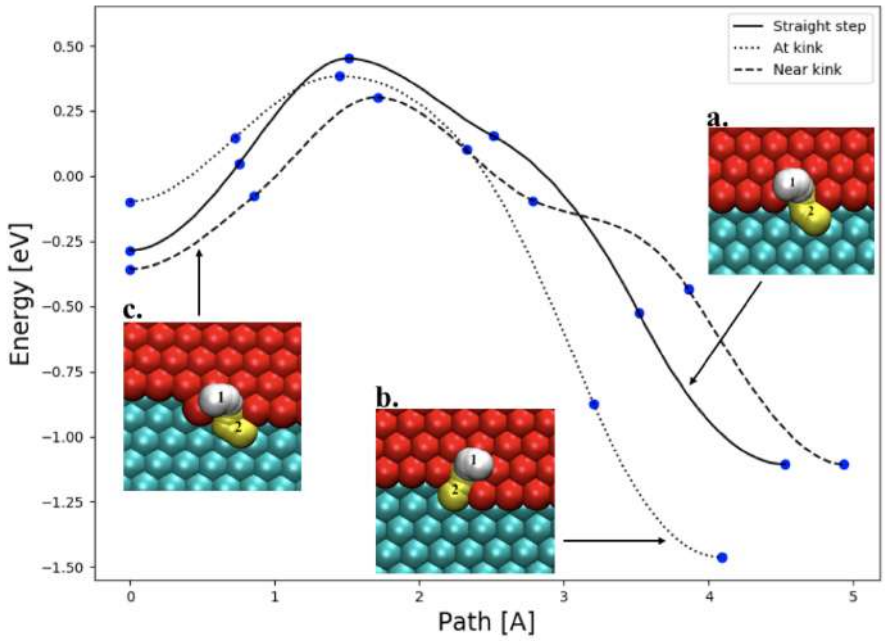

Figure 5.14. Minimum energy paths for downstepping of a Pt adatom at a B-type step on Pt(111) surface calculated using density functional theory. The zero of energy corresponds to an adatom on the flat (111) surface. Three paths are shown: At straight step (solid line), see inset (a); at kink (dotted line), see inset (b); and near kink (dashed line) see inset (c). Downstepping near a kink has lower ativation energy than at a kink even though it leads to higher final state energy.

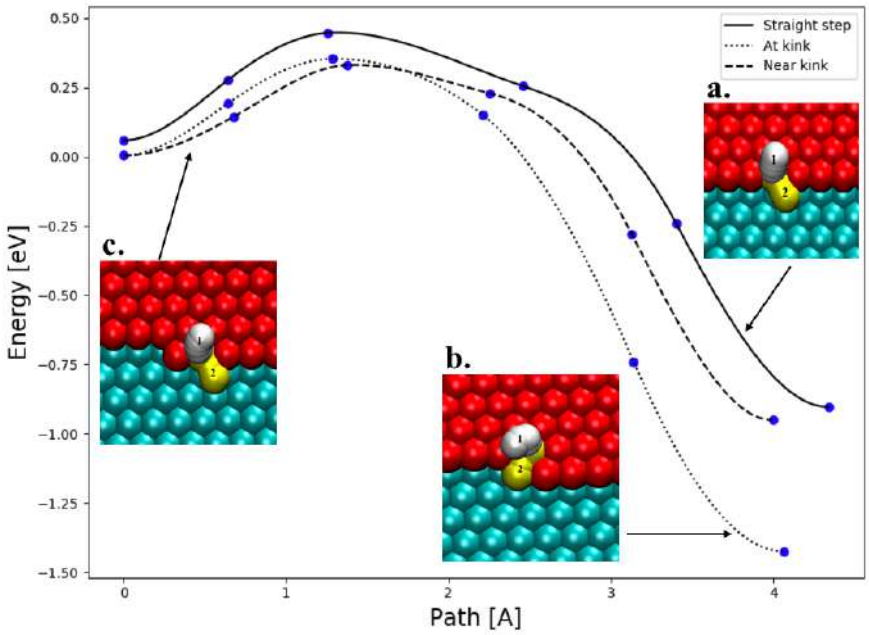

Figure 5.15. Minimum energy paths for downstepping of a Pt adatom at an A-type step on Pt(111) surface calculated using density functional theory. The zero of energy corresponds to an adatom on the flat (111) surface. Three paths are shown: At straight step (solid line), see inset (a); at kink (dotted line), see inset (b); and near kink (dashed line) see inset (c). Downstepping near a kink has lower ativation energy than at a kink even though it leads to higher final state energy.

Table 5.3. Results of DFT/PBEsol calculations of the activation energy for adatom descent at A- and B-type steps, with and without kink sites. The activation energy is the saddle point energy minus the energy of an adatom at an FCC site of the flat (111) surface.

Step type	Mechanism	Activation energy
A		
	straight	0.44
	at kink	0.35
	near kink	0.33
B		
	straight	0.45
	at kink	0.38
	near kink	0.30

5.3.1 Rounding the corner at a kink

After downstepping near a kink, an atom is sitting at the step edge in a fivefold coordinated site. It is then close to the sixfold coordinated kink site which offers significantly higher binding energy. The question therefore arises whether the atom can round the corner and enter the kink site. DFT/PBEsol calculations of minimum energy paths for both a hop and a concerted displacement mechanism for this process were carried out. The results for the B-type step are shown in Fig. 5.16. Both transition mechanisms are found to correspond to high activation energy, 0.97 eV for the hop and 1.27 eV for the concerted exchange. This process will, therefore not occur at a significant rate at room temperature. The atom that lands in a fivefold coordinated site at step edge is, therefore, not likely to enter the fixfold coordinated kink site but will instead more likely represent the beginning of a new step row and eventual formation of new kink sites.

Similar calculations for the rounding of a corner atom on the A-type step gave similar results as shown in Fig. 5.17. The energy barriers are found to be 0.91 eV for the hop mechanism, while via concerted displacement mechanism has a barrier of 1.27 eV.

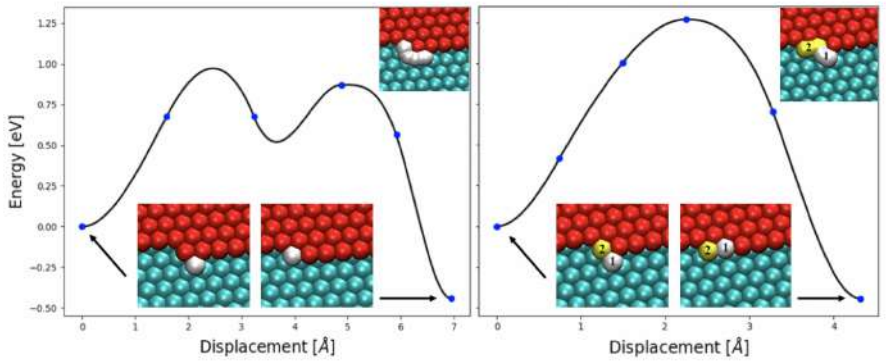

Figure 5.16. Hopping (a) and concerted displacement (b) processes for the transition from a Pt adatom at an A-type step to enter a kink site. Both mechanisms correspond to high energy barrier, on the order of 1 eV, so this process is not active at room temperature.

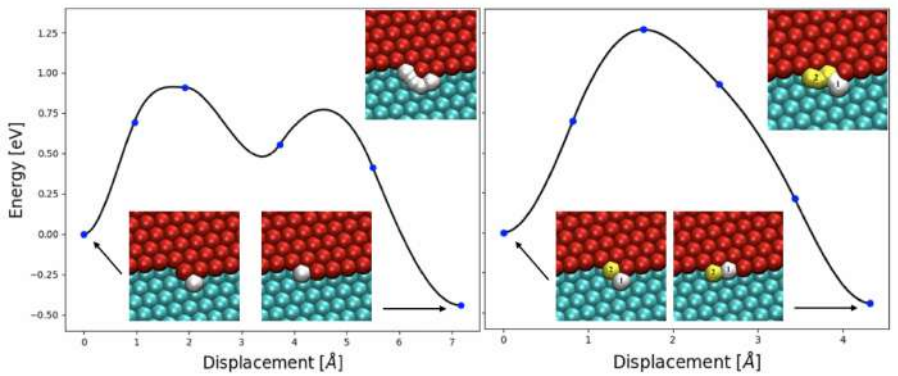

Figure 5.17. Hopping (a) and concerted displacement (b) processes for the transition from a Pt adatom at a B-type step to enter a kink site. Both mechanisms correspond to high energy barrier, on the order of 1 eV, so this process is not active at room temperature.

The results of the calculations presented above illustrate that there are a number of important processes relevant to the fate of an adatom that lands on top of an island, and thereby the question whether deposition of atoms on the surface leads to 2D or 3D growth. Some of these features are subtle and unexpected. The challenge to the theoretical studies is to identify the relevant processes and estimate the rate of these processes accurately enough to be able to explain the surface patterns observed in experimental measurements. The most serious challenge to theoretical studies is the problem of identifying the relevant processes.

As the calculations on Pt(111) presented here illustrate, the key process may be non-intuitive, as the near but not at kink sites, shown in figures 5.14 and 5.15. This calls for algorithms that can find what processes would occur in the simulated system if direct classical dynamics simulations could be carried out long enough to cover experimental time scales. Long time scale simulation approaches such as the adaptive kinetic Monte Carlo method (Henkelman and Jónsson, 2001) can in principle be used in such studies, but the problem is that the DFT calculations are computationally very demanding, too much so to make such calculations practical at the present time. Empirical potential functions such as EAM and EMT are fast enough, but are too approximate, although they have been used successfully to identify soe unexpected mechanisms.

A possible future direction in this respect is the use of machine learning to interpolate between calculated DFT results. The question still remains whether such an approach can be trusted to provide unexpected results since it represents only an interpolation between results fed into the machine learning as a training set. The challenge of explaining how microscopic processes influence macroscopic behavior is particularly relevant in studies of growth shapes of crystals, which offer a unique testing ground for the computational challenges of bridging vast length and time scales.

5.4 Au crystal calculations using EMT potential

Calculations of a Au crystal were done using EMT with readily available parameters in the potential energy function. Fig. 5.18 describes the equation of state, where bulk modulus for Au crystal was calculated. Bulk modulus for Au crystal was found to be 174 GPa by using EMT potential, in good agreement with the experimental value of 169 GPa. The cohesive energy for Au was calculated to be 3.80 eV, also in good agreement with the experimental value of 3.93 eV.

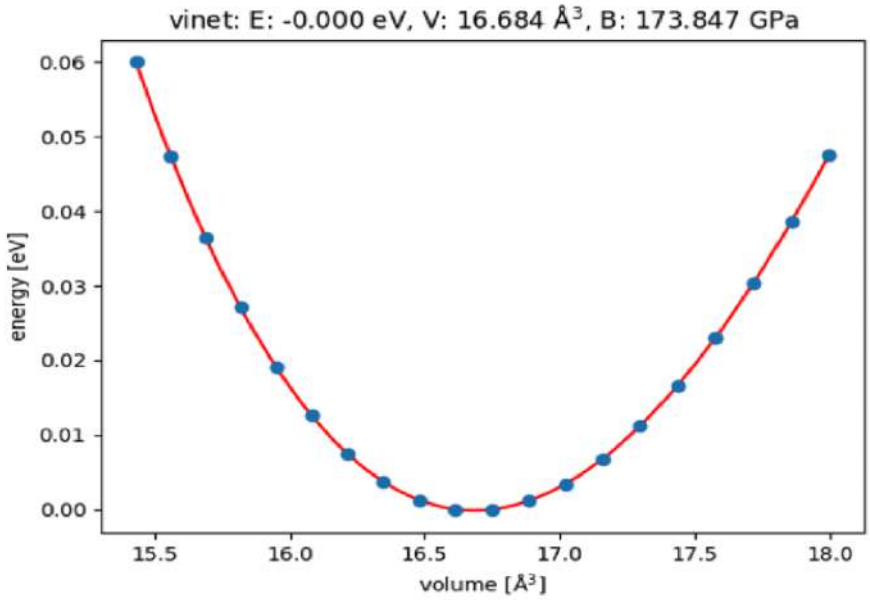

Figure 5.18. Equation of State graph for Au crystal

	Bulk Modulus (B)	Cohesive energy (E_c)
Exp. Values	169 GP a	- 3.93 eV
EMT. Values	173 GP a	- 3.80 eV

Figure 5.19. Comparison of calculated results for Au crystal using EMT potential function with experimental values.

5.5 EMT results for Au adatom

5.5.1 Downstepping of Au adatom at steps

The energy barriers for the down stepping of a Au adatom at both A- and B-type steps on Au (111) were calculated using the EMT potential function. The energy barriers for these processes were found to be 0.22 eV at straight B-edge as shown in Fig. 5.20(a), 0.27 eV for downstepping at a kink on the B-step as shown in Fig. 5.20(b), and 0.17 eV for downstepping near a kink as shown in Fig. 5.20(c). This shows that downstepping near kinks is significantly faster than downstepping at kinks or at straight edges. Also, similar trend was found for A-type steps, for straight edge as shown in 0.31 eV Fig. 5.21(a), 0.32 eV for downstepping at kink on the A-stp as shown in Fig. 5.21(b), and 0.29 eV for downstepping near a kink as shown in Fig. 5.21(c). The energy barriers are higher than at the B-type step.

The activation energy for moving around the corner atom at the kinks were also calculated. The energy barrier for hopping around the corner at a kink on B-type step was found to be 0.33 eV, see Fig. 5.24(a), while the concerted displacement mechanism gave 0.47 eV, see Fig. 5.24(b). The activation energy for moving around corner atom at a kink within a layer is not so high in this case.

Similar calculations for the A-type step gave similar trend. The energy barrier for moving around the corner atom by hopping mechanism was calculated to be 0.35 eV, see Fig.5.25(a), while via exchange mechanism barrier was 0.46 eV, see Fig.5.25(b).

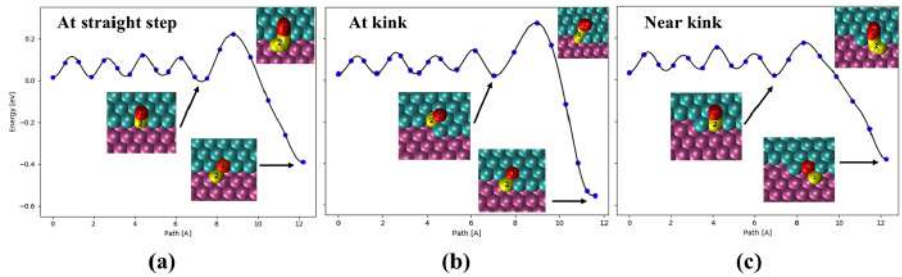

Figure 5.20. Downstepping of Au adatom at B-edge on Au (111) island.

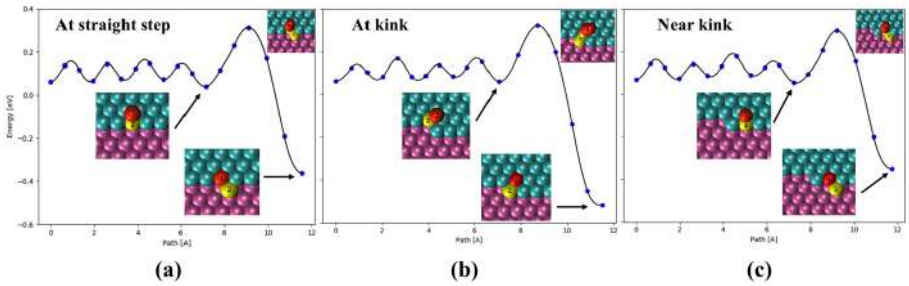

Figure 5.21. Downstepping of Au adatom at A-type step.

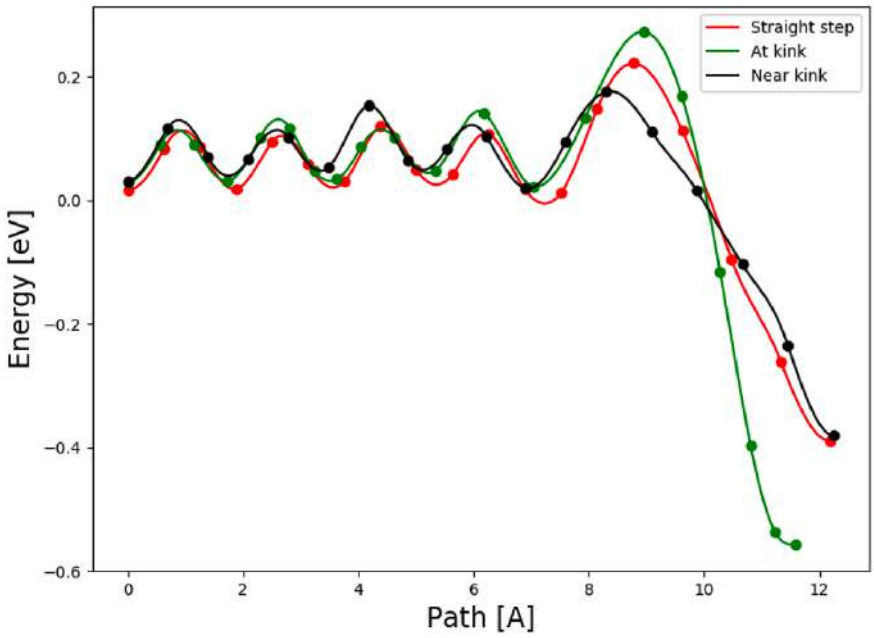

Figure 5.22. Comparison of the three mechanisms studied for downstepping of a Au adatom at a B-type step. (Red line) represents the minimum energy path for descent at straight step; (Black line) represents the minimum energy path for downstepping near a kink; (Green line) represents the minimum energy path for downstepping at a kink. The activation energy barrier for downstepping near a kink is lowest.

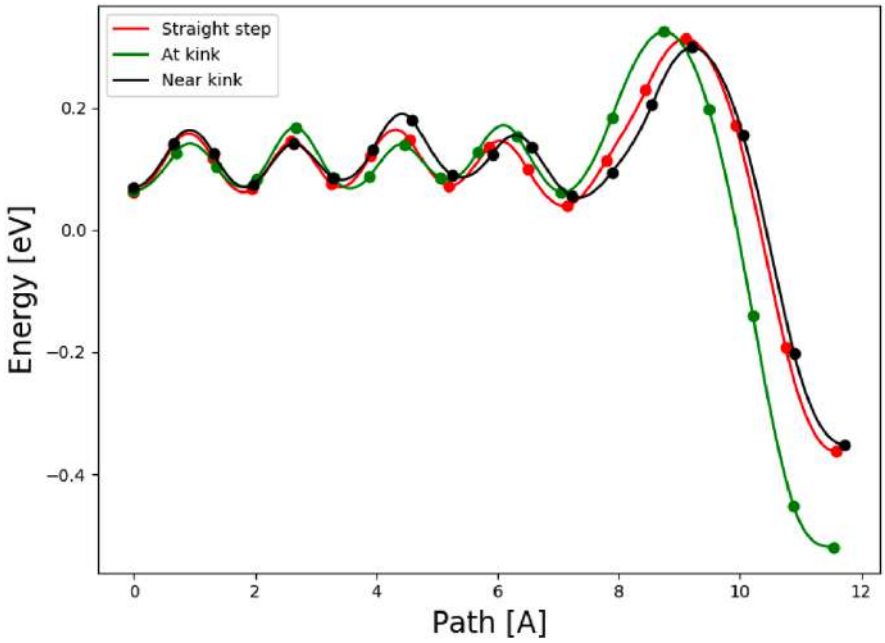

Figure 5.23. Comparison of the three mechanisms studied for downstepping of a Au adatom at a A-type step. (Red line) represents the minimum energy path for descent at straight step; (Black line) represents the minimum energy path for downstepping near a kink; (Green line) represents the minimum energy path for downstepping at a kink. The activation energy barrier near kink is lower than at kinks and at straight edges.

5.5.2 Rounding a corner atom at a kink

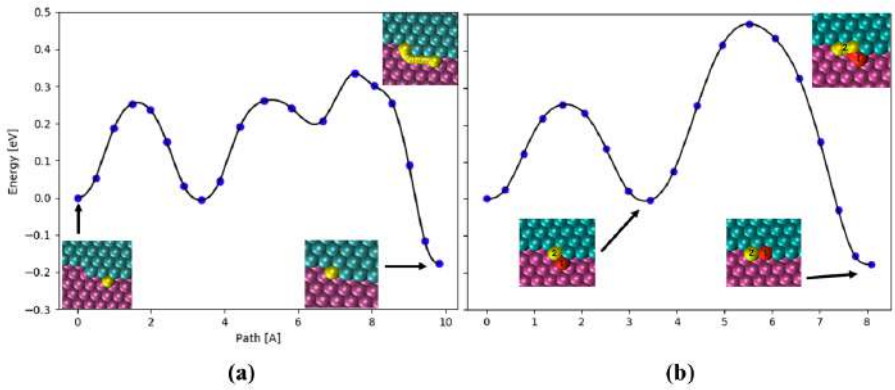

Figure 5.24. Hopping (a) and exchange (b) processes for Au adatom moving around the corner atom at a kink on an B-type step calculated using EMT potential function. The minimum energy paths for hopping and exchange are shown. The energy barrier for exchange mechanism is calculated to be 0.47 eV which is slightly higher than the barrier 0.33 eV for hopping process.

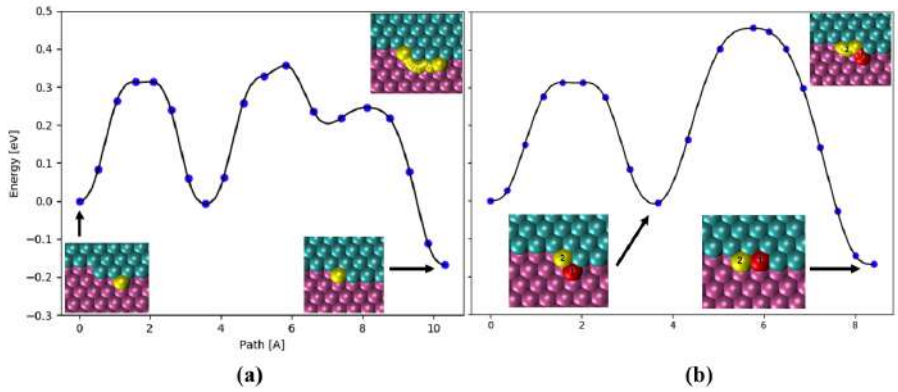

Figure 5.25. Hopping (a) and exchange (b) processes for Au adatom moving around the corner atom at a kink on an A-type step calculated using EMT potential function. The minimum energy paths for hopping and exchange are shown. The energy barrier for exchange mechanism is calculated to be 0.46 eV while the barrier is 0.35 eV for the hop mechanism.

5.6 DFT/PBEsol results for Au/Au (111)

In order to study these processes with higher accuracy, DFT/PBEsol calculations were carried out for both A- and B-type steps with and without kinks. The simulated system is necessarily smaller than in the EMT calculations because of the larger computational effort. The NEB method was used to find minimum energy paths for descent of a Au adatom at straight step, near kink and at kink on both A- and B-type steps. Unlike the EMT calculations, only the last exchange descent process was calculated in the DFT/PBEsol calculations. The initial guesses for the minimum energy paths in DFT/PBEsol calculations were taken from the EMT calculations. The energy barriers for downstepping were calculated to be 0.31 eV for straight B-type step, as shown in Fig. 5.26(a), 0.14 eV for downstepping near kink as shown in Fig. 5.26(c) and 0.20 eV for downstepping at a kink as shown in Fig. 5.26(b). As in the EMT calculations, downstepping near kinks is significantly faster than downstepping at kinks or at straight B-type steps so qualitatively similar results are obtained with the two approaches.

For the A-type steps, the DFT/PBEsol calculations gave somewhat different results than the EMT calculations. The energy barriers were calculated to be 0.25 eV at straight for A-edge as shown in Fig. 5.27(a), 0.17 eV for downstepping near a kink as shown in Fig. 5.27(c), and 0.16 eV fordown stepping at a kink as shown in Fig. 5.27(b). In this case downstepping near and at kink has similar activation energy, while downstepping at straight step is higher, as in the EMT calculations.

The results of the DFT/PBEsol calculations of the activation energy for adatom

descent at A- and B-type steps are summarized in Table 5.4.

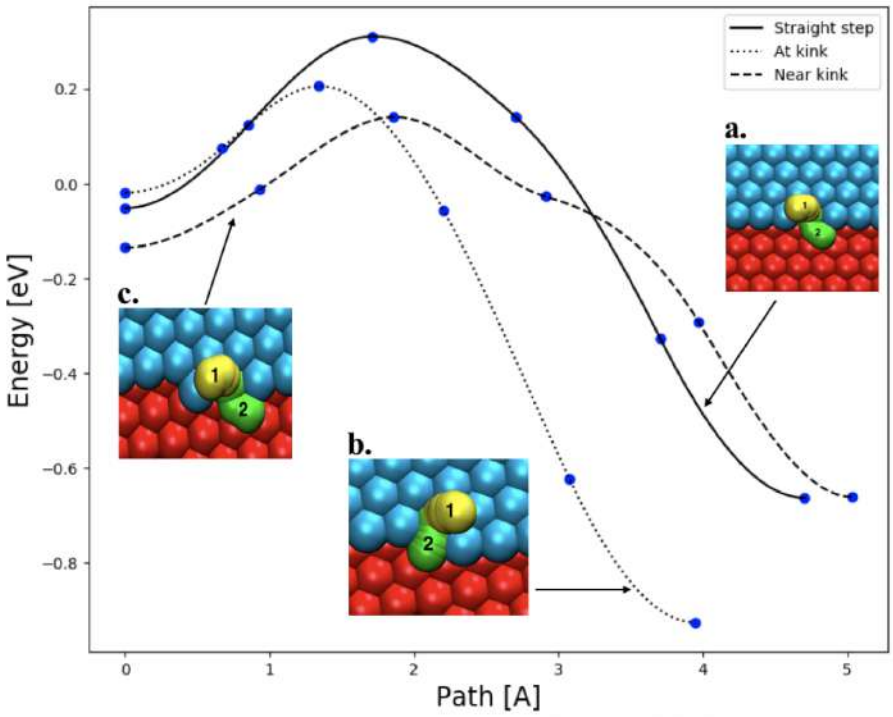

Figure 5.26. Results of minimum energy path calculations for descent of a Au adatom at B-type step based on DFT/PBEsol energetics. Three paths are shown. Solid line corresponds to downstepping at a straight step, see inset (a). The initial position of the adatom is labled with 1. It undergoes a concerted displacement process with a step atom as it descends. At the end, an edge atom has been pushed into a fivefold coordinated site. Dotted line corresponds to downstepping into a kink site, see inset (b). During this process, an eightfold coordinated kink atom is pushed to a sixfold coordinated site. Dashed line corresponds to corresponds to downstepping near a kink site, see inset (c). During this process a sevenfold coordinated edge atom is pushed to a fivefold coordinated site.

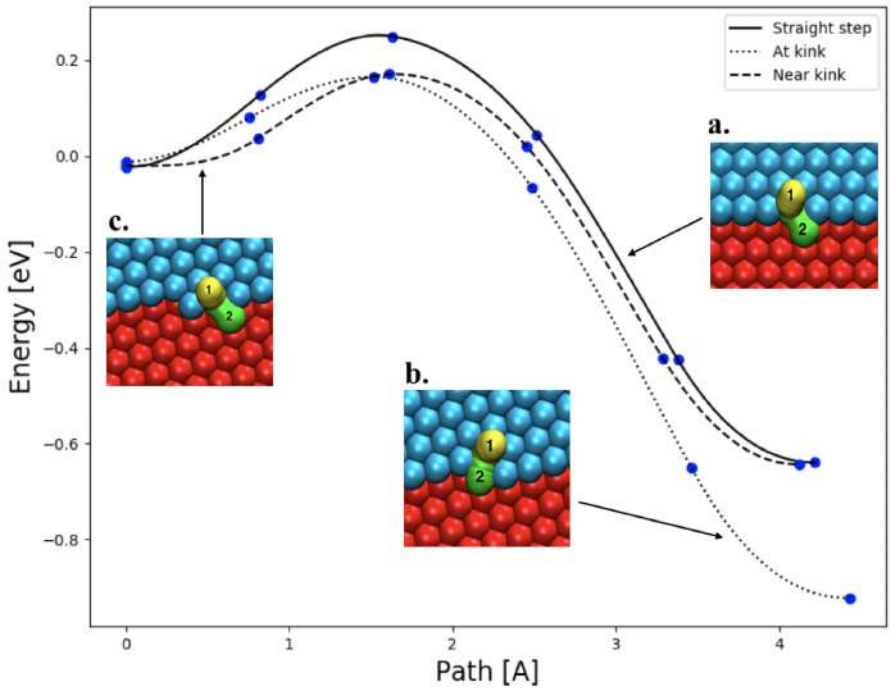

Figure 5.27. Results of minimum energy path calculations for descent of a Au adatom at A-type step based on DFT/PBEsol energetics. Three paths are shown. Solid line corresponds to downstepping at a straight step, see inset (a). The initial position of the adatom is labled with 1. It undergoes a concerted displacement process with a step atom as it descends. At the end, an edge atom has been pushed into a fivefold coordinated site. Dotted line corresponds to downstepping into a kink site, see inset (b). During this process, an eightfold coordinated kink atom is pushed to a sixfold coordinated site. Dashed line corresponds to corresponds to downstepping near a kink site, see inset (c). During this process a sevenfold coordinated edge atom is pushed to a fivefold coordinated site.

Table 5.4. Summary of calculated activation energy for downstepping obtained from NEB calculations with DFT/PBEsol energetics. The activation energy is the saddle point energy minus the energy of the adatom at an FCC site of an extended (111) surface.

Step type	Mechanism	Activation energy
A		
	straight	0.25
	at kink	0.16
	near kink	0.17
B		
	straight	0.31
	at kink	0.20
	near kink	0.14

5.6.1 Rounding a corner

The paths for both hop and exchange mechanisms for an adatom to move from a site at the step edge to a kink site was also calculated with DFT/PBEsol. The energy barriers were found to be 0.46 eV for hop and 0.78 eV for concerted displacement at the B-type step, as shown Fig. 5.28, while the values are 0.53 eV and 0.76 eV for the A-type step, as shown in Fig. 5.29. Again, the energy barriers for hopping mechanisms are found to be lower than for the exchange on both at A- and B-type steps, similar to the results found from the empirical EMT potential function.

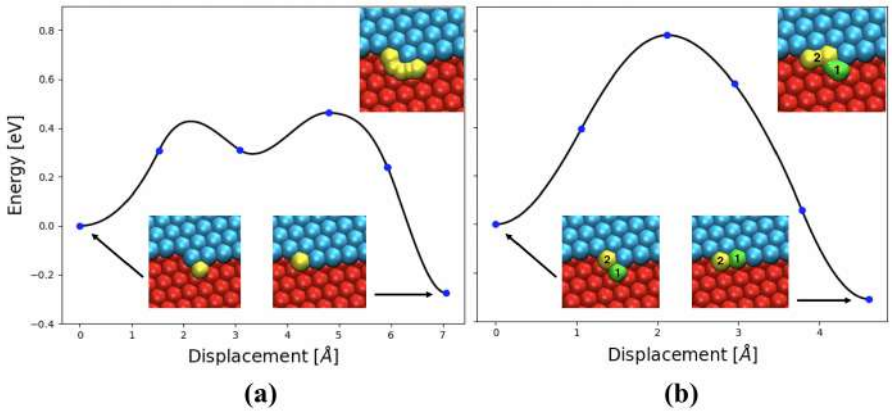

Figure 5.28. Hopping (a) and exchange (b) processes for a Au adatom to move around the corner at a kink on B-type step.

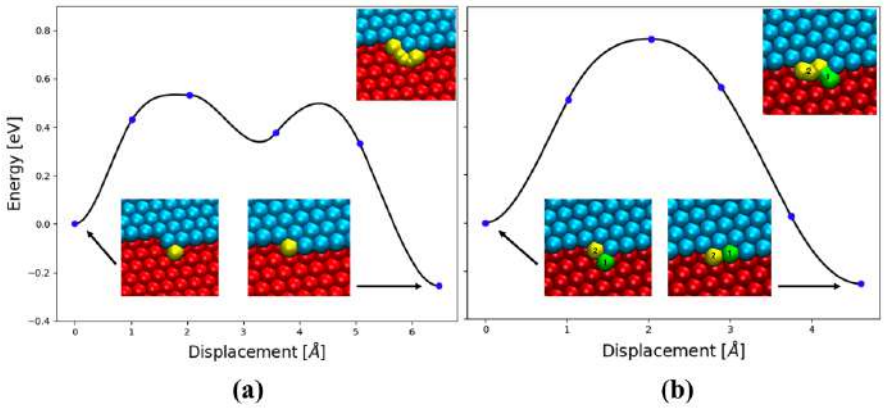

Figure 5.29. Hopping (a) and exchange (b) processes for a Au adatom to move around the corner at a kink on A-type step.

The calculations presented above indicate that a Au adatom on top of an island on a Au(111) surface can descend to the lower layer most easily near a kink on a B-type step. This is similar to what has previously been deduced from calculations for a Pt adatom on a Pt(111) surface (Villarba and Jónsson, 1994; Jonsson, 2000) and what has been observed experimentally for a Co adatom on a Pt(111) surface (Lundgren et al., 1999). This non-intuitive mechanism was first predicted from extensive study of various mechanisms using an EAM potential function for the Pt/Pt(111) system (Villarba and Jónsson, 1994). It can explain the observed re-entrant layer-by-layer growth mode of Pt(111) and since the same feature is found here in the energy landscape for a Au adatom on Au(111), the indication is that Au(111) also can show re-entrant layer-by-layer growth. The sites adjacent to and above the B-type step offer 0.03 eV stronger binding than corresponding sites on the A-type step, so adatoms will tend to migrate to the B-type step. As the energy barrier for rounding the corner into a kink site is more than three times larger than the energy barrier for descent, there will be a range in temperature where descent is active but rounding the corner is not, so the step edge will become rough with multiple kinks, each offering a low energy path for descent, and thereby promoting layer-by-layer growth.

The results presented above demonstrate the complexity of the energy landscape and the importance of choosing a single reference point for the energy of the adatom. If the activation energy of a downstepping event is simply taken to be the energy maximum along the minimum energy path minus the energy of the initial state for the elementary event, then the comparison between A- and B-type steps will be incorrect. The initial state for the downstepping event is higher in energy at the A-type step than at the B-type step because it corresponds to an HCP site rather than an FCC site. The initial site for the descent near a kink on the B-type step is even lower in energy, as can be seen in Fig. 5.26. The proper energy reference for all the adatom descent mechanisms is the energy of the adatom in an FCC site of a flat terrace since this represents the majority species.

A possible future direction in this respect is the use of machine learning to interpolate between points in a training set of DFT calculations. The question still remains whether such an approach can be trusted to provide unexpected results since it represents only an interpolation between results fed into the machine learning algorithm. The most relevant part of the energy surface, corresponding to non-intuitive and unexpected mechanisms may be incorrectly represented since the training set will likely not contain such configurations. The challenge of explaining how microscopic processes influence macroscopic behavior is particularly relevant in studies of growth shapes of crystals, which offer a unique testing ground for the computational challenges of bridging vast length and time scales.

5.7 Au adatom on the Si(100)-2×1 surface

Mtallic nanostructures on surfaces can have special and important properties for research and technological applications (Zhang et al., 2013). This includes interesting optical, electronic, and catalytic properties (Link and El-Sayed, 2000; Roduner, 2006). In particular, gold nanostructures on silicon surfaces are of interest for numerous applications. For example, gold nanoparticles and gold nanoislands formed on a silicon surface can be used in the synthesis of one-dimensional nanostructures such as carbon nanotubes (Bhaviripudi et al., 2007) and silicon nanowires (Hannon et al., 2006). They have also been found to display optical properties (Minoda and Yamamoto, 2005), and to form mesoscopic structures (Choi et al., 2008). Moreover, the presence of a gold layer on a silicon surface has proven to play a key role on the silicon oxide growth mechanism (Leclerc et al., 1992) and other materials (Cheng and Chen, 2008).

An understanding of the initial stages of gold cluster formation on silicon is important for choosing the right conditions for the desired growth mechanism. With that aim, several experimental techniques such as scanning tunneling microscopy (STM) have been proposed to study the growth of gold clusters on a silicon surface (Kim et al., 1996; Akira et al., 1992; Chiaravalloti et al., 2009). However, the diffusion mechanism of the Au adatoms on the Si(100) surface is still not known, Although some preliminary work has been done to identify the binding sites and diffusion mechanism of Au adatoms on the Si(100) surface (Ju et al., 2008; Chiaravalloti et al., 2009), there are still many open questions.

In this part of the thesis, a theoretical study of the adsorption sites and diffusion processes of a single gold atom on the Si(100)2×1 surface are studied using the NEB method with energy and atomic forces estimated from DFT calculations with the PBEsol functional. Additionally, two Si-Au angular-dependent potential (ADP) functions developed by Starikov et al. (Starikov et al., 2018, 2020) are tested and used in extended time scale KMC simulations.

It is well known that the Si(100) surface undergoes a reconstruction to form a periodic 2×1 unit cell where the silicon dimer rows are formed after a surface rearrangement. We started our calculations from the unreconstructed Si(100) surface, with two dangling bonds for every surface Si atom. In Fig. 5.30 we show the top (a) and side (b) views of the clean Si(100)2×1 surface after optimisation with DFT/PBEsol. The distinctive buckling dimer rows that have been observed before both experimentally and theoretically are highlighted with a different color. In our calculations, we obtain a dimer bond length of 2.34 Å and a buckling angle of 19.8° after reconstruction. This agrees well with data obtained from low energy electron diffraction experiments (LEED), Over *et al.* (Rietig et al., 2020) report values of 2.24 Åand 19.2° for the dimer bond length and buckling angle, respectively. It is worth noting that the calculations using ADP18 and ADP20 result in the rearrangement where the silicon dimers are formed without the buckling, (*i. e.* the Si dimers remain parallel to the surface).

An STM measurement by Chiaravalloti *et al.* (Chiaravalloti et al., 2009) shows that the most favorable adsorption sites for a single Au atom on the Si(100)-2×1 surface are between silicon dimer rows (BDR) and less stable sites are found on top of the rows

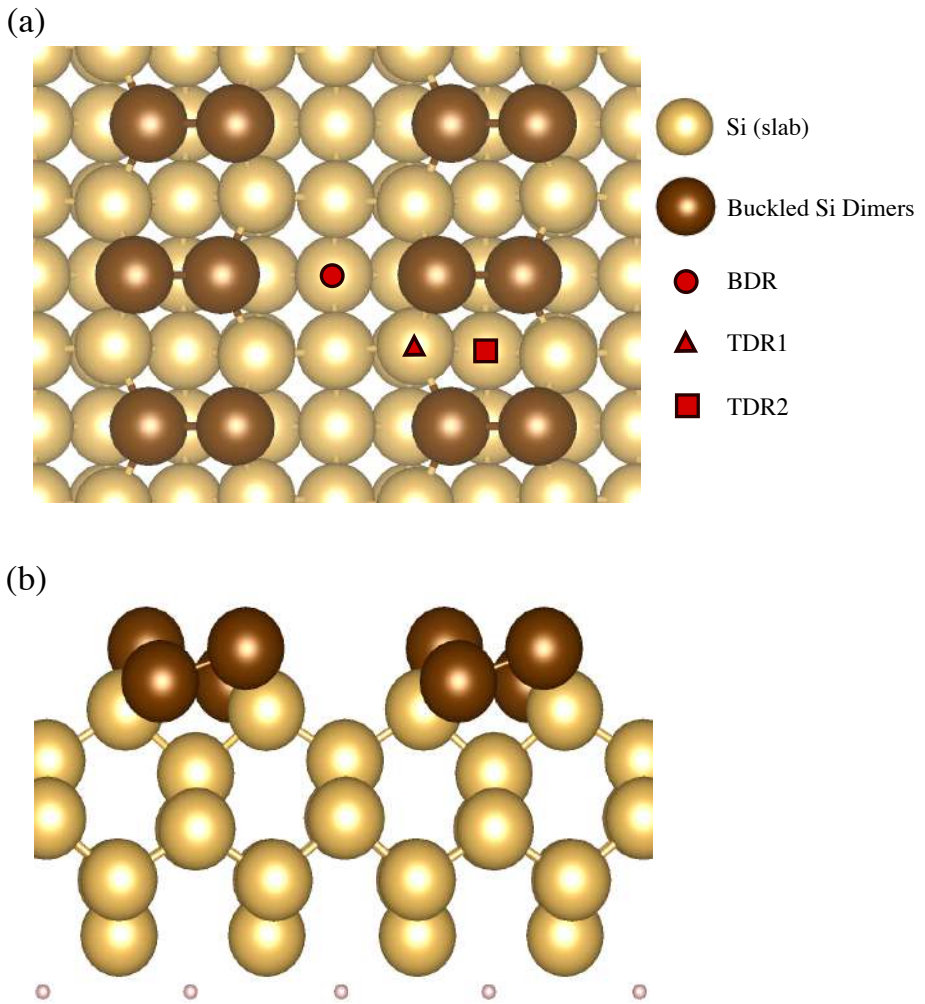

Figure 5.30. Top (a) and side (b) views of the slab used to represent the Si(100)2×1 surface. The atom coordinates in the dimer rows and the underlying layer have been optimised using DFT/PBEsol

	DFT/PBEsol	DFT/PBE[a]	Si-Au ADP18	Si-Au ADP20
BDR	3.44 (140.2°)	3.24 (131°)	4.14 (140.3°)	3.82 (160.1°)
TDR1	2.95 (99.8°)	3.03 (97.5°)	4.04 (102.9°)	3.59 (96.1°)
TDR2	2.93 (121.3°)	2.94 (117.7°)	3.99 (120.3°)	3.27 (108.3°)

Table 5.5. Binding energy (in eV) of a single Au adatom at various adsorption sites on the Si(100)-2×1 surface. The resulting Si-Au-Si angle for a given configuration is shown in brackets (in deg).
[a]Data taken from Ref. Chiaravalloti et al. (2009)

(TDR). DFT/PBE calculations carried out by the same group identified two sites on top of rows, TDR1 and TDR2. In panel (a) of Fig. 5.30, we have marked the three sites mentioned in their work. We have calculated the adsorption energies using DFT/PBEsol, as well as the Si-Au-Si angle formed after relaxation, and the results are shown in Table 5.5. From these results, we can see that the BDR position is the most stable configuration, consistent with the STM measurements Chiaravalloti et al. (2009). In our DFT/PBEsol calculations, the binding energy of the Au atom in the BDR site is around 0.5 eV higher than in the other configurations. This is a larger difference than the one obtained with PBE, where the BDR site is 0.2 eV more stable than the rest. On the other hand, the data obtained from the ADP18 calculations reveal an overestimation of the binding energies of almost 1 eV with respect to the DFT results. Using the ADP20, this overestimation is reduced, additionally, the energy difference between the three adsorption sites is increased.

In general,we can see that the same trend is obtained with the different descriptions of the Au/Si interaction, with the BDR being the most stable configuration, and the main difference being the relative stability between adsorption sites. Although the calculations with the ADP functions do not yield the buckled dimers, as expected, the resulting Si-Au-Si angles compare well to those obtained with DFT.

We have also found an additional local minimum in the BDR position, where the Au atom is located around 1 Å closer to the surface as compared to the previously known BDR. Fig. 5.31 shows a side view comparison between these two adsorption sites. The calculated binding energy for the new BDR position (BDR2) is 2.91 eV, similar to the one obtained for the TDR sites. The configuration also displays the Au atom being bonded to two Si-dimer atoms. This local minimum is not present when the ADP18 and ADP20 interaction potentials are used.

5.8 Diffusion of a Au adatom on the Si(100)-2x1 surface

In order to learn about the mechanism of the diffusion of Au adatoms on the surface, the energy barriers for transitions between the various adsorption sites needs is calculated. In Fig. 5.32 we show the calculated minimum energy paths (MEPs) between the BDR and TDR1 adsorption sites (panel a) and between the TDR1 and TDR2 sites (panel b) with energetics obtained from DFT/PBEsol, ADP18 and ADP20. The calculated energy barrier between the BDR and TDR1 site for PBEsol is 0.84 eV, much higher than the ones obtained using ADP18 (0.31 eV) and ADP20 (0.41 eV). On the other hand,

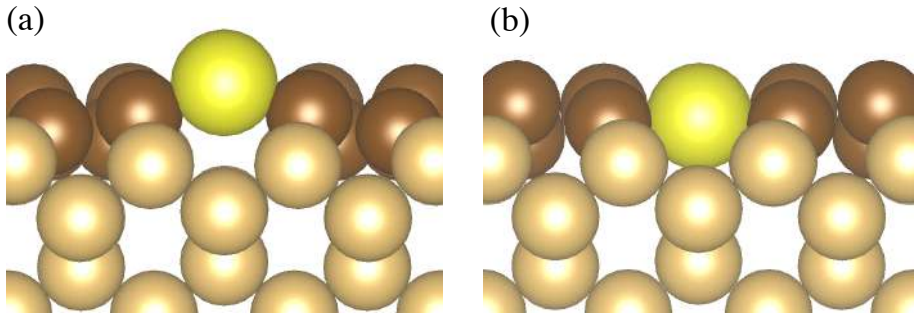

Figure 5.31. Side view of two adsorption sites found in between the silicon dimer rows (BDRs). Gold atoms are displayed in yellow and the Si-dimer atoms are coloured in brown. The calculated binding energies are: (a) 3.44 eV and (b) 2.91 eV

the calculated energy barriers between the TDR1 and TDR2 sites are similar, 0.29 eV, 0.23 eV and 0.35 eV for PBEsol, ADP18 and ADP20, respectively.

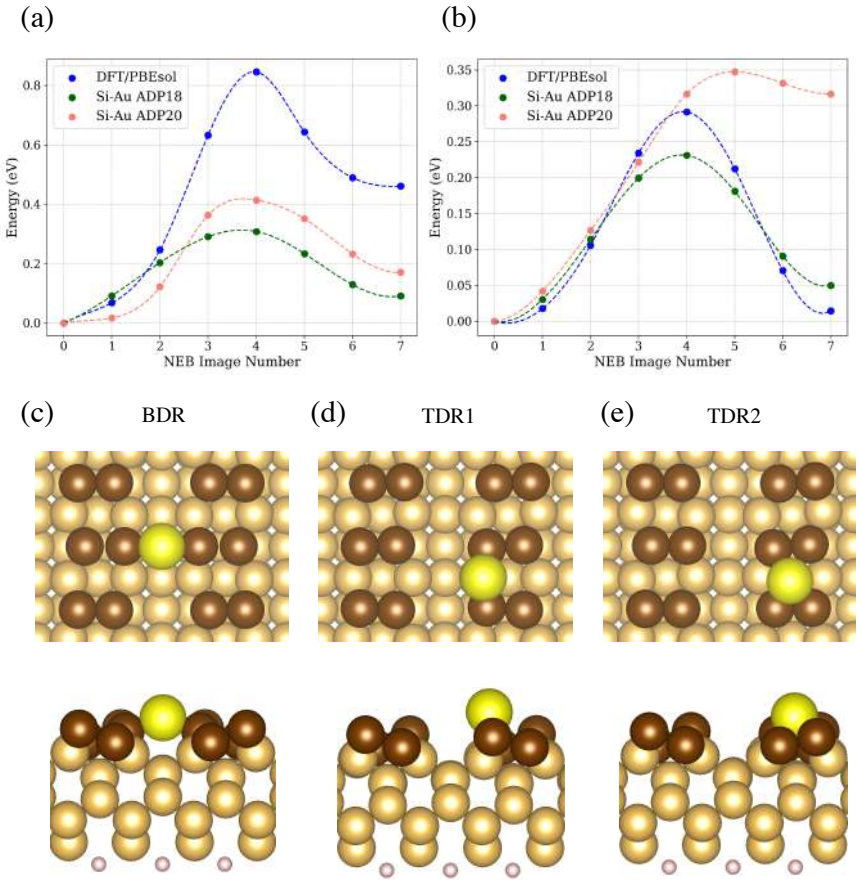

Figure 5.32. The calculated minimum energy paths (MEPs) between the BDR and TDR1 adsorption sites (panel a) and between the TDR1 and TDR2 sites (panel b) obtained with DFT/PBEsol, ADP18 and ADP20.

5.9 Short time scale simulations of Au deposition

Classical dynamics simulations have been used to model sequential deposition of Au atoms on the Si(100) 2×1 surface. For each deposition event, starting from random lateral position, a nanosecond is simulated before another atom is deposited. The short time scale in direct classical simulations is necessarily limited due to the small time step (a tenth of a vibrational period) prevents observation of diffusion events which have significant energy barrier. Also, thermal annealing which would occur in experimental deposition where the time between deposition events is many orders of magnitude longer than what can be simulated by classical dynamics. These simulations, therefore, lead to amorphous metal overlayer growth.

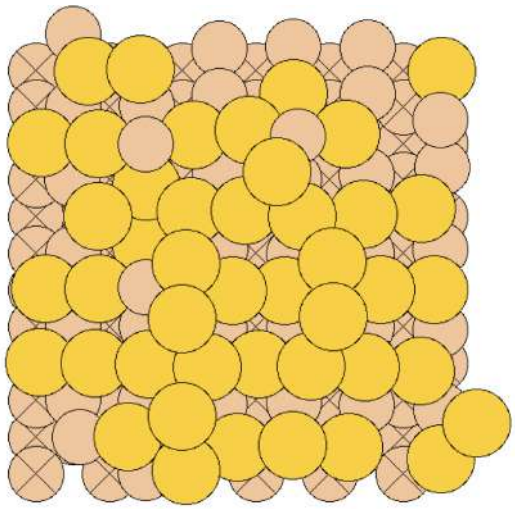

Figure 5.33. An amorphous island is formed in short timescale direct classical simulations using the ADP18 potential function.

5.10 Long timescale simulations of Au deposition and annealing

Because of the limitation of short time scale direct classical simulations, longer timescale simulations were carried out to study annealing process of the amorphous Au overlayer on the Si(100) 2×1 surface. The simulations make use of the adaptive kinetic Monte Carlo (AKMC) method. The AKMC method is used to describe thermally induced events without being limited in time scale by the fast vibrational motion of the atoms. It is based on rate theory where the focus is on activated transitions that overcome energy barriers, i.e rare events. The fast vibrational motion within a stable state is assumed to lead to thermal equilibrium and the properties of the state are described

statistically. While the short timescale direct classical simulations necessarily do not include diffusion and activated annealing events, they can be included in the AKMC simulations.

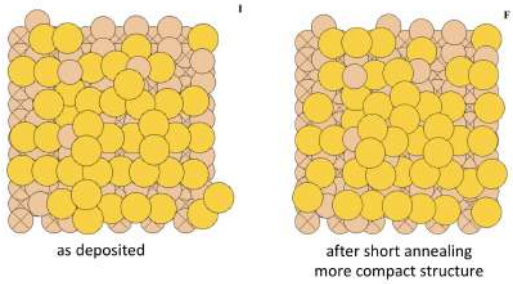

Figure 5.34. Annealing of the Au island formed (F) by fast, sequential deposition using AKMC method and the ADP18 potential function.

Long time scale simulations using the AKMC method of Au deposition on a Si (100) surface show that direct classical dynamics simulations where each atom deposition is described over one nanosecond leads to irregular, amorphous structure. Long timescale (AKMC) simulations are used to study the effect of long timescale annealing of the structure. Also, mixed classical dynamics and AKMC methods are used for multi-scale simulations of Au deposition on Si(100)-2$\times$1. The AKMC simulations show some increase in Au atom density in one region, the atoms are still distributed over the entire surface. The overestimate of the Au-Si attractive interaction by the ADP18 likely ensures that the Au atoms are spread out and do not form a surface island.

6 Summary of the articles included

6.1 Article I

In the first article, we used density functional theory (DFT) and a semi-empirical potential function, EMT, to investigate the downstepping mechanism of a Pt adatom on Pt (111) island at A- and B-type steps. The mechanism was identified by which Pt adatom that lands on top of a Pt metal island can descend to a lower layer. This is known to be a central issue determining whether the metal grows layer-by-layer or forms three dimensional islands. In this work we used kinked and stepped surfaces (of large enough size to get convergence) of Pt in EMT calculations while smaller samples were used in the DFT calculations. Minimum energy paths for the descent of Pt adatom were calculated using the NEB method. We found that DFT/PBEsol energy barriers for downstepping near kinks are lower than at kinks or straight edges on B-steps, while the barriers are roughly equal for downstepping at and near kinks on A-steps. The DFT/PBEsol results are consistent with the EMT results in that downstepping near kinks on B-type steps is the fastest process for interlayer transport. Since the energy barrier for rounding the corner atom at the kink to enter the kink site is high, donwstepping near kinks promotes the formation of more kinks and thereby layer-by-layer growth.

6.2 Article II

In the second article, similar calculations are carried out for a Au adatom on Au(111) surface. Again, DFT and EMT were used to investigate the downstepping mechanisms. In this work we used kinked and stepped surfaces including large terraces in EMT calculations while smaller systems were used in the DFT calculations. Unlike the EMT calculations, we calculated only the last exchange descent mechanism in DFT/PBEsol calculations. Minimum energy paths for the descent of an adatom were calculated using the NEB method. DFT/PBEsol energy barriers for downstepping near kinks were found to be lower than at kinks or straight edges on B- edges and barriers were higher at the A-edge. This confirms the EMT results that downstepping near kinks on B type edges is the fastest process for interlayer transport. The activation energy for moving around a kink within the layer is significantly higher, so the downstepping near a kink promotes the formation of more kink sites. We therefore expect re-entrant layer-by-layer growth of Au(111) surface analogous to what has been found previously for Pt(111).

6.3 Article III

In the third article, we investigate the adsorption sites and diffusion processes of a Au adatom on the Si(100)-2×1 surface using DFT calculations with the PBEsol functional. We tested also two angular-dependent-potential (ADP) functions describing the Au-Si interaction, by performing and comparing the same set of calculations. Additionally, we used short time scale direct classical simulations to simulate the sequential deposition of Au atoms on Si(100)-2×1 surface. For each deposition event, starting from random lateral position, a nanosecond was simulated before another atom is deposited. The direct classical simulations are necessarily limited to short timescale and do not allow for diffusion and annealing events which would occur during experimental deposition where the time between deposition events is many orders of magnitude longer. Then, long timescale simulations were used for studies of annealing process for the Au overlayer. These longer timescale simulations made use of the adaptive kinetic Monte Carlo (AKMC) method. We found that direct classical dynamics simulations where each atom deposition is described over one nanosecond leads to irregular, amorphous structure while long time scale simulations (AKMC) annealing process leads to a more compact structure.

7 Conclusion and Future Direction

7.1 Conclusion

In the first part of this thesis, the mechanism by which an adatom that lands on top of a metal island can descend to a lower layer was identified. This is known to be a central issue determining whether the metal surface grows layer-by-layer or forms three dimensional islands. Density functional theory (DFT) within the PBEsol approximation, semi-empirical potential EMT, and Gaussian approximation Potential (GAP) approaches were used to investigate the downstepping mechanism of Pt adatom on Pt (111) surface and Au adatom on Au (111) surface, at both A- and B- type steps. The kinked and stepped surfaces (of large enough size to obtain convergence) of Pt and Au were used in the EMT calculations while smaller samples were used in the DFT/PBEsol calculations. Minimum energy paths (MEPs) for the decent of Pt and Au adatom were calculated using the NEB method. Qualitatively, similar trends were found in EMT calculations for both Pt and Au. The activation energy for moving around the kink within the layer were significantly higher. This shows that down stepping near kinks at B-type edges is the fastest process for layer-by-layer growth and it promotes the formation of more kink sites. The GAP potential calculations for both Pt/Pt (111) and Au/Au (111) systems were, however, inconsistent with the DFT/PBEsol results. The potential function is clearly not an accurate enough representation of the DFT/PBEsol energy landscape to be useful for these types of calculations. The GAP calculations indicated that energy barriers for down stepping for both Pt/Pt (111) and Au/Au (111) systems near kinks are lower than at kinks or straight edges. Also, the barriers are lower at B-type steps than at A-type step. A larger training set including more surface configurations would be needed to obtain a more accurate GAP potential.

In the second part of the thesis, the adsorption sites and diffusion processes of a Au adatom on a Si(100)-2$\times$1 surface were studied. Two angular-dependent potential (ADP18 and ADP20) functions optimised previously for the Si-Au interaction were used in addition to DFT calculations with the PBEsol functional. An interesting diffusion mechanism for a Au atom on the Si(100)-2$\times$1 surface was identified from the DFT/PBEsol calculations. The results were compared with two available empirical potential functions, ADP18 and ADP20, deveoped for describing the Si-Au interaction. Additionally, short timescale direct classical simulations based on the ADP18 potential function were used to simulate the sequential deposition of Au atoms on the Si(100)-2$\times$1 surface. These short timescale simulations are limited in that they do not include thermally activated diffusion and annealing processes, and lead to the formation of an amorphous structure. Longer timescale simulations based on the AKMC method were used to simulate annealing of the amorphous Au overlayer and the annealing was found to lead to a more compact structure. But, the Au-Si interaction is too strong in the ADP

potential functions, thereby favoring an extended Au overlayer rather than Au island formation.

7.2 Future Direction

The results obtained from the work on down-stepping of Au/Au (111) and Pt/Pt (111) using the NEB-DFT/PBEsol calculations ilustrate that a number of processes need to be taken into account to determine fate of an adatom that lands on top of an island, and thereby answer the question whether the atom deposition leads to 2D or 3D growth. Some of these features are subtle and unexpected, but they can control the surface morphology of a growing crystal. The challenge to theoretical studies is to identify the relevant processes and estimate the rate of these processes accurately enough to be able to explain the surface patterns observed in experimental measurements and to predict the growth mode of materials that have not been studied experimentally. The most serious challenge is the problem of identifying the relevant atomic scale processes. As the calculations presented here illustrate, the key process may be nonintuitive. This calls for efficient algorithms for finding which processes can occur in the system under study at given conditions. Since classical dynamics simulations cannot cover long enough time scales, advanced techniques are needed to search for likely transition mechanisms. Long time scale simulation methods such as adaptive kinetic Monte Carlo (Henkelman and Jónsson, 2001; Chill et al., 2014) have been used in combination with empirical potential functions in such studies, for example in simulations of Al(100) and Cu(100) growth (Henkelman and Jónsson, 2003), but the problem is that the more accurate and reliable DFT calculations have so far been computationally too demanding for such simulations. A possible future direction in this respect is the use of machine learning to interpolate between points in a training set of DFT calculations. The question still remains whether such an approach can be trusted to provide unexpected results since it represents only an interpolation between data fed into the machine learning algorithm. The most relevant part of the energy surface, corresponding to nonintuitive and unexpected mechanisms may be incorrectly represented since the training set will likely not contain such configurations. The challenge of explaining how microscopic processes influence macroscopic behavior is particularly relevant in studies of growth shapes of crystals, which offer a unique testing ground for the computational challenges of bridging vast length and time scales.

Article I

Mechanism of Low Temperature, Re-entrant 2D Growth of Pt(111)

Abid Ali, Vilhjálmur Ásgeirsson, Grace Siswanto Sun, Hannes Jónsson

Preprint submitted to Nanoscale

Mechanism of Low Temperature, Re-entrant 2D Growth of Pt(111)

Abid Ali[a], Vilhjálmur Ásgeirsson[a], Grace Siswanto Sun[b], Hannes Jónsson[a,b]

[a]*Science Institute and Faculty of Physical Sciences, University of Iceland VR-III,107 Reykjavík, Iceland*
[b]*Department of Chemistry, University of Washington, Seattle, WA, USA*

Abstract

Calculations of atomic scale transitions relevant to platinum crystal growth are presented to identify features in the energy landscape that can determine whether the growth mode is layer-by-layer, i.e. 2D, or whether new islands nucleate on top of existing islands resulting in 3D growth. The mechanism of the various transitions is found using the nudged elastic band method where the energy of the system and the atomic forces are evaluated using density functional theory within the generalized gradient approximation. The lowest energy paths for the descent of an adatom, i.e. interlayer transport, turns out to occur near but not at kink sites on both A- and B-type steps. This mechanism does not place an atom in the kink site but rather at the step edge showing that the often assumed scaling of activation energy with transition energy does not hold. The energy barrier for an adatom to round the corner and enter the kink site turns out to be significantly higher. This near kink descent mechanism therefore promotes the formation of a new row of step atoms and additional kink sites creating additional low paths for descent. The sites adjacent and above the step edge provide large binding energy for the adatom, especially at the B-step, and form a trough along which the adatom can migrate before descending, thereby increasing the probability of finding a kink site. The path to approach the step edge and reach such sites involves, however, a slight decrease in binding energy and corresponding increase in energy barriers, consistent with a depletion zone that has been reported from field ion microscopy experiments. These important features of the energy surface for the adatom are missing in the standard surface growth model but are qualitatively consistent with results obtained previously from calculations using a more approximate empirical potential function.

1. Introduction

When thin films are grown the goal is often to obtain 2D growth without raising the temperature of the sample so much that interlayer mixing occurs.

Email address: hj@hi.is (Hannes Jónsson)

Preprint submitted to Elsevier *January 11, 2022*

The key issue is whether atoms that land on top of an islands on the surface manage to descend down to the lower layer rather than form a new island on top of an existing island. An energy barrier larger than the activation energy for diffusion typically exists for such adatom descent and is referred to as the Ehrligh-Schwoebel (ES) barrier [1]. It arises from the fact that some bonds of the adatom to the underlying atoms need to be broken in the transition before new bonds can be formed with atoms in the lower layer. For example, if an atom sitting in a threefold site of an island on a (111) surface of an FCC crystal rolls over the island edge, one of the three bonds to the underlying atoms needs to be broken and a transition state traversed with only two bonds to the step atoms. Measurements using field ion microscopy (FIM) [2] and scanning tunneling microscopy (STM), as well as several theoretical calculations [4, 6, 7] for transition metal surfaces have shown, however, that such a descent process occur by a concerted displacement mechanism rather than by a hop over the step edge, but it, nevertheless, typically involves a significant energy barrier. The identification of the relevant transition mechanisms and characterization of the energy landscape for adatom migration on a growing surface is essential for gaining an understanding of the atomic scale mechanism of crystal and thin film growth and the conditions that will promote 2D growth [8].

Early theoretical studies of growth phenomena have been based mainly on kinetic Monte Carlo (KMC) simulations [9, 10, 11] where a table of possible transitions in the system is first created and some estimate made of the rate of the various possible events. Random numbers are then used to choose the sequence of events, consistent with the rate table, so as to simulate long time scale evolution of the system. Often the assumed rates of transitions are chosen in such a way as to reproduce some experimental observations. A more fundamental approach is to start from a description of the atomic interactions, thereby defining the energy of the system as a function of the atomic coordinates - an energy surface - and estimate the rate of the various transitions using rate theory [12]. Typically, the harmonic approximation to transition state theory [13, 14, 15] suffices to estimate rate of transitions involving atoms in and on the surface of solids at not too high temperature. Several studies using this approach have been carried out for the growth of transition metals using empirical potential energy functions such as the embedded atom method (EAM) [16, 17**?**] and the effective medium theory (EMT) [19] approach [6, 8]. The key challenge is to identify the relevant transition mechanisms. Usually this is assumed and postulated based on intuition, but a robust method for finding minimum energy paths for transitions, such as the nudged elastic band (NEB) method [20, 21], makes the exploration of a large number of possible mechanisms feasible, as long as the computational effort in evaluating the system energy and atomic forces is not too great. This has been done in calculations based on the EAM potential function and several unexpected mechanisms revealed, as discussed below [5, 4]. Nevertheless, the NEB method requires as input the final state of the transition and therefore is dependent on some predefined notion of the outcome of the transition. A more systematic method for exploring possible transition mechanisms where no assumption is made of the final state can also

be applied opening the possibility of discovering unexpected transition mechanisms [45, 23] and this approach has, for example, been used in simulations of Al(100) and Cu(100) growth using an EAM potential function [24].

From observations of the growth of several metals, in particular (100) facet of copper, it has been reported that 2D growth can be achieved at surprisingly low temperature [25, 26]. When higher temperature leads to three-dimensional growth this phenomenon is referred to as re-entrant 2D growth [27]. The experimental characterization is most thorough for Pt(111) and involves both low energy He atom scattering [27, 28, 29] and scanning tunneling microscopy (STM) [30] measurements.

Motivated by the observation of surprising re-entrant 2D growth of Pt(111), there have been several theoretical calculations devoted to the study of adatom descent at step edges, *i.e.* interlayer transport. It has been found that many subtle features of the energy landscape can affect the probability of descent. FIM experiments have shown an excluded zone near island edges both on Ir(111) and Pt(111) surfaces [31, 32, 33, 34]. Estimates based on calculations using the EAM interaction potential have indicated that as an adatom approaches a step edge from above, a gradual rise in the energy occurs (decrease in the binding energy) as far as three sites away from the edge [4]. This is likely due to elastic strain caused by the step. This is a subtle effect, but even a rise of only 0.03 eV will significantly reduce the adatom population at room temperature of sites near the edge. As the adatom enters, however, sites adjacent to the step edge, the energy is reduced considerably. This again is consistent with the FIM measurements and can be rationalized from bond counting arguments and the general principle that less coordinated atoms form stronger bonds. The edge atoms are 7-fold coordinated as compared to the 9-fold coordination of terrace atoms. The adatom can, therefore, be expected to populate lower energy sites adjacent to the step edge. The energy barrier for adatom hops between such sites along the step edge has been estimated in EAM calculations [4] to be significantly smaller than either diffusion away from the step edge or descent to the lower layer. As a result, the adatom can be expected to diffuse along the edge once it has reached the step edge. This increases the attempt frequency for descent but can also increase the probability of nucleation of a new island on top of an existing island.

This illustrates that one has to be careful when defining the effective energy barrier for descent, i.e. interlayer transport. The important issue is the relative probability of descent vs. reflection back into the interior of the island. It is not enough to just focus on the energy barrier for the descent from a site adjacent to the step edge. In calculations of the energy of the adatom at various binding sites and the energy barriers for transitions it is essential to use a *common zero of energy*, which is naturally taken to be the energy of the most favorable, FCC binding site on the flat terrace representing the interior of a large island. Often the ES barrier is estimated simply as the difference between the energy barrier for descent starting from a site adjacent to the step edge minus the activation energy for diffusion on the flat terrace. The FIM measurements show that the landscape is more complex than is assumed in such calculations and this has

also been inferred from the EAM calculations.

Electronic structure calculations have been carried out using the density functional theory (DFT) approach within the local density approximation (LDA) to estimate energy barriers for descent from a site adjacent to a step edge [7]. The energy barrier for hopping along the edge was again found to be significantly lower (by over 0.1 eV) than either the barrier for descent or the barrier for a hop to the second site from the edge. These DFT/LDA results therefore support the notion that an adatom which has reached the step edge is most likely going to migrate along the perimeter of the island before descent. A key question that remains to be addressed by DFT calculations is what the relative energy of the binding sites adjacent to the step edge is compared with the FCC site of the flat terrace.

As an adatom migrates along the step edge it is likely to run into defects such as kinks where a row of atoms ends. The importance of kinks as well as corners of island edges (where A- and B-steps meet) on the energy barrier for descent has been pointed out based on extensive exploratory NEB calculations using the EAM potential [4]. It was shown that kink sites can offer significantly lower energy paths for descent as compared to straight edges. An unexpected mechanism involving an edge atom near, but not at, a kink site on the B-type step turned out to have a particularly low energy barrier. Preliminary DFT/GGA calculations using the PW91 functional have also shown that this qualitative feature predicted by the EAM calculations [8, 35]. If confirmed by more exhaustive calculations, this can provide an explanation of the re-entrant 2D growth, i.e. the transition from 3D growth to 2D growth as the temperature is lowered. STM measurements of adsorbed Co atom on Pt(111) islands has indeed shown that kinks offer the lowest path for descent and the mechanism was found to be the non-intuitive one derived from the EAM calculations [3].

From simulations of Pt(111) growth using KMC and a rather simple transition table it has been concluded that no reasonable set of energy barriers and pre-exponential factors in the rates of the various transitions can reproduce the re-entrant 2D growth unless the low energy near kink descent process is included [6]. The simulations were tailored to CO contaminated STM experiments where triangular islands with A-edges form in the intermediate, 3D growth regime. More recently, simulations of island shapes have been carried out using energetics calculated for clean as well as CO contaminated Pt(111) surface with focus on island shapes [36].

While a great deal of effort has gone into studies of the energetics that affect island shapes and interlayer transport on Pt(111) there is still need for higher level electronic structure calculations using a more accurate functional than the LDA and using a common zero of the energy for the adatom binding at various sites and the height of saddle points on the energy surface to determine activation energy. The question is whether the complex features identified by the simpler and more approximate empirical potentials are reproduced in these more accurate but also computationally much more demanding calculations. In particular, it remains to be seen whether the special role of kinks and corners in the interlayer transport is present in the energy landscape predicted by the

Figure 1: Ilustration of the simulation cell used for the DFT calculations of the straight B-type step. The Miller index is (221). The lowest atom layers (darker gray) are fixed at positions corresponding to the three-dimensional crystal.

electronic structure calculations. While preliminary results have indicated this to be the case [8], the purpose of the present study is to address this issue in a systematic way.

The article is organized in the following way. The methodology is described in section 2 , including the systems simulated, the electronic structure method, the method for finding minimum energy paths of transitions and long time scale simulation. Then the results are presented in section 3. The article concludes with a discussion in section 4.

2. Methods

A flat Pt(111) terrace is simulated using a slab with 5 layers, each containing 16 atoms, the atoms in the bottom two layers being kept fixed. This system is used to calculate the zero of energy for the adatom in all subsequent calculations presented here, namely the binding energy of at an FCC site. Also, the activation energy for diffusion, i.e. hop from an FCC site to an HCP site is evaluated. This quantity can be compared with the experimentally determined activation energy for diffusion.

The straight A-type step, which has a {100} microfacet, is represented by a slab with a surface Miller index (322) while a kink on the step is represented by a slab with a surface Miller index (956). The straight B-type step, which has a {111} microfacet, is represented by a slab with a surface Miller index (221) while a kink on the step is represented by a slab with a surface Miller index (985). These configurations contain between 150 and 200 atoms, large and demanding systems for electronic structure calculations. A cross section of the system used to study a periodic B-type step is shown in figure 1.

The electronic structure calculations are carried out using the density functional approach [37] within the generalized gradient approximation that is a step up in accuracy from LDA [38]. Most of the calculations are carried out with with the PBEsol functional [39] as it gives good estimate of surface energy, a quantity that affects the strength of adatom interaction with the surface, as

well as the lattice parameter (3.91 Å vs. the experimental value of 3.92 Å). The PW91 functional [40, 41] is also used for some of the calculations. The valence electrons are described with plane waves while the effect of inner electrons is described using the projected augmented wave (PAW) formalism [42]. An energy cutoff of 400 eV is used in the plane wave expansion. A 2x2x1 k-point sampling is used with Methfessel-Paxton smearing [43] at a temperature of 0.1 eV. The reported energy values are for extrapolation to zero temperature. The VASP implementation was used in the calculations [44].

The minimum energy paths for the various transitions are calculated using the nudged elastic band method [20, 21] with the climbing image extension [**?**] and improved tangent estimate [46]. The tolerance in the magnitude of atomic forces in optimizations of the atomic coordinates both for identification of local minima and the minimum energy paths is 0.02 eV/Å. Typically, 5 intermediate images are used to represent the path in between the fixed endpoints, but this is specified further in the graphs below showing the calculated results. The initial path is generated using the image dependent pair potential [47].

Given the estimates of binding energy and activation energy for the various transitions, a model is constructed for kinetic Monte Carlo (KMC) simulations of the time evolution of an adatom on top of a surface island. The KMC implementation includes both FCC and HCP sites for the adatom as has been described previously [8]. The model takes into account the slight, 0.02 to 0.03 eV increase in binding energy and corresponding energy barriers as an adatom approaches a step edge, as well as the 0.2 to 0.3 eV increase in binding energy at sites adjacent to the step edge, the barrier for diffusing along the step and barrier for descent at straight steps and kinks.

3. Results

The results obtained from the DFT calculations combined with the NEB method for finding minimum energy paths are presented first for descent at step edges, both straight and with a kink. Then, the paths for moving around a corner site at a kink is presented and finally the energy landscape for approaching a step edge from above. Finally, KMC simulations of adatom diffusion on top of an island at room temperature and subsequent descent are presented.

Figure 2 shows the results obtained for Pt adatom diffusion on the flat terrace. The adatom starts at an FCC site and hops over a bridge to an HCP site. The binding energy difference is 0.2 eV. The energy barrier is found to be 0.29 eV, which is in close agreement with estimates from previous DFT calculations [54]. The completion of a diffusion path is a second hop from the HCP site to another FCC site. The overall activation energy for diffusion is, therefore, estimated to be 0.29 eV. This is in reasonable agreement with estimates from experimental measurements, both FIM and STM which which give a value of 0.26 eV [48, 49, 50].

The adatom energy at the FCC site on the flat terrace is taken to be the zero of energy in all the results presented below. It is important to have a single well defined zero of energy when such a complex energy landscape is explored rather

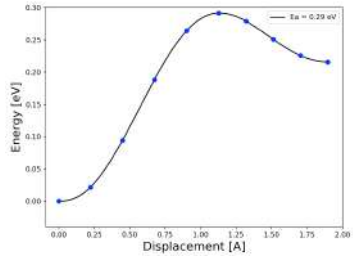

Figure 2: Calculated energy along the minimum energy path for adatom hop from an FCC site to an HCP site on flat Pt(111) surface. The complete diffusion path involves analogous hop in reverse from the HCP site to another FCC site. The activation energy for diffusion is found to be 0.29 eV and the energy difference between the two sites is 0.2 eV. The energy of the adatom at the FCC site on the flat terrace is taken to be the zero of energy in all the results presented here.

than shift the zero of energy to whatever happens to be the initial configuration of the various transitions studied.

3.1. Adatom descent

Figures 3 and 4 show calculated minimum energy paths for the descent of an adatom at A- and B-type steps with and without kinks. The initial site of the adatom is adjacent to the step edge, an HCP site in the case of the A-type step but an FCC site in the case of the B-type step. The zero of energy is the energy corresponds to an adatom at an FCC site on the flat (111) surface. The energy barriers for descent are summarized in table 1.

As had been seen from EAM calculations [4], the lowest energy barrier is obtained for a surprising mechanism, a descent near a kink but not into a kink site. This is in contradiction with a frequently invoked approximation where energy barriers are assumed to scale with the energy of the transition, i.e. barriers being lower when the final state energy is lower. In this case, the lowest barrier is for a mechanism where an atom is sitting at a step edge rather than in the kink site, a final state that is ca. 0.5 eV higher in energy (see insets in figures 3 and 4 showing the transition mechanism). The lowest barrier is for the descent near a kink site on the B-type step, 0.30 eV. The highest barrier is for a straight A-type step, 0.44 eV.

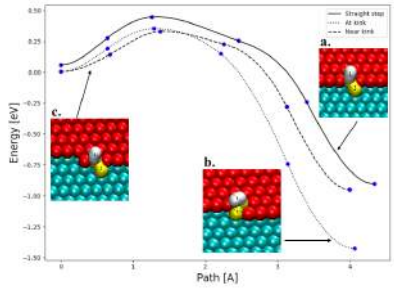

Figure 3: Calculated energy along minimum energy paths for the descent of an adatom at an A-type step, with or without a kink. Insets show the images of the atoms in a converged nudged elastic band calculation of the transition path and points on the energy curve show energy of the intermediate system images in the NEB calculations. Remarkably, the lowest activation energy is obtained for descent near but not at a kink site even thought this mechanism leads to significantly higher final state energy (see Table 1 for numerical values).

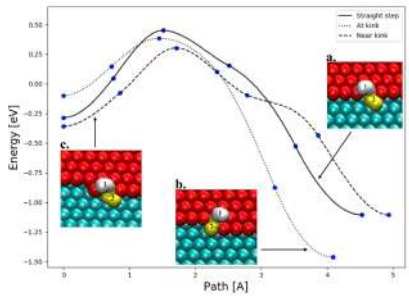

Figure 4: Calculated energy along minimum energy paths for the descent of an adatom at a B-type step, with and without a kink. Insets show the images of the atoms in a converged nudged elastic band calculation of the transition path and points on the energy curve show energy of the intermediate system images in the NEB calculations. Remarkably, the lowest activation energy is obtained for descent near but not at a kink site even thought this mechanism leads to significantly higher final state energy (see Table 1 for numerical values).

Table 1: Results of DFT/PBEsol calculations of the activation energy for adatom descent at A- and B-type steps, with and without kink sites. The activation energy is the saddle point energy minus the energy of the adatom at an FCC site of an extended (111) surface.

Step type	Mechanism	Activation energy
A		
	straight	0.44
	at kink	0.35
	near kink	0.33
B		
	straight	0.45
	at kink	0.38
	near kink	0.30

3.2. Rounding a corner

The preference for the near kink mechanism is important because it places an atom on the side of an existing step, thereby providing a seed for the formation of a new step and additional kink sites. A key issue then is whether such an atom can easily move from this rather high energy site to the kink site by rounding the corner atom. The minimum energy paths for such transitions on both the A-type and B-type steps are shown in figure 5. The mechanism is shown in insets. The calculated energy barrier is large for both steps, around 0.9 eV. This means that the atom placed adjacent to a step edge after descent near a kink is likely going to diffuse only along that step edge and will eventually bind to another such atom to nucleate a new step edge, thereby introducing two more kink sites. The low energy descent paths with, therefore, proliferate. Another mechanism for the atom to move into the kink site, involving concerted exchange, was also calculated but turned out to have even higher energy.

3.3. Step approached from above

The calculations of paths for adatom descent at step edges described above started at the binding site adjacent to the step edge, an HCP site on the A-type step and an FCC site on the B-type step. The energy of this initial site at the A-type step is slightly positive, meaning that the binding energy of the adatom is lower there than on the flat terrace. It is, however not as high as at an HCP site on the flat terrace because it is bound to one under coordinated step atom. The energy of the initial site at the B-type step is, however, significantly lower than for the flat terrace. This is an FCC site which is lowered further in

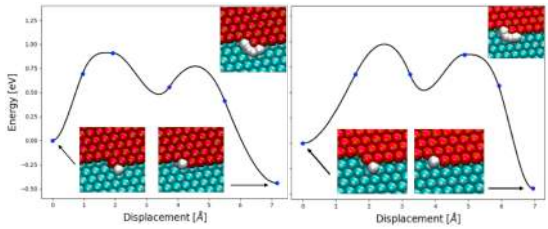

Figure 5: Calculated energy along minimum energy paths for the adatom to move from outside a step edge into a kink site on A-type step (left) and B-type step (right). Insets show the images of the atoms in a converged nudged elastic band calculation of the transition path. The energy barriers are high, much too high for the process to be active at room temperature, thus leading to growth of rough edges of islands.

energy by the fact that the adatom binds to two under coordinated step atoms. The adatom is, therefore, trapped near the descending B-type step edge. The question then becomes to what extent an adatom located at such a strongly binding site can migrate and in what direction.

The minimum energy paths for the adatom displacement away from the step edge and along the step edge are illustrated in figure 6. From this it becomes evident that the atom will migrate primarily along the step edge. A trench is formed long the step in which the atoms moves in a diffusive way back and forth. The energy barrier to move out of this trench away from the step and towards an interior of an island is just about as high as the energy barrier to descend.

The figure also illustrates how the binding energy of the adatom gradually decreases as the adatom approaches the step. While this amounts to just 0.02 to 0.03 eV, it will significantly reduce the probability of finding an adatom at these sites at room temperature. This slight increase in energy is then the main obstacle for an adatom to approach a step edge and subsequently descend to the lower layer, not the barrier to descend from the site adjacent to the step. The energy landscape emerging from these DFT calculations is, therefore, quite different from what is generally assumed, as illustrated in figure 6. Instead of a equal binding energy for all sites on the upper terrace and then an increased barrier only for descent to the lower layer, there is a gradual rise in energy as the atom approaches the step edge and then a trough with large binding energy at sites next to the step edge. The energy barrier to descend from there is not higher than the barrier to go back to the interior of the island, especially when the presence of kinks are taken into account.

3.4. kinetic Monte Carlo simulation

In order to explore the consequences of the main features of the energy landscape emerging from the DFT calculations on the dynamics of an adatom

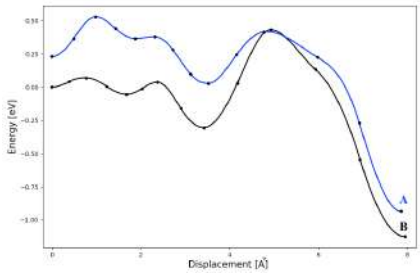

Figure 6: Calculated energy along minimum energy paths for the approach of an adatom to a step edge and descent to the lower layer (using PW91 functional). The energy barrier for migration along the step edge is indicated with dashed lines. The adatom binds most strongly at sites adjacent to the step edge and diffusion along the step is more facile than either descent or migration away from the step. As a result, the adatom mainly travels along the step once it has reached the step edge.

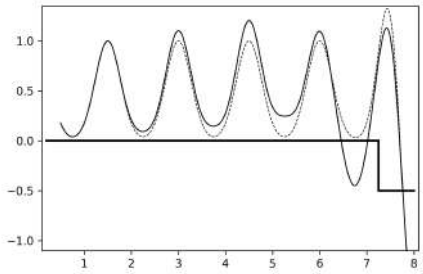

Figure 7: A schematic illustration of the energy landscape emerging from the DFT calculations (solid line) were the energy at binding sites rises when the adatom approaches the step edge (by 0.02 to 0.03 eV) but then gets trapped at sites adjacent to the step edge (by 0.1 to 0.3 eV). Diffusion along the step edge is then most facile while the energy barrier for migration away from the step edge and the barrier for descent are significantly higher and roughly equal. The 'standard' and frequently assumed energy landscape is shown for reference (dashed line) where each binding site is assumed to be equivalent and providing the same binding energy.

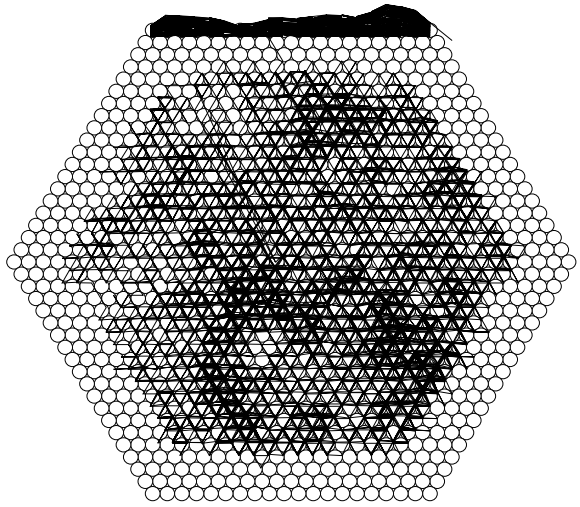

Figure 8: Diffusion path of an adatom on top of an island at a temperature of 300 K generated using a kinetic Monte Carlo simulation based on the energy landscape illustrated in figure 7. The adatom starts in the interior of the island and visits the various binding sites except for those close to the step edge. This corresponds closely to the visitation map of sites obtained experimentally by field ion microscopy [34]. Once the adatom reaches a site adjacent to the step edge, it only moves along the step (see thick bundle of paths at the uppermost island edge) until it descends near a corner site (to the right).

that lands on top of a hexagonal island on the Pt(111) surface, a kinetic Monte Carlo simulation for room temperature is carried out. The results are shown in figure 7. The adatom explores repeatedly most of the sites in the interior of the island but sites near the edge of the island are rarely visited and when they are, the adatom is most often reflected back to the interior. Eventually, the adatom makes it to a B-type edge and is then trapped for a long time, migrating back and forth along the edge, until it eventually descends near a corner site (where there is a low barrier descent path analogous to that near a kink). This is illustrates how the slight decrease in binding energy and corresponding increase in barrier height (with respect to the FCC site on a flat terrace) is the effective barrier for descent, not the activation energy for the descent process itself starting from a site adjacent to the step edge.

4. Discussion

The preference for descent near kinks over descent at straight step edges and at kinks found here from the NEB calculations combined with DFT is qualitatively consistent with the original suggestion of this mechanism which was obtained from extensive studies of various mechanisms using the EAM potential function [4]. Wide exploration of mechanisms beyond what is assumed to be optimal *a priori* as was carried out there is clearly of great importance as the energy surface is highly complex. This descent near kink sites has strong influence on the surface morphology of the growing surface since the energy barrier for rounding the corner into a kink site is too high for the process to be active at, for example, room temperature. The energy barrier is more than three times larger than the energy barrier for descent. This means that an atom that has undergone such a descent process becomes the nucleus of a new row of atoms, i.e. a new step, and thereby new kink sites that offer additional low energy paths for descent. If the low energy pathway were to simply fill the kink site, then the number of kink sites would remain low and the effect be less pronounced. The importance of the descent near kinks rather than at kinks has been further emphasized in KMC simulations [6] where it was shown that re-entrant 2D growth could not be obtained without this preference for descent near kink sites. The simulations were, however, based on a highly simplified table of transitions and did not include nearly all the subtleties in the DFT energy landscape.

The calculations also support another feature that was identified in the EAM simulations, namely the slight decrease in binding energy and increase in energy barriers as an adatom approaches a step edge from above, but before entering one of the sites adjacent to the edge. This in the end becomes the feature of the energy landscape that most promotes 3D growth because it prevents the adatom from coming hear the step edge. This feature is not taken into account in standard models of the energy landscape, as illustrated in figure 8 (dashed line). FIM measurements have shown clearly such an avoided zone for the adatom next to the step edge, so the calculations are in good correspondence with experiment. Either the definition of the Ehrlich-Schwoebel barrier needs to be refined to take into account not only the descent from a site adjacent to the step edge but also this more delocalized drift in the energy which may be more important in some cases, as seems to be the case for Pt(111). This upward drift in energy is likely the results from elastic strain effects. Possibly, a new quantity should be defined that better reflects what the critical feature is in an energy landscape for distinguishing between 2D and 3D growth at low temperature. The strong binding to the sites adjacent to the step edge is another feature that is missing in the standard models, but is found here in the DFT results, especially at the B-type edge. This feature was, again, predicted from the EAM calculations and there a classical dynamics simulation showed how the adatom runs back and forth along the step until it finally descents near a kink or corner site [4].

The descent of an adatom near but not at a kink site could explain the

ocurrence of re-entrant 2D growth. The transition from 3D to 2D growth as temperature is lowered seems to coincide with a transition from compact islands with relatively straight edges to dendritic islands with high density of kinks, as judged from scanning tunneling microscopy measurements [30]. Straight edges lead to large activation energy for descent while the presence of kinks offers low energy paths for descent that can be active even at low temperature. Thus, even though the thermal energy of the adatoms is reduced, the number of low barrier paths for descent is increased enough by the increase in kink density that 2D growth reappears as the temperature is lowered. Another important consideration is the slight but significant decrease in binding energy and corresponding increase in activation energy as an adatom on top of an island approaches a step edge. For a large island, this will hinder the adatom from reaching the step edge and thereby promote 3D growth. For islands that are small enough, such as dendritic islands with width less than 6 atom rows, this upward drift in the adatom energy will be smaller. It remains to be seen from detailed KMC simulations that properly take into account all these subtle features which of these two effects or even both are responsible for the re-entrant 2D growth. In any case, these explanation that emerge from the calculations are consistent with the original explanation of Kunkel et al. [27] that 'the reduced island size and/or their less regular shape, both due to the reduced adatom mobility at lower temperature' leads to the re-entrant 2D growth.

The results of the NEB calculations combined with DFT presented above illustrate that there are a number of important processes relevant to the fate of an adatom that lands on top of an island, and thereby the question whether the vapor deposition leads to 2D or 3D growth. Some of these features are subtle and unexpected, but they can control the surface morphology of a growing crystal. The challenge to the theoretical studies is to identify the relevant processes and estimate the rate of these processes accurately enough to be able to explain the surface patterns observed in experimental measurements and it seems clear that the standard model is oversimplified. The most serious challenge to theoretical studies is the problem of identifying the relevant processes. As the calculations on Pt(111) presented here illustrate, the key process may be non-intuitive, as the near but not at kink sites, shown in figures 3 and 4. This calls for algorithms that can find what processes would occur in the simulated system if direct classical dynamics simulations could be carried out long enough to cover experimental time scales. Long time scale simulation approaches such as the adaptive kinetic Monte Carlo method [45, 23] can in principle be used in such studied, as has been illustrated for Al(100) and Cu(100) growth, but the problem is that the DFT calculations are computationally very demanding, too much so to make such calculations practical at the present time, and that empirical potential functions such as EAM and EMT are too approximate, although they have been used successfully to identify unexpected mechanisms. A possible future direction in this respect is the use of machine learning to interpolate between calculated DFT results. The question still remains whether such an approach can be trusted to provide unexpected results since it represents only an interpolation between results fed into the machine learning as a test set. The

challenge of explaining how microscopic processes influence macroscopic behavior is particularly relevant in studies of growth shapes of crystals, which offer a unique testing ground for the computational challenges of bridging vast length and time scales.

5. Acknowledgement

This work was funded by the European Union's Horizon 2020 research and innovation programme under the Marie Sklodowska Curie Innovative Training Network ELENA, grant agreement No. 722149.

[1] R. L. Schwoebel and E. J. Shipsey, 'Step motion on crystal surfaces', *J. Appl. Phys.* **37**, 3682 (1966); G. Ehrlich and F. G. Hudda, 'Atomic view of surface self-diffusion: Tungsten on tungsten', *J. Chem. Phys.* **44**, 1039 (1966).

[2] S. C. Wang and G. Ehrlich, 'Atom incorporation at surface clusters: An atomic view', *Phys. Rev. Lett.* **67**, 2509 (1991).

[3] E. Lundgren, B. Stanka, G. Leonardelli, M. Schmid and P. Varga, 'Interlayer Diffusion of Adatoms: A Scanning-Tunneling Microscopy Study', *Phys. Rev. Lett.* **82**, 5068 (1999).

[4] M. Villarba and H. Jónsson, 'Diffusion Mechanisms Relevant to Metal Crystal Growth: Pt/Pt(111) ', *Surf. Sci.*, **317**, 15 (1994).

[5] M. Villarba and H. Jónsson, 'Low Temperature Homoepitaxial Growth of Pt(111) in Simulated Vapor Deposition', *Phys. Rev. B* , **49**, 2208 (1994).

[6] J. Jacobsen, K. W. Jacobsen, P. Stoltze, and J. K. Nørskov, 'Island shape-induced transition from 2D to 3D growth for Pt/Pt(111)', *Phys. Rev. Lett.* **74**, 2295 (1995).

[7] P. J. Feibelman, 'Interlayer Self-diffusion on Stepped Pt(111)', *Phys. Rev. Lett.* **81**, 168 (1998).

[8] H. Jónsson, 'Theoretical Studies of Atomic Scale Processes Relevant to Crystal Growth', *Annual Review of Physical Chemistry*, **51**, 623 (2000).

[9] D. T. Gillespie, 'A general method for numerically simulating the stochastic time evolution of coupled chemical reactions', *J. Comp. Phys.*, **22**, 403 (1976).

[10] D. T. Gillespie, 'Monte Carlo simulation of random walks with residence time dependent transition probability rates', *J. Comp. Phys.*, **28**, 395 (1978).

[11] G. H. Gilmer, 'Computer models of crystal growth', *Science* **208**, 355 (1980).

[12] A. F. Voter, 'Introduction to the Kinetic Monte Carlo Method', in *Radiation Effects in Solids*, edited by K. E. Sickafus and E. A. Kotomin (Springer, NATO Publishing Unit, Dordrecht, The Netherlands, 2005).

[13] E. Wigner, 'Uber das Uberschreiten von Potentialschwellen bei chemischen Reaktionen', *Z. Phys. Chem. Abt. B* 19, 203 (1932).

[14] C. Wert and C. Zener, 'Interstitial Atomic Diffusion Coefficients', *Phys. Rev.*, **76**, 1169 (1949).

[15] G. H. Vineyard, 'Frequency factors and isotope effects in solid state rate processes', *J. Phys. Chem. Solids* **3**, 121 (1957).

[16] M. S. Daw and M. I. Baskes, 'Embedded-atom method: Derivation and application to impurities, surfaces, and other defects in metals', *Phys Rev. B* **29**, 6443 (1984).

[17] A. F. Voter and S. P. Chen, *Mat. Res. Soc. Symp. Proc.* **82** (1987) 175.

[18] M.S. Daw, 'Model of metallic cohesion: The embedded-atom method', *Phys. Rev. B* **39**, 7441 (1989).

[19] K. W. Jacobsen, J. K. Nørskov, and M. J. Puska, 'Interatomic interactions in the effective-medium theory', *Phys. Rev. B* **35**, 7423 (1987).

[20] G. Mills, H. Jónsson and G. K. Schenter, 'Reversible work transition state theory: application to dissociative adsorption of hydrogen', *Surf. Sci.* **324**, 305 (1995).

[21] H. Jónsson, G. Mills, and K. W. Jacobsen, in *Classical and Quantum Dynamics in Condensed Phase Simulations*, ed. B. J. Berne, G. Ciccotti, and D. F. Coker, page 385 (World Scientific, 1998).

[22] G. Henkelman and H. Jónsson, 'Long time scale kinetic Monte Carlo simulations without lattice approximation and predefined event table', *J. Chem. Phys.* **115**, 9657 (2001).

[23] S.T. Chill, M. Welborn, R. Terrell, L. Zhang, J-C. Berthet, A. Pedersen, H. Jónsson and G. Henkelman, 'EON: Software for long time simulations of atomic scale systems', *Modelling and Simulation in Materials Science and Engineering* **22**, 055002 (2014).

[24] G. Henkelman and H. Jónsson, 'Multiple time scale simulations of metal crystal growth reveal importance of multi-atom surface processes', *Phys. Rev. Letters*, **90**, 116101 (2003).

[25] J. J. de Miguel, A. Sanchez, A. Cebollada, J. M. Callego, J. Ferron, and S. Ferrer, *Surf. Sci.* **189/190**, 1062 (1987).

[26] W.F. Egelhoff and I. Jacob, 'Reflection High-Energy Electron Diffraction (RHEED) Oscillations at 77 K', *Phys. Rev. Letters* , **62**, 921 (1989).

[27] R. Kunkel, B. Poelsema, L. K. Verheij, and G. Comsa, 'Reentrant layer-by-layer growth during molecular-beam epitaxy of metal-on-metal substrates', *Phys. Rev. Letters* **65**, 733 (1990).

[28] B. Poelsema, R. Kunkel, N. Nagel, A. F. Becker, G. Rosenfeld, L. K. Verheij, and G. Comsa, 'New phenomena in homoepitaxial growth of metals'; *Appl. Phys.* **A 53**, 369 (1991).

[29] B. Poelsema, A. Becker, G. Rosenfeld, R. Kunkel, N. Nagel, L. K. Verheij, and G. Comsa, 'On the shape of the in-phase TEAS oscillations during epitaxial growth of Pt(111) *Surf. Sci.* **272**, 269 (1992).

[30] M. Kalf, G. Comsa, and T. Michely, 'How sensitive is epitaxial growth to adsorbates', *Phys. Rev. Lett.* **81**, 1255 (1998).

[31] S. C. Wang and G. Ehrlich, 'Adatom motion to lattice steps: A direct view', *Phys. Rev. Lett.* **70**, 41 (1993).

[32] S. C. Wang and G. Ehrlich, 'Atom condensation at lattice steps and clusters', *Phys. Rev. Lett.* **71**, 4174 (1993).

[33] A. Gölzhäser and G. Ehrlich, 'Atom movement and binding on surface clusters: Pt on Pt(111) clusters', *Phys. Rev. Lett.* **77**, 1334 (1996).

[34] K. Kyuno and G. Ehrlich, 'Step-edge barriers: An atomistic view', *Phys. Rev. Lett.* **81**, 5592 (1998).

[35] G. Siswanto Sun, *PhD thesis*, University of Washington (2000).

[36] J. Wu, E. G. Wang, K. Varga, B. G. Liu, S. T. Pantelides and Z. Zhang, 'Island shape selection in Pt(111) submonolayer homoepitaxy with or without CO as an adsorbate', *Phys. Rev. Lett.* **89**, 146103 (2002).

[37] P. Hohenberg and W. Kohn, *Phys. Rev.*, **136**, B864 (1964); W. Kohn and L. J. Sham, *Phys. Rev.*, **140**, A1133 (1965).

[38] J. P. Perdew, 'Jacob's ladder of density functional approximations for the exchange-correlation energy', *AIP Conference Proceedings*, **577**, 1 (2001).

[39] J. P. Perdew, J. P. Perdew, A. Ruzsinszky, G. I. Csonka, O. A. Vydrov, G. E. Scuseria, L. A. Constantin, X. Zhou and K. Burke, 'Restoring the density-gradient expansion for exchange in solids and surfaces', *Phys. Rev. Lett.* **100**, 136406 (2008); *Phys. Rev. Lett.* **102**, 039902 (2009).

[40] J. P. Perdew, in *Electronic Structure of Solids*, eds. P. Ziesche and H. Eschrig (1991).

[41] J. P. Perdew and Y. Wang, 'Accurate and simple analytic representation of the electron-gas correlation energy', *Phys. Rev. B* **45**, 13244 (1992).

[42] P. E. Bloechl, 'Projector augmented-wave method', *Phys. Rev. B* **50**, 17953 (1994).

[43] M. Methfessel and A.T. Paxton, 'High-precision sampling for Brillouin-zone integration in metals', *Phys. Rev. B* **40**, 3616 (1989).

[44] G. Kresse and J. Hafner, *Phys. Rev. B* **47**, 558 (1993); **49**, 14251 (1994); G. Kresse and J. Furthmüller, *Comput. Mater. Sci.* **6**, 16 (1996); *Phys. Rev. B* **55**, 11169 (1996).

[45] G. Henkelman, B. Uberuaga and H. Jónsson, 'A Climbing-Image NEB Method for Finding Saddle Points and Minimum Energy Paths' *J. Chem. Phys.* **113**, 9901 (2000).

[46] G. Henkelman and H. Jónsson, 'Improved Tangent Estimate in the NEB Method for Finding Minimum Energy Paths and Saddle Points', *J. Chem. Phys.* **113**, 9978 (2000).

[47] S. Smidstrup, A. Pedersen, K. Stokbro and H. Jónsson, 'Improved initial guess for minimum energy path calculations', *J. Chem. Phys.* **140**, 214106 (2014).

[48] P. J. Feibelman, J. S. Nelson, and G. L. Kellogg, *Phys. Rev. B* **49**, 10548 (1994).

[49] K. Kyuno, A. Gölzhäuser, and G. Ehrlich, *Surf. Sci.* **397**, 191 (1998).

[50] M. Bott, M. Hohage, M. Morgenstern, T. Michely, and G. Comsa, *Phys. Rev. Lett.* **76**, 1304 (1996).

[51] H. Brune, *Surf. Sci. Reports* **31**, 121 (1998).

[52] D. Vanderbilt, *Phys. Rev. B* **41**, 7892 (1990).

[53] S. Liu and H. Metiu, *Surf. Sci.* **359**, 245 (1996).

[54] P. J. Feibelman, 'Self-Diffusion Along Step Bottoms on Pt(111)', *Phys. Rev. B* **60**, 4972 (1999).

[55] K. Kyuno and G. Ehrlich, 'Step-edge barriers: truths and kinetic consequences', *Surf. Sci.* **383**, L766 (1997).

[56] G.L. Kellogg, *Surf. Sci. Reports* **21**, 1 (1994).

[57] G. Henkelman and H. Jónsson, 'A dimer method for finding saddle points on high dimensional potential surfaces using only first derivatives' *J. Chem. Phys.* **111**, 7010 (1999).

Article II

Mechanism of Interlayer Transport on a Growing Au(111) Surface: 2D vs. 3D Growth

Abid Ali, Hannes Jónsson

Surfaces and Interfaces, 31(2022), 101944

Surfaces and Interfaces 31 (2022) 101944

Contents lists available at ScienceDirect

Surfaces and Interfaces

journal homepage: www.sciencedirect.com/journal/surfaces-and-interfaces

Mechanism of Interlayer Transport on a Growing Au(111) Surface: 2D vs. 3D Growth

Abid Ali [a], Hannes Jónsson [a,b,*]

[a] Science Institute and Faculty of Physical Sciences, University of Iceland, VR-III, Reykjavík 107, Iceland
[b] Dept. of Chemistry, Brown University, Rhode Island 02912, USA

ARTICLE INFO

Keywords:
Interlayer transport
Crystal growth
Simulations
Transition mechanism
Electronic structure
Gold

ABSTRACT

The atomic scale transitions corresponding to diffusion and interlayer transport of a Au adatom on the low energy, close packed Au(111) surface are studied using density functional theory calculations within the generalized gradient approximation. Minimum energy paths and estimates of activation energy are calculated for processes that influence whether the crystal grows layer-by-layer, i.e. 2D growth, or whether new islands tend to nucleate on top of existing islands resulting in 3D growth. Kinks on island edges turn out to provide paths for adatom descent with lower activation energy than straight steps. The energy barrier for an adatom to round the corner and enter a kink site is significantly higher. A descent mechanism that places an adatom near but not at a kink site can therefore promote the formation of a new row of step atoms and lead to the introduction of additional kink sites, thereby opening up new low activation energy paths for descent and promotion of 2D growth. The sites adjacent and above the step edge provide large binding energy for the adatom, especially at the B-type step, and form a trough along which the adatom can migrate before descending, thereby increasing the probability that an adatom finds a kink on the B-type step. These features of the energy landscape representing the interaction of a Au adatom with the surface point to the possibility of a re-entrant layer-by-layer growth mode of the low energy, close packed surface of the gold crystal.

1. Introduction

In some material growth applications the goal is to form nanoscale islands on a surface while in others the preferred growth mode is layer-by-layer. The morphology of the surface is typically governed by kinetic processes rather than thermodynamics because the surface temperature is kept low enough to prevent the mixing of components. An important consideration then is the rate of various atomic rearrangement processes, in particular those that lead to descent of adatoms from an upper layer to a lower layer, i.e. interlayer transport. Such processes have been studied extensively for several metals, in particular platinum, but while gold is also an attractive metal in various applications, little work has been done so far on interlayer transport in gold crystal growth.

An energy barrier larger than the activation energy for diffusion on a flat surface typically exists for the descent of an adatom from an upper layer to a lower layer and it is referred to as the Ehrlich-Schwoebel (ES) barrier [1]. This can be most easily seen if an adatom sitting in a threefold site of an island on a (111) surface of an FCC crystal rolls over an island edge. Then one of the three bonds to the underlying atoms is broken to a larger extent than if the adatom is rolling over a bridge site in a diffusion hop on a flat surface. Several theoretical calculations [2–4] for transition metal surfaces have shown, however, that such descent processes occur by a concerted displacement mechanism rather than by a hop over the step edge. Nevertheless, a significant ES barrier is typically present. The identification of the relevant transition mechanisms and characterization of the energy landscape for adatom migration on a growing surface is essential for gaining an understanding of the atomic scale mechanism of crystal and thin film growth and the conditions that can promote either 2D or 3D growth.

Sometimes the ES barrier is estimated simply as the difference between the energy barrier for descent starting from a site adjacent to the step edge minus the activation energy for diffusion on the flat terrace. Theoretical calculations using empirical potential functions, such as the embedded atom method (EAM) [10,11], that can be applied to large enough systems [3], as well as field ion microscope (FIM) measurements [5] surface show that the landscape is more complex. The site closest to the step edge can offer higher binding energy for the adatom, as can be understood from the low coordination of the step atoms (lower

* Corresponding author.
E-mail address: hj@hi.is (H. Jónsson).

https://doi.org/10.1016/j.surfin.2022.101944
Received 26 January 2022; Received in revised form 23 March 2022; Accepted 4 April 2022
Available online 6 April 2022

coordinated atoms form stronger bonds) but sites further away from the step can have lower binding energy than sites on the flat surface, leading to an excluded zone near the step edge, as has been observed in FIM measurements [6–9]. The energy barrier for adatom hops along and above the step edge can be small, as has been seen in EAM [10,11] calculations of Pt(111) [3], significantly smaller than either diffusion away from the step edge or descent to the lower layer. As a result, the adatom can be expected to diffuse along the top of the step edge. This increases the attempt frequency for descent but can also increase the probability of nucleation of a new island on top of an existing island.

It is important to use a single reference point when the energy of the adatom in various sites and at the transition state for atomic rearrangements is estimated. If the islands are large enough, the most likely landing site of an incoming atom is at a flat terrace and the majority species will be an adatom in the lowest energy site of an extended, flat terrace. The zero of energy is here taken to be the energy of an adatom at an FCC site of the Au(111) surface.

Measurements of growing metal surfaces, in particular (100) facet of copper, have shown that 2D growth can be achieved at surprisingly low temperature [12,13]. When growth at higher temperature leads to three-dimensional growth, this phenomenon is referred to as re-entrant layer-by-layer growth [14]. It has been documented particularly well for the growth of the (111) facet of platinum [14–17]. It is not clear how common re-entrant layer-by-layer growth is, in particular whether it holds for Au(111), a metal that is commonly used in experimental studies of nanostructures.

The key challenge in gaining understanding of the way conditions affect the growth mode is to identify the relevant atomic scale transition mechanisms. Usually this is assumed and postulated based on intuition, but a robust method for finding minimum energy paths for transitions, such as the nudged elastic band (NEB) method [18,19], makes the exploration of a large number of possible mechanisms feasible, as long as the computational effort in evaluating the system energy and atomic forces is not too large. Such calculations can reveal several unexpected mechanisms, as discussed below.

As an adatom migrates along the step edge, it is likely to run into defects such as kinks where a row of step atoms ends. It has been pointed out that kinks as well as corners of island edges (where A- and B-type steps meet) can affect the energy barrier for descent of a Pt adatom on the Pt(111) surface. This was first based on extensive exploration of transitions mechanisms using NEB and EAM potential function [3] and then later supported also by density functional theory (DFT) calculations [20]. There, it was shown that kink sites can offer significantly lower energy paths for descent as compared to straight edges. This is particularly important for B-type steps on Pt(111) since the activation energy for descent is estimated to be particularly large there [4] and the 3D islands formed in the intermediate temperature range tend to be triangular surrounded by B-type steps. An unexpected mechanism involving a concerted two atom displacement process where the adatom takes the place of an edge atom near – but not at – a kink site turned out to have a particularly low energy barrier. It is hard to verify such a mechanism experimentally for a one-component system since the atoms are indistinguishable. But, an experimental STM study of a Co adatom on a Pt (111) surface has indeed shown that a concerted displacement process facilitated by a kink site, is most likely to occur [21]. This could be inferred from the final state location of the Co atom.

In this article, we present studies of the energetics and transition mechanisms for a Au adatom on the Au(111) surface using NEB calculations where the energy of the system and atomic forces are evaluated using DFT within the generalized gradient approximation. In particular, we address the question whether kinks on steps play an important role in the interlayer transport and thereby the possibility that a Au(111) surface can show re-entrant layer-by-layer growth.

The article is organized as follows. The methods are described in section 2, including the systems studied, the electronic structure method used, and the method for finding minimum energy paths of transitions. Then, the results are presented in section 3 and a discussion presented in section 4. A brief conclusion is given in section 5.

2. Methods

The flat Au(111) terrace is simulated using a slab of atomic layers containing 16 atoms subject to periodic boundary conditions in the plane of the surface. The atoms in the bottom two layers are kept fixed while atoms are free to move in the top layer. The binding energy of the adatom at an FCC site is used to define the zero of energy for the adatom in all the calculations presented here. It is important to have a single well defined zero of energy when such a complex energy landscape is explored. If the zero of energy is shifted to whatever happens to be the initial configuration of the transition studied, then an incorrect estimate is obtained for the activation energy.

The straight A-type step, which has a {100} microfacet, is represented by a slab with Miller index (322) while the straight B-type step, which has a {111} microfacet, is represented by a slab with index (221). These are periodic arrays of steps with short terraces in between. Such models have previously been used extensively in DFT studies of the properties of steps and atomic transitions, such as chemical reactions, at steps. Kinks on an A-type step are represented by a slab with Miller index (956) while kinks on a B-type step are represented by a slab with Miller index (985). These models are analogous to the (854) and (874) surface slabs used by Feibelman [22] in calculations of adatom diffusion along step bottoms, except that the width of the terraces in between the steps is larger in the (956) and (985) models, making them a more accurate representations of an island edge. These configurations contain between 150 and 200 atoms, a relatively large number making these systemds computationally demanding in electronic structure calculations. A cross section of the model used here to study a periodic B-type step and the model used to study kinks on the B-type step are shown in Fig. 1.

The electronic structure calculations are carried out using DFT [23,24] within the generalized gradient approximation which is a step up in accuracy from the local density approximation (LDA) [25]. The calculations are carried out with the PBEsol functional [26] as it gives good estimate of surface energy and lattice constant of solids, quantities that affect the strength of adatom interaction with the surface. The energy of a Au atom in the gas phase is likely to be overestimated by the PBEsol functional and the absolute value of the binding energy therefore overestimated (more towards LDA than functionals optimized for atoms and molecular bonding). But this is not of concern since the question addressed here is the variation of the energy of the adatom as it undergoes transitions on the solid surface, not the energy of the adatom with respect to a gas phase atom. The DFT/PBEsol calculations give a lattice parameter of 4.08 Å for Au crystal, in close agreement with the experimental value of 4.07 Å. The valence electrons are described using a plane wave basis while the effect of inner electrons is described using the projected augmented wave (PAW) formalism [27]. An energy cutoff of 300 eV is used in the plane wave expansion. A 2x2x1 k-point sampling is used with Methfessel-Paxton smearing [28] at a temperature of 0.1 eV. The reported energy values correspond to extrapolation to zero temperature. The VASP software is used in these calculations [29].

The minimum energy paths for the various transitions are calculated using the NEB method [18,19] with the climbing image extension [30] and improved tangent estimate [31]. The initial paths are generated with the image dependent pair potential (IDPP) method [32]. The tolerance in the magnitude of atomic forces in optimizations of the atomic coordinates, both for identification of local minima and the images along the minimum energy paths, is 0.02 eV/Å. Typically, 5 intermediate images are used to represent paths in between the fixed endpoints, but this is specified further in the graphs below illustrating the calculated results.

Within the harmonic approximation to transition state theory (HTST), see review in ref. [20], the activation energy in the Arrhenius expression for the rate constant of an elementary transition is given by

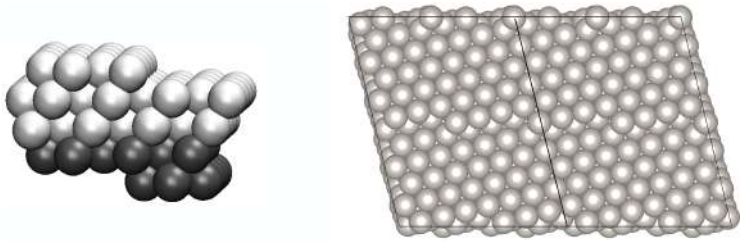

Fig. 1. Left: Cross section of the slab with (221) surface Miller index, used to study the straight B-type step. Light gray spheres indicate atoms that can move freely, while dark gray spheres indicate atoms that are fixed in order to represent the confining effects of missing atoms below. Right: On-top view of two simulation cells used to represent kinks on the B-type step, with Miller index (985).

the highest energy along the minimum energy path, a first order saddle point on the energy surface, minus the energy of the initial state minimum. The activation energy for a given downstepping mechanism reported below is calculated as the difference in the saddle point energy and the energy of the adatom in a FCC site on the flat surface. The HTST rate theory is the standard approach in calculations of rates of crystal growth transitions. The pre-exponential factor in the Arrhenius expression can also be found by calculating the vibrational modes at the saddle point and in the initial state, but we will assume here that the value of the pre-exponential factor does not vary between mechanisms enough to make a significant difference in the rates and we compare only the values of the activation energy.

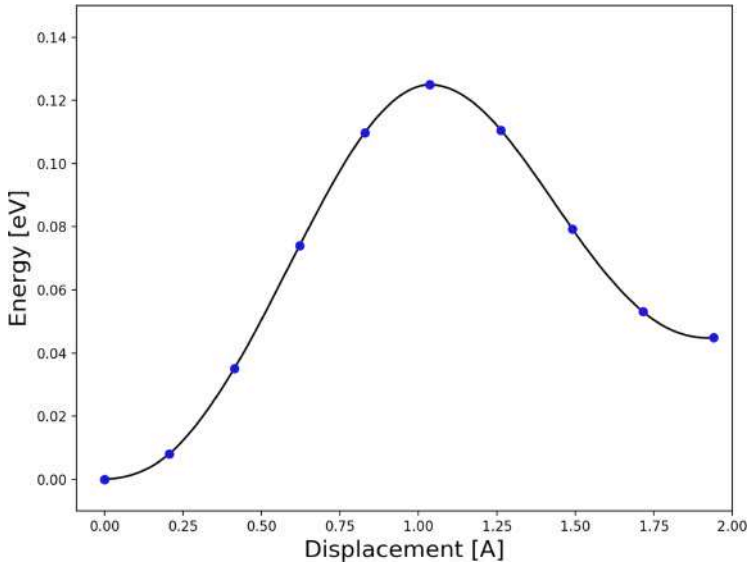

Fig. 2. Energy along the minimum energy path for adatom hop from an FCC site to an HCP site on the flat Au(111) surface. The complete diffusion path involves analogous hop in reverse from the HCP site to another FCC site. The activation energy for diffusion is found to be 0.12 eV and the energy difference between the two sites is 0.04 eV. The energy of the adatom at the FCC site on the (111) surface is taken to be the zero of energy in all the results presented here.

3. Results

The results of the NEB calculations of minimum energy paths are presented first for descent at steps, both straight and with a kink, and then paths for moving around a corner atom at a kink.

Fig. 2 shows the results obtained for a Au adatom diffusion hop on the flat (111) surface. The adatom starts at an FCC site and hops over a bridge to an HCP site where the binding energy is smaller by 0.04 eV. The completion of a diffusion path involves a second hop from the HCP site to another FCC site which is the reverse of the path shown. The activation energy for diffusion is found to be 0.12 eV. This is comparable to an estimate obtained in previous DFT calculations using the PBE functional, 0.15 eV (calculations using the more approximate LDA functional give 0.20 eV) [33].

3.1. Adatom descent

Figs. 3 and 4 show calculated minimum energy paths for the descent of an adatom at A- and B-type steps with and without a kink. The initial site of the adatom is adjacent to the step edge, an HCP site in the case of the A-type step but an FCC site in the case of the B-type step. The binding energy at the HCP site adjacent to the A-type step is nearly equal to that of the FCC site of the flat Au(111) surface. The fact that the step atoms are undercoordinated and thereby form stronger bonds to the adatom compensates here the reduced binding energy at HCP sites as compared to FCC sites. At the B-type step edge, however, the adjacent site is of FCC type and the undercoordination of the step atoms leads to larger binding energy by 0.03 eV, as can be seen from the downward shift in the corresponding initial point of the descent path in Fig. 2. The activation energy is the energy of the maximum along the minimum energy path with respect to the adatom at the FCC site on a flat Au(111) surface. The calculated activation energy for three different descent paths at the two types of steps are summarized in Table 1.

Table 1
Results of DFT/PBEsol calculations of the activation energy for a Au adatom descent at A- and B-type steps on the Au(111) surface, with and without a kink. The activation energy is the highest energy along the minimum energy path minus the energy of an adatom in an FCC site on the Au(111) surface. The uncertainty in the difference between values of the activation energy for different transition mechanisms of this type has been estimated to be ca. 0.02 eV [4].

Step type	Mechanism	Activation energy
A		
	straight	0.25
	at kink	0.16
	near kink	0.17
B		
	straight	0.31
	at kink	0.20
	near kink	0.14

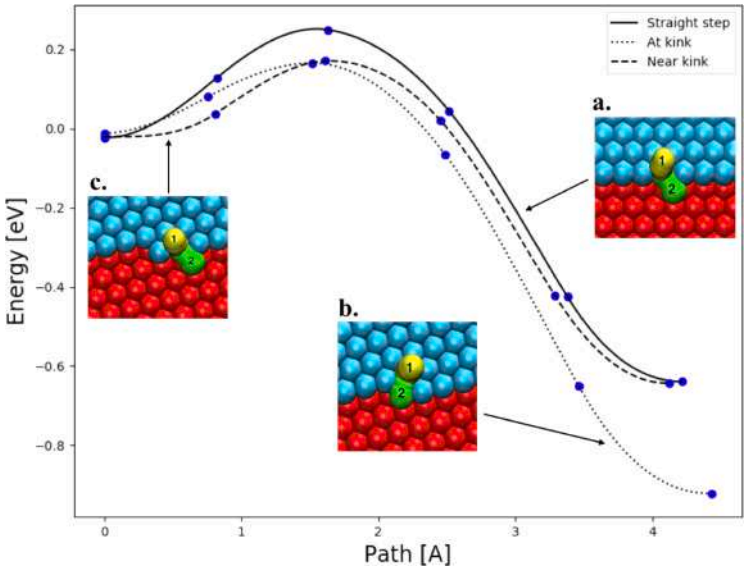

Fig. 3. Energy along minimum energy paths for the descent of an adatom at a straight A-type step (solid line), at kink (dotted line) and near kink (dashed line). Insets show the configurations of the atoms in the nudged elastic band images of the minimum energy paths. Points on the curves show energy of the intermediate system images in the discretization of the paths. The atom that starts as an adatom at the upper terrace is labeled 1, while the step atom that gets pushed out is labeled 2. A kink site provides paths for adatom descent with lower activation energy than a straight step (see Table 1 for numerical values).

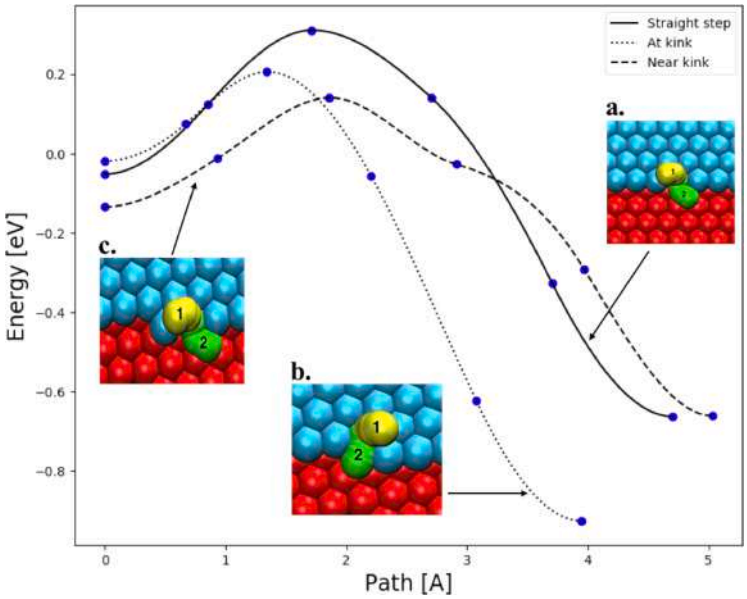

Fig. 4. Energy along minimum energy paths for the descent of an adatom at a straight B-type step (solid line), at kink (dotted line) and near kink (dashed line). Insets show the configurations of the atoms in the nudged elastic band images of the minimum energy paths. Points on the energy curve show energy of the intermediate system images in the discretization of the paths. The atom that starts as an adatom at the upper terrace is labeled 1, while the step atom that gets pushed out is labeled 2. Remarkably, the lowest activation energy is obtained for a descent mechanism that places an atom at the step edge near a kink site but not in the kink site, even though this mechanism leads to significantly higher final state energy (see Table 1 for numerical values).

The lowest activation energy for interlayer transport turns out to correspond to descent near a kink site on the B-type step. The initial site for this process is even lower in energy than the sites at the straight B-step, by about 0.1 eV and the activation energy for descent is 0.14 eV. This is substantially lower than the barrier for descent at a straight B-type step which is calculated to be 0.31 eV. Note that the final state energy is 0.3 eV higher for the path with lower activation energy because the final state does not correspond to an atom being placed at the 6-fold coordinated kink site but rather in a 5-fold coordinated site at the step edge. This shows that the height of the energy barriers does not scale with the final state energy. Such an approximation is, however, often invoked in crystal growth and chemical reaction calculations where energy barriers are not calculated but only estimated roughly.

The descent mechanism that involves placing an atom into the kink site at the B-type step rather than at the step edge near the kink site, corresponds to an intermediate value of the activation energy, 0.20 eV. The comparison of the two downstepping mechanisms at a kink on the B-type step again show that the activation energy does not scale with the energy of the final state.

Also for the A-type step, the kink offers paths for descent with lower activation energy than a straight step, but here the two kink related paths, the one that places an atom into the kink site and the one placing an atom at the step edge near the kink site, have similar activation energy, 0.16 and 0.17 eV. The lowest energy path for descent is, therefore, calculated to be descent near a kink site on the B-type step.

3.2. Rounding a corner

The preference for adatom descent into a site near but not at a kink site is important because it provides a seed for the formation of a new row of atoms and additional kink sites. A key issue then is whether such an atom can easily move from this rather high energy site to the nearby low energy kink site, either by rounding the corner atom or by a concerted displacement mechanism. The former mechanism turns out to have lower activation energy and the minimum energy paths for such transitions at both A-type and B-type steps are shown in Fig. 5. The insets show the atom configurations at the two endpoints and at each image in the converged NEB calculation of the transition path. The calculated energy barrier is large for both steps, over 0.5 eV, and the concerted displacement mechanism even higher, 0.7 eV. This means that an atom placed at a step after descent near a kink is not likely to move into the kink site if the temperature is not too high, for example at room temperature. The adatom can diffuse more readily along the step edge, with activation energy of 0.3 eV. This means that a new row of step atoms will

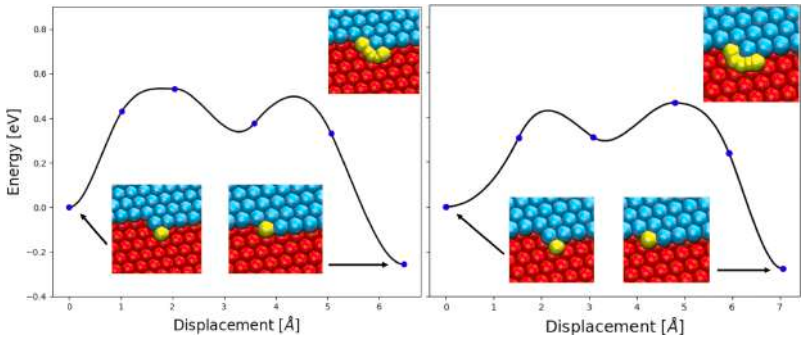

Fig. 5. Energy along minimum energy paths for an adatom to move from a 5-fold coordinated site at a step edge into a nearby 6-fold coordinated kink site. Left: at A-type step. Right: at B-type step. Insets show the configurations of the atoms at the two endpoints and for images of the system in converged nudged elastic band calculations of the minimum energy paths. The activation energy is high in both cases, over 0.5 eV, significantly higher than for adatom descent. At a temperature where descent near a kink is active while the rounding of the corner to enter the kink site is not, the step edge becomes rough and the number of kink sites proliferates promoting layer-by-layer growth.

form, introducing more kink sites and the low energy descent paths will, thereby, proliferate.

4. Discussion

The calculations presented here indicate that a Au adatom on top of an island on a Au(111) surface can descend to the lower layer most easily near a kink on a B-type step. This is similar to what has previously been deduced from calculations of a Pt adatom on a Pt(111) surface [3,20]. This nonintuitive mechanism was first predicted from extensive studies of various mechanisms using an EAM potential function for the Pt/Pt(111) system [3]. It has been used to explain signs of re-entrant layer-by-layer growth in kinetic Monte Carlo simulations of Pt(111) surface growth [34]. Since the same feature in the energy landscape is found here for a Au adatom on a stepped gold surface, the indication is that Au(111) may also show re-entrant layer-by-layer growth behavior. The sites adjacent to and above the B-type step offer 0.03 eV stronger binding than corresponding sites on the A-type step, so adatoms will tend to migrate to the top of B-type step edges. As the energy barrier for rounding the corner into a kink site is more than three times larger than the energy barrier for descent, there will be a range in temperature where descent is active but rounding the corner is not, so the step edge will become rough with multiple kinks, each offering a low energy path for descent, and thereby promoting layer-by-layer growth.

Experimental STM measurements of Pt(111) growth have shown that the transition from 3D to 2D growth as temperature is lowered down to room temperature coincides with a transition from compact islands with relatively straight steps to dendritic islands with high density of kinks [17]. Straight step edges lead to significant activation energy for descent, especially B-type steps [4], while the presence of kinks offers low energy paths for descent that can be active even at low temperature. Thus, even though the thermal energy of the adatoms is reduced as the temperature is lowered, the number of low barrier paths for descent is increased enough by the increase in kink density so that 2D growth reappears as the temperature is lowered.

While the differences in activation energy between competing transition mechanisms calculated are small, on the order of 0.1 eV, which is often quoted as an error bar for DFT calculations, the fact that only similar configurations of the system are being compared here and cancellation of errors can therefore be expected to be effective. The calculated activation energy differences presented here are likely meaningful and provide correct trends, for example in the comparison the different descent mechanisms. Also, the fact that various empirical potentials [3,34] and STM experiments on a related system [21] show similar features indicates that kink sites do indeed offer low energy paths for adatom descent.

The results presented here demonstrate the complexity of the energy landscape and the importance of choosing a single reference point for the energy of the adatom. If the activation energy of a downstepping event is estimated as the increase in energy with respect to the energy of the initial state for the elementary event, then the comparison between A- and B-type steps will be incorrect. The initial state for the downstepping event is higher in energy at the A-type step than at the B-type step because it corresponds to an HCP site rather than an FCC site. The initial site for the descent near a kink on the B-type step is even lower in energy, as can be seen in Fig. 4. The proper energy reference for all the adatom descent mechanisms is the energy of the adatom in an FCC site of a flat terrace since this represents the majority species.

The results of the NEB-DFT/PBEsol calculations presented here illustrate that a number of processes need to be taken into account to determine the fate of an adatom that lands on top of an island, and thereby answer the question whether the atom deposition leads to 2D or 3D growth. Some of these features are subtle and unexpected, but they can control the surface morphology of a growing crystal. The challenge to theoretical studies is to identify the relevant processes and estimate the rate of these processes accurately enough to be able to explain the surface patterns observed in experimental measurements and to predict the growth mode of materials that have not been studied experimentally. The most serious challenge is the problem of identifying the relevant atomic scale processes. As the calculations presented here illustrate, the key process may be nonintuitive. This calls for efficient algorithms for finding which processes can occur in the system under study at given conditions.

Since classical dynamics simulations cannot cover long enough time scales, advanced techniques are needed to search for likely transition mechanisms [20,35]. Long time scale simulation methods such as

adaptive kinetic Monte Carlo [36,37] have been used in combination with empirical potential functions in such studies, for example in simulations of Al(100) and Cu(100) growth [38], but the problem is that the more accurate and reliable DFT calculations have so far been computationally too demanding for such simulations. A possible future direction in this respect is the use of machine learning to interpolate between points in a training set of DFT calculations. The question still remains whether such an approach can be trusted to provide unexpected results since it represents only an interpolation between data fed into the machine learning algorithm. The most relevant part of the energy surface, corresponding to nonintuitive and unexpected mechanisms may be incorrectly represented since the training set will likely not contain such configurations. The challenge of explaining how microscopic processes influence macroscopic behavior is particularly relevant in studies of growth shapes of crystals, which offer a unique testing ground for the computational challenges of bridging vast length and time scales.

As mentioned in the introduction, there is great interest in Au nanoparticles and therefore also the growth modes of Au nanoparticles. Recently, intriguing experimental observations have been made where Au nanoparticles were grown by reduction of precursors using an electron beam [39]. As a function of time, switches between disordered and ordered structures were observed until, eventually, as the nanoparticles became large enough the ordered structure dominated. More often, nanoparticles are grown by precipitation from solution, and there again it is important to gain an understanding of how the growth mode depends on conditions such as temperature and concentration of precursors [40]. Chemical vapor deposition can also be used, even one-step catalyst-free thermal chemical vapor deposition, as has been demonstrated in growth of Au nanoparticles on silicon substrates [41]. There, single-crystal nanoparticles with various morphologies such as prism, icosahedron, and five-fold twinned decahedron were formed. The shape of such nanoparticles is governed by the kinetic processes that take place as atoms land on the particle surface, including the processes studied here, as well as many others. A full description of the growth of nanoparticles requires calculations of additional atomic scale rearrangements, and then a long timescale simulations of the growth under specific conditions.

5. Conclusion

The theoretical results presented here, based on calculations of minimum energy paths for the descent of a Au adatom from atop an island into the growing layer, show that kinks on the step edge provide paths with lower activation energy than straight steps. This is found to be the case for both A- and B-type steps, as summarized in Table 1. The binding energy of an adatom is particularly large at sites adjacent to and above the B-type step, so adatoms landing on top of an island are more likely to drift to such sites. At the straight B-type step, the activation energy for descent is found to be higher than at the A-type step, 0.31 eV *vs.* 0.25 eV, but a non-intuitive downstepping process that places an adatom next to – but not into – a kink site has a particularly low activation energy of 0.14 eV, representing essentially zero Ehrlich-Schwöbel barrier (the activation energy for diffusion on the flat (111) terrace is calculated to be 0.12 eV). This unexpected result illustrates that the activation for the various downstepping mechanisms does not scale with the final state energy, since a lower barrier leads to a higher energy final state in this case. The energy barrier for an adatom at the bottom of a step edge to round the corner and enter a kink site is found to be large, so the non-intuitive downstepping near a kink on a B-type step will likely lead to the formation of a new row of step atoms and thereby more kink sites, offering larger number of low barrier paths for descent.

The features of the energy landscape representing the interaction of a Au adatom with the crystal surface described above are in many ways similar to those found earlier for a Pt adatom on a Pt(111) surface and one can expect similar growth modes to occur. While layer-by-layer growth is in any case going to be taking place at a temperature that is high enough for the adatoms to overcome energy barriers for downstepping, an intermediate temperature range where diffusion along island edges is active and the steps therefore tend to be straight and free of kinks will likely give 3D growth since the barrier for descent at straight steps is relatively high, significantly higher than diffusion on the flat terrace. The corresponding Ehrlich-Schwöbel barrier is 0.2 eV at the B-type step. Then, as the temperature is lowered further and diffusion of adatoms along the step bottoms becomes hindered, the steps will develop kinks and a new low barrier descent mechanism becomes available. Since the downstepping at kinks on a B-type step is most likely going to place an adatom near but not at a kink site, a new row of step atoms is nucleated, generating new kinks and additional low barrier paths for descent. This can lead to re-entrant layer-by-layer growth, as has been observed experimentally for Pt(111). The main conclusion of the work presented here is, therefore, that Au(111) growth is likely to show re-entrant layer-by-layer behavior analogous to that of Pt(111). This can have significant consequences for the various methods that are being developed for growing Au nanoparticles of particular shape. The functionality of Au nanoparticles in various applications, such as catalysis, is strongly dependent on the shape of the nanoparticle and thereby the abundance of the various types of sites on the surface.

Declaration of Competing Interest

The authors declare the following financial interests/personal relationships which may be considered as potential competing interests:

Hannes Jonsson reports financial support was provided by Horizon 2020.

Acknowledgement

This work was funded by the European Union's Horizon 2020 research and innovation programme under the Marie Sklodowska Curie Innovative Training Network ELENA, grant agreement No. 722149 and by the Icelandic Science Fund.

References

[1] R.L. Schwöbel, E.J. Shipsey, Step motion on crystal surfaces, J. Appl. Phys. 37 (1966) 3682.G. Ehrlich and F. G. Hudda, Atomic view of surface self-diffusion: Tungsten on tungsten, J. Chem. Phys. 44, 1039 (1966)
[2] M. Villarba, H. Jónsson, Low temperature homoepitaxial growth of pt(111) in simulated vapor deposition, Phys. Rev. B 49 (1994) 2208.
[3] M. Villarba, H. Jónsson, Diffusion mechanisms relevant to metal crystal growth: Pt/pt(111), Surf. Sci. 317 (1994) 15.
[4] P.J. Feibelman, Interlayer self-diffusion on stepped pt(111), Phys. Rev. Lett. 81 (1998) 168.
[5] S.C. Wang, G. Ehrlich, Atom incorporation at surface clusters: An atomic view, Phys. Rev. Lett. 67 (1991) 2509.
[6] S.C. Wang, G. Ehrlich, Adatom motion to lattice steps: A direct view, Phys. Rev. Lett. 70 (1993) 41.
[7] S.C. Wang, G. Ehrlich, Atom condensation at lattice steps and clusters, Phys. Rev. Lett. 71 (1993) 4174.
[8] A. Gölzhäser, G. Ehrlich, Atom movement and binding on surface clusters: Pt on pt (111) clusters, Phys. Rev. Lett. 77 (1996) 1334.
[9] K. Kyuno, G. Ehrlich, Step-edge barriers: An atomistic view, Phys. Rev. Lett. 81 (1998) 5592.
[10] M.S. Daw, M.I. Baskes, Embedded-atom method: Derivation and application to impurities, surfaces, and other defects in metals, Phys Rev. B 29 (1984) 6443.
[11] M.S. Daw, Model of metallic cohesion: The embedded-atom method, Phys. Rev. B 39 (1989) 7441.
[12] J.J. de Miguel, A. Sanchez, A. Cebollada, J.M. Callego, J. Ferron, S. Ferrer, The surface morphology of a growing crystal studied by thermal energy atom scattering (TEAS), Surf. Sci. 189/190 (1987) 1062.
[13] W.F. Egelhoff, I. Jacob, Reflection high-energy electron diffraction (RHEED) oscillations at 77 k, Phys. Rev. Lett. 62 (1989) 921.
[14] R. Kunkel, B. Poelsema, L.K. Verheij, G. Comsa, Reentrant layer-by-layer growth during molecular-beam epitaxy of metal-on-metal substrates, Phys. Rev. Lett. 65 (1990) 733.
[15] B. Poelsema, R. Kunkel, N. Nagel, A.F. Becker, G. Rosenfeld, L.K. Verheij, G. Comsa, New phenomena in homoepitaxial growth of metals, Appl. Phys. A 53 (1991) 369.

[16] B. Poelsema, A. Becker, G. Rosenfeld, R. Kunkel, N. Nagel, L.K. Verheij, G. Comsa, On the shape of the in-phase TEAS oscillations during epitaxial growth of pt(111), Surf. Sci. 272 (1992) 269.
[17] M. Kalf, G. Comsa, T. Michely, How sensitive is epitaxial growth to adsorbates, Phys. Rev. Lett. 81 (1998) 1255.
[18] G. Mills, H. Jónsson, G.K. Schenter, Reversible work transition state theory: application to dissociative adsorption of hydrogen, Surf. Sci. 324 (1995) 305.
[19] H. Jónsson, G. Mills, K.W. Jacobsen, in Classical and Quantum Dynamics in Condensed Phase Simulations, World Scientific, 1998.**Page 385**
[20] H. Jónsson, Theoretical studies of atomic scale processes relevant to crystal growth, Ann. Rev. Phys. Chem. 51 (2000) 623.
[21] E. Lundgren, B. Stanka, G. Leonardelli, M. Schmid, P. Varga, Interlayer diffusion of adatoms: A scanning-tunneling microscopy study, Phys. Rev. Lett. 82 (1999) 5068.
[22] P.J. Feibelman, Self-diffusion along step bottoms on pt(111), Phys. Rev. B 60 (1999) 4972.
[23] P. Hohenberg, W. Kohn, Inhomogeneous electron gas, Phys. Rev. 136 (1964) B864.
[24] W. Kohn, L.J. Sham, Self-consistent equations including exchange and correlation effects, Phys. Rev. 140 (1965) A1133.
[25] J.P. Perdew, Jacob's ladder of density functional approximations for the exchange-correlation energy, AIP Conf. Proc. 577 (2001) 1.
[26] J.P. Perdew, J.P. Perdew, A. Ruzsinszky, G.I. Csonka, O.A. Vydrov, G.E. Scuseria, L. A. Constantin, X. Zhou, K. Burke, Restoring the density-gradient expansion for exchange in solids and surfaces, Phys. Rev. Lett. 100 (2008) 136406.***Phys. Rev. Lett.*****102**, 039902 (2009)
[27] P.E. Bloechl, Projector augmented-wave method, Phys. Rev. B 50 (1994) 17953.
[28] M. Methfessel, A.T. Paxton, High-precision sampling for brillouin-zone integration in metals, Phys. Rev. B 40 (1989) 3616.
[29] G. Kresse, J. Hafner, Phys. Rev. B 47 (1993) 558.**49**, 14251 (1994); G. Kresse and J. Furthmüller, Comput. Mater. Sci. **6**, 16 (1996); Phys. Rev. B **55**, 11169 (1996)
[30] G. Henkelman, B. Uberuaga, H. Jónsson, A climbing-image NEB method for finding saddle points and minimum energy paths, J. Chem. Phys. 113 (2000) 9901.
[31] G. Henkelman, H. Jónsson, Improved tangent estimate in the NEB method for finding minimum energy paths and saddle points, J. Chem. Phys. 113 (2000) 9978.
[32] S. Smidstrup, A. Pedersen, K. Stokbro, H. Jónsson, Improved initial guess for minimum energy path calculations, J. Chem. Phys. 140 (2014) 214106.
[33] J.J. Mortensen, B.H. Bjørk, O.H. Nielsen, K.W. Jacobsen, J.K. Nørskov, Density functional theory study of self-diffusion on the (111) surfaces of ni, pd, pt, cu, ag and au, Springer Ser. Solid State Phys. 121 (1996) 173.
[34] J. Jacobsen, K.W. Jacobsen, P. Stoltze, J.K. Nørskov, Island shape-induced transition from 2d to 3d growth for pt/pt(111), Phys. Rev. Lett. 74 (1995) 2295.
[35] H. Jónsson, Simulation of surface processes, Proc. Natl. Acad. Sci. 108 (2011) 944.
[36] G. Henkelman, H. Jónsson, Long time scale kinetic monte carlo simulations without lattice approximation and predefined event table, J. Chem. Phys. 115 (2001) 9657.
[37] S.T. Chill, M. Welborn, R. Terrell, L. Zhang, J.-C. Berthet, A. Pedersen, H. Jónsson, G. Henkelman, EON: Software for long time simulations of atomic scale systems, Modelling and Simulation in Materials Science and Engineering 22 (2014) 055002.
[38] G. Henkelman, H. Jónsson, Multiple time scale simulations of metal crystal growth reveal importance of multi-atom surface processes, Phys. Rev. Lett. 90 (2003) 116101.
[39] S. Jeon, et al., Reversible disorder-order transitions in atomic crystal nucleation, Science 371 (2021) 498.
[40] T. Nguyen, K. Thanh, N. Maclean, S. Mahiddine, Mechanisms of nucleation and growth of nanoparticles in solution, Chem. Rev. 114 (2014) 7610.
[41] S. Manna, J.W. Kim, Y. Takahashi, O.G. Shpyrko, E.E. Fullerton, Synthesis of single-crystalline anisotropic gold nano-crystals via chemical vapor deposition, J. Appl. Phys. 119 (2016) 174301.

Article III

Indirect Mechanism of Au adatom Diffusion on the Si(100) Surface

Alejandro Peña-Torres, Abid Ali, Michail Stamatakis, Hannes Jónsson

Physical Review B, 105, 205411 (2022)

PHYSICAL REVIEW B **105**, 205411 (2022)

Indirect mechanism of Au adatom diffusion on the Si(100) surface

Alejandro Peña-Torres and Abid Ali
Science Institute of the University of Iceland, VR-III, IS-107 Reykjavík, Iceland

Michail Stamatakis
Department of Chemical Engineering, University College London, Roberts Building, Torrington Place, London WC1E 7JE, United Kingdom

Hannes Jónsson
Faculty of Physical Sciences, University of Iceland, VR-III, IS-107 Reykjavík, Iceland and Department of Applied Physics, Aalto University, FI-00076 Espoo, Finland

(Received 7 March 2022; revised 14 April 2022; accepted 27 April 2022; published 6 May 2022)

Calculations of the diffusion of a Au adatom on the dimer reconstructed Si(100)-2 × 1 surface reveal an interesting mechanism that differs significantly from a direct path between optimal binding sites, which are located in between dimer rows. Instead, the active diffusion mechanism involves promotion of the adatom to higher-energy sites on top of a dimer row and then fast migration along the row, visiting ca. a hundred sites at room temperature, before falling back down into an optimal binding site. This top-of-row mechanism becomes more important the lower is the temperature. The calculations are carried out by finding minimum energy paths on the energy surface obtained from density functional theory within the PBEsol functional approximation followed by kinetic Monte Carlo simulations of the diffusion over a range of temperature from 200 to 900 K. While the activation energy for the direct diffusion mechanism, both parallel and perpendicular to the dimer rows, is calculated to be 0.84 eV, the effective activation energy for the indirect mechanism parallel to the rows is on average 0.56 eV.

DOI: 10.1103/PhysRevB.105.205411

I. INTRODUCTION

The formation of metallic nanostructures on solid surfaces has become the focus of various types of research and technological applications [1] as they can have interesting properties, such as optical, electronic, and catalytic [2,3]. Gold nanostructures are often of particular interest because of their stability and silicon surfaces represent a natural choice for a substrate because of its widespread use in electronic applications. For example, gold nanoparticles formed on a silicon surface can be used as metal catalysts in the synthesis of one-dimensional nanostructures such as carbon nanotubes [4] and silicon nanowires [5]. They have also been found to display interesting optical properties [6] and to form mesoscopic structures [7]. Moreover, the presence of a gold overlayer on silicon has proven to play an important role in the growth mechanism of silicon oxide [8] and other materials [9]. Stripes of Au on silicon surfaces have also been studied extensively in recent years, for example, the electronic structure and surface dynamics of Au wires on flat [10] and stepped [11,12] silicon surfaces.

An understanding of the interaction between Au atoms and the Si surface as well as the initial stages of Au nanostructure formation is therefore of considerable importance. Epitaxial growth of gold islands and overlayers on Si(100) have been studied by scanning and high-resolution transmission electron microscopy, electron diffraction, and grazing-incidence x-ray diffraction [13–15]. More detailed information about the Au/Si(100) interaction has been obtained from the low-temperature scanning tunneling microscopy (STM) studies of Chiaravalloti *et al.* where the binding sites of Au adatoms on the silicon surface could be identified [16] both in between the Si dimer rows of the reconstructed Si(100)-2 × 1 surface and on top of the dimer rows. An adatom initially sitting on top of a row was observed to move in between rows during STM manipulation, indicating that the latter site is more stable. Previous density functional theory (DFT) studies had reported binding sites in between the dimer rows (BDRs) [17] and there it was assumed that diffusion occurs by adatom hops between such binding sites, the adatom thereby remaining in between dimer rows during diffusion. More extensive DFT calculations by Chiaravalloti *et al.*, however, identified also two binding sites on top of the dimer rows, an asymmetric site at the edge of the dimer row (TDR1) and a symmetric site in the center of a row (TDR2). The question then arises how Au adatoms diffuse on the surface, in particular whether the TDR sites play some role there or whether the diffusion occurs by direct hopping between the optimal BDR sites. This will, for example, affect where dimers form and how Au islands nucleate on the surface.

In this paper, results of theoretical calculations of the diffusion of a Au adatom on the reconstructed Si(100)-2 × 1

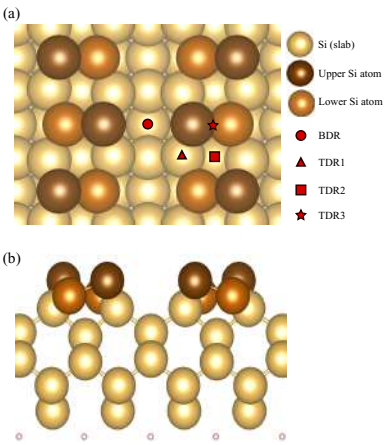

FIG. 1. (a) Top and (b) side views of the clean Si(100)-2 × 1 surface. The buckled dimers are highlighted with a brown (orange) color for the upper (lower) Si atoms, and the capping hydrogen atoms are shown in lighter color. The binding sites of the Au adatom, in between dimer rows (BDR, representing both BDR1 and BDR2—see Fig. 2) and on top of a dimer row (TDR1, TDR2 and TDR3), are marked with red symbols.

surface are presented. The study is based on nudged elastic band (NEB) calculations of minimum energy paths for elementary transitions with the energy and atomic forces estimated from DFT calculations with the Perdew-Burke-Ernzerhof exchange-correlation density functional (PBEsol) for metallic bulk and surface systems. The results, combined with rate estimates based on harmonic transition state theory, are used in kinetic Monte Carlo (KMC) simulations of Au adatom diffusion over a range of temperatures. The optimal diffusion mechanism turns out to be nonintuitive and indirect involving Au adatom hopping on top of a dimer row and then migration along the row long distance between visits to the low-energy BDR sites. The effective activation energy turns out to be significantly smaller than that of the more direct diffusion path between BDR sites.

II. METHODOLOGY

The reconstructed Si(100)-2 × 1 surface is modeled with a periodic 4 × 4 surface supercell of a six-layer slab. The three upper layers are allowed to relax while the rest of the atoms are kept frozen at the perfect crystal positions. The bottom silicon layer is passivated with hydrogen atoms. The system is illustrated in Fig. 1.

To calculate the minimum energy paths between the local minima corresponding to the Au adatom binding sites, the climbing image NEB (CI-NEB) method is used [18–20]. The image-dependent pair potential (IDPP) method [21] with six intermediate images is used to generate the initial paths. Iterative optimization of atomic coordinates is carried out until the magnitude of the components of the atomic forces perpendicular to the path have dropped below 0.01 eV/Å.

The energy of the system and atomic forces are estimated using DFT within the PBEsol functional approximation [22]. PBEsol is chosen here because it is known to give good results for the silicon crystal and its surface, including the surface energy. It is closer to the local density approximation (LDA) than the PBE approximation in that the exchange enhancement factor is smaller. As a result, the energy of an isolated atom is higher with PBEsol and the binding energy to the surface therefore overestimated, but this error will be similar for all binding sites on the surface and not affect the shape of the energy landscape for the adatom. A plane-wave basis set is used with a cutoff energy of 350 eV to represent the valence electrons, while the inner electrons are represented with the projector augmented-wave method [23]. Calculations of the crystal give a lattice parameter of 5.43 Å, in excellent agreement with the experimental value. A vacuum space of 15 Å is used to avoid interactions between periodic images of the slab. The Brillouin zone is sampled using a uniform mesh with 7 × 7 × 1 k points. The calculations are carried out with the EON software [24] with energy and atomic forces obtained from VASP [25].

The values of the activation energy E_a for each elementary hop of the Au adatom from one binding site to another are obtained from the minimum energy paths as the maximum energy along the path minus the initial state energy, given by the harmonic approximation to transition state theory (HTST) (for a review, see Ref. [20]). The rate constants for the various processes are then estimated using the Arrhenius expression $k = \nu \exp(-E_a/k_B T)$, where the preexponential factor is taken to have a typical value of $\nu = 10^{12}$ s^{-1}. The transition mechanisms and estimated rate constants are then used to prepare input for a KMC simulation of the diffusion over a larger area of the surface and a range of temperature values using the ZACROS software [26,27]. The possibility for desorption or adsorption of gold atoms is not included as the goal here is to identify the possible diffusion paths of a single Au adatom.

III. RESULTS AND DISCUSSION

A. Binding sites

It is well known that the Si(100) surface undergoes a reconstruction to form an extended 2 × 1 surface unit cell where dimer rows are formed to reduce dangling bonds. The calculations were started from the unreconstructed Si(100) surface, with two dangling bonds for every surface Si atom. During energy minimization with respect to coordinates of the movable atoms, buckled dimer rows form as shown in Fig. 1. The resulting arrangement of the surface atoms corresponds to the $c(4 \times 2)$ reconstruction where the buckling of dimers in adjacent Si dimer rows follows opposite patterns. This structure has been observed in both low-temperature STM experiments [28] and in simulations [29] and is found to be the

TABLE I. Binding energy (in eV) of a Au adatom at various adsorption sites on the Si(100)-2 × 1 surface, calculated with the PBEsol and PBE functional approximations. The Si-Au-Si angle is given in parentheses (in degrees).

	DFT/PBEsol	DFT/PBE[a]
BDR1	3.44 (140°)	3.24 (131°)
BDR2	2.91 (170.5°)	
TDR1	3.12 (100°)	3.03 (98°)
TDR2	3.07 (121°)	2.94 (118°)
TDR3	2.87 (58°)	

[a]Data from Ref. [16].

predominant configuration of the surface above 120 K. The calculations give a dimer bond length of 2.34 Å and a buckling angle of 19.8°. This agrees quite well with data obtained from low-energy electron diffraction (LEED) experiments giving values of 2.24 Å and 19.2° [30].

The three binding sites of the Au adatom identified by Chiaravalloti *et al.* [16] are first calculated by placing the adatom in the vicinity of these locations and minimizing the energy with respect to the coordinates of all the movable atoms. These binding sites are labeled as BDR1, TDR1, and TDR2, as indicated in Fig. 1. After the local minimum has been reached, the binding energy E_b is calculated as

$$E_b = E_{\text{surf}} + E_{\text{Au}} - E_{\text{Au/surf}}, \tag{1}$$

where $E_{\text{Au/surf}}$ and E_{surf} correspond to the energy of the silicon slab with and without the Au adatom and E_{Au} is the energy of an isolated Au atom. Table I shows the values obtained here with the PBEsol functional as well as the PBE values obtained previously by Chiaravalloti *et al.* [16]. The two functionals give similar values, the PBEsol binding energy being larger by about 0.1–0.2 eV as could be expected from the overestimate of the energy of the isolated Au atom.

At all the binding sites, the Au adatom is stabilized by bonding to two Si-dimer atoms. The Si-Au-Si angle formed is given in Table I. The BDR1 position represents the most stable adsorption site, consistent with the fact that it is the most frequently observed configuration in the low-temperature STM measurements [16]. The TDR1 and TDR2 sites appear to be nearly equally stable, with a binding energy difference of only 0.05 eV in the PBEsol calculations.

An additional local minimum in the BDR position has also been found (from now on referred to as BDR2) where the Au adatom is located ≈1 Å closer to the surface as compared to the previously known BDR1 configuration. Figure 2 shows a side view comparison between these two configurations of the atoms. The calculated binding energy for the BDR2 configuration is 2.91 eV, about 0.5 eV smaller than the one obtained for the BDR1 site. There, the Au atom is again bonded to two Si-dimer atoms but forms a significantly larger Si-Au-Si angle of 170.5°.

B. Diffusion mechanism

The mechanism of Au adatom diffusion on the surface is found by identifying the minimum energy paths connecting the binding sites. The results are shown in Fig. 3. Starting

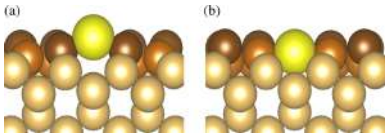

FIG. 2. Side view of the two local minima found for the Au adatom placed in between silicon dimer rows (BDR sites). The Au adatom is displayed in yellow and the Si-dimer atoms are colored in brown. The Au adatom in the lower site, BDR2, shown in (b), is 1 Å closer to the surface than in the more stable upper site, BDR1, shown in (a).

with the adatom in one of the most stable binding sites, a BDR1 site, an initial path to an adjacent BDR1 site is generated using the IDPP method. The NEB optimization of the path results in a longer path that visits a TDR1 site as an intermediate minimum. It turns out that there is no minimum energy path between two BDR1 sites that does not include an intermediate minimum. The calculated activation energy for the BDR1→TDR1 hop is 0.84 eV, while the opposite process, a jump back to the same or an adjacent BDR1 site, has an activation energy of 0.52 eV. Once the Au adatom is in a TDR1 site, it has, however, other options than to fall down to a BDR1 site. A hop to a TDR2 site at the center of the dimer row has a lower activation energy of 0.12 eV. From the TDR2 site, the adatom can either go back to the TDR1 site by overcoming a barrier of only 0.08 eV, or it can slide over a silicon dimer to get to an adjacent TDR2 site. The CI-NEB calculation of the path between two TDR2 sites reveals an intermediate binding site where the adatom sits on top of a Si dimer. (This site is labeled as TDR3 in Figs. 1 and 3.) The energy barrier for the TDR2→TDR3 hop is 0.24 eV. The TDR2→TDR2 process can also involve dissociation of the Si dimer as the Au atom goes through it instead of going over it. However, this process has an activation energy of 0.57 eV, making it less likely.

It is worth noting that the diffusion of the Au adatom on the surface involves a local change in the tilt of Si dimers. From the on-top views in Fig. 3, it can be seen how during the BDR1→TDR1 transition, a Si dimer flips in order to stabilize the Au atom in the TDR1 configuration. Then, in order to get to the next BDR1 site, the Si dimer in the adjacent dimer row flips as well. Similarly, when the Au atom hops on top of a Si dimer in the TDR3 site, the tilt is eliminated, but then the dimer tilts again once the Au atom has passed by. The energy barriers reported here correspond to the diffusion of a Au adatom on the $c(4 \times 2)$ reconstruction of the Si(100) surface and take these local changes in the dimer tilt into account. Similar values of the energy barriers are obtained for diffusion on the $p(2 \times 2)$ reconstructed surface, the difference being on the order of 0.01 eV.

In summary, the diffusion from one BDR1 site to another can occur via two possible paths (illustrated in Fig. 4). In the most direct path, the Au adatom goes first to a TDR1 site and then to another BDR1 site. Another, less direct path involves visiting also TDR2 sites from the TDR1 site and possibly extended travel along the silicon dimer row until

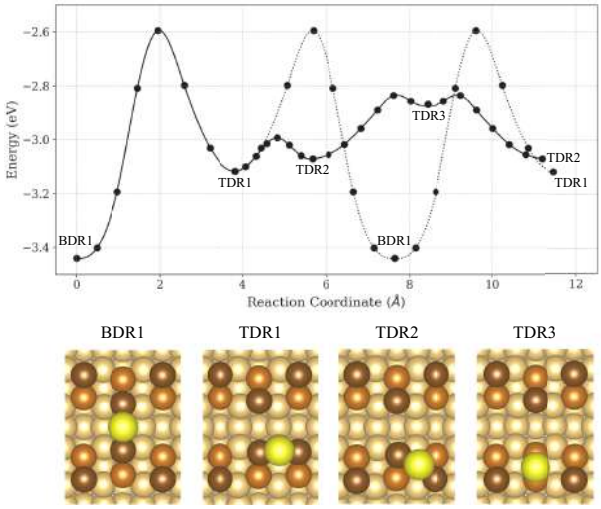

FIG. 3. Calculated minimum energy paths between the main adsorption sites obtained using the CI-NEB method with DFT/PBEsol atomic forces. Each dot corresponds to an image of the system along the path. Bottom panels correspond to on-top view of the BDR1, TDR1, TDR2, and TDR3 configurations. The TDR3 site was discovered as an intermediate minimum in the CI-NEB calculation of the minimum energy path between adjacent TDR2 sites.

the adatom eventually jumps back down to a BDR1 site. The latter process takes place via the TDR1 configuration with an overall activation energy of 0.52 eV. In order to study the competition between these different diffusion mechanisms, KMC simulations of the long-timescale dynamics were carried out for a range in temperature.

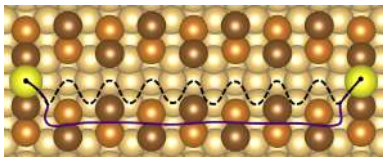

FIG. 4. Illustration of the two competing diffusion paths for the Au adatom. The dashed line represents the most direct diffusion path between optimal sites, BDR1→TDR1→BDR1. The solid line indicates schematically the more efficient indirect path involving fast migration on top of a dimer row between TDR1, TDR2 and TDR3 sites before falling back down again into one of the optimal BDR1 binding sites.

IV. KINETIC MONTE CARLO SIMULATIONS

As mentioned in the Methodology section, the activation energy (E_a) for each elementary transition included in the KMC simulations is obtained from the DFT/PBEsol calculations as the energy difference between the maximum energy along the minimum energy path and the initial state minimum, as given by HTST. Although the preexponential factor of the Arrhenius expression for the rate can be estimated using HTST by calculating the vibrational modes at the initial state and at the saddle point, we assume here that its value does not vary significantly for the transitions involved and use a typical value of 10^{12} s^{-1}.

The lattice used in the KMC simulations includes only the most relevant adsorption sites (i.e., BDR1, TDR1, and TDR2), as illustrated in Fig. 5. The elementary transitions included correspond to the reversible adatom hops: (1) between BDR1 and TDR1; (2) between TDR1 and TDR2; and (3) between adjacent TDR2 sites. Adsorption or desorption of the Au atom is not included in the simulations. The initial configuration corresponds to a Au atom adsorbed in one of the BDR1 sites.

A total of ten simulations were carried out for seven values of the temperature: 200, 250, 300, 400, 500, 700, and 900 K. For each simulation, a different random number seed was used to generate independent instances of time evolution of

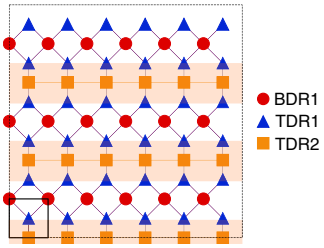

FIG. 5. Illustration of the lattice of sites included in the KMC simulations of the diffusion of the Au atom. For simplicity, the weakly binding TDR3 site is not included in the simulations.

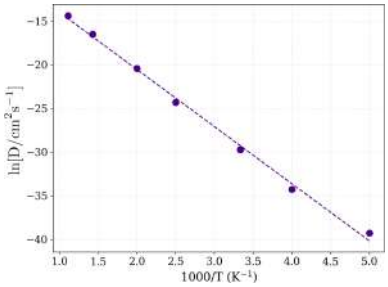

FIG. 6. Arrhenius graph of the Au adatom diffusion coefficient D on Si(100)-2 × 1 as a function of temperature in the range 200–900 K. The linear fit gives an effective activation energy of 0.56 eV. There is, however, clear deviation from linear dependence because the indirect mechanism of skidding along a dimer row becomes more important as the temperature is lowered.

the system. An average of 5×10^{09} KMC events occurred in each simulation. Table II presents the average time spent in a BDR1 site as well as the average time spent on top of a dimer row and number of TDR2 sites visited in between BDR1 sites. The results show that the Au adatom tends to skid along a dimer row, especially at low temperature, rather than following the BDR1→TDR1→BDR1 path. This preference at low temperature stems from the fact that once the adatom has made it to a TDR1 site, the energy barrier for skidding along a dimer row is lower than the barrier for entering a BDR1 site. At high temperature, this difference in barrier height is less important and the BDR1→TDR1→BDR1 path becomes more competitive.

The KMC results give a value for the average distance traveled by the Au adatom along a dimer row in between visits to BDR1 sites. This can be used to estimate the diffusion coefficient D assuming a one-dimensional random walk between BDR1 sites as

$$D(T) = \frac{L^2}{2\tau}, \tag{2}$$

where L is the average length traveled and τ_{BDR1} is the average time spent at a BDR1 site before hopping on top of a dimer row. Figure 6 shows the Arrhenius graph of this estimate of the diffusion coefficient. Since the skidding along a dimer row is more important relative to the more direct BDR1→TDR1→BDR1 path at low temperature, the relationship is not linear, but a straight line fit to the whole range from 200 to 900 K gives an average slope corresponding to an effective activation energy for diffusion as 0.56 eV. The slope, however, is lower in the lower-temperature range than in the high-temperature range as the relative importance of the two diffusion mechanisms changes with temperature. This value of the effective activation energy is significantly lower than the activation energy for the direct BDR1→TDR1→BDR1 path which is 0.84 eV. Figure 4 shows a depiction of the competing diffusion paths. The solid line indicates a simplified description of the indirect mechanism where the adatom hops on top of a dimer row in rapid migration. The dashed line represents the more direct BDR1→TDR1→BDR1 mechanism that becomes competitive only at high temperature.

TABLE II. Results of kinetic Monte Carlo simulations at various values of the temperature. τ_{BDR1} is the average time in seconds spent in a BDR1 site, τ_{TDRs} is the time spent on sites on top of dimer rows in between visits to BDR1 sites, and L/d is the length traveled along the top of a dimer row divided by the BDR1 site separation, $d = 3.84$ Å.

T (K)	τ_{BDR1}	τ_{TDRs}	L/d
200	3.5×10^{08}	2.7×10^{-01}	1910
250	2.3×10^{04}	1.2×10^{-03}	240
300	3.0×10^{01}	2.0×10^{-05}	72
400	9.4×10^{-03}	2.0×10^{-07}	19
500	6.8×10^{-05}	1.6×10^{-08}	11
700	2.8×10^{-07}	7.9×10^{-10}	5
900	1.2×10^{-08}	1.3×10^{-10}	3

At high temperature, the transition between TDR1 and TDR2 sites is not well described by HTST due to the low-energy barrier of 0.08 eV. This, however, does not significantly affect the results presented here. It is not important to include explicitly the TDR2 site in the KMC simulations as it can simply be merged with the TDR1 site. The results of KMC simulations using this reduced model give average time spent at BDR sites and average length traveled on top of a dimer row of same order of magnitude as the ones where the TDR2 site is included explicitly.

Both parallel and perpendicular diffusion paths with respect to the dimer rows involve traversing through the same saddle point on the energy surface 0.84 eV above the energy of the BDR1 site. The activation energy for diffusion in the two directions obtained directly from the energy surface is therefore the same and from this one would conclude that the diffusion is isotropic. However, since the repeated hopping along dimer rows lowers the effective activation energy,

diffusion parallel to the rows is faster, particularly at low temperature.

The diffusion mechanism for the Au adatom on the Si(100)-2 × 1 surface identified here is similar in many respects to the diffusion mechanism of a Si adatom on this surface, in that an indirect diffusion mechanism involving repeated hops along of the top of a dimer row rows turn out to be more efficient than a direct hopping mechanism between optimal binding sites, especially at low temperature [31]. This explained the experimental STM observations of the formation of Si ad-dimers on top of dimer rows even though dimers were expected to form in between dimer rows since those sites have a greater binding energy.

V. CONCLUSION

The mechanism and rate of diffusion of a Au adatom on the reconstructed Si(100)-2 × 1 surface has been calculated using the CI-NEB method for identifying optimal diffusion paths with energy and atomic forces estimated from DFT/PBEsol. While the most stable binding site is found to be in between dimer rows, in agreement with previous theoretical calculations and STM experimental measurements [16,17], the dominant diffusion mechanism is found to involve promotion of the adatom into metastable sites on top of a dimer row and multiple hops along the row, before the adatom settles down again into an optimal binding site between dimer rows. This indirect diffusion mechanism becomes more dominant the lower is the temperature. At room temperature the adatom is predicted to skid along a dimer row covering distances on the order of 300 Å in between visits to optimal binding sites.

In addition to the optimal binding site in between dimer rows, an additional local minimum, BDR2, is found where the Au adatom is 1 Å closer to the surface but this site corresponds to higher energy by 0.5 eV. Also, a weak binding site on top of a Si dimer, the TDR3 site, has been identified as an intermediate minimum in the CI-NEB calculation on the minimum energy path between adjacent TDR2 sites. The Au adatom can also split a Si dimer in order to pass through it during the transition between TDR2 sites, but the energy barrier is 0.57 eV so this process is less likely than a hop over the Si dimer.

Simulations of diffusion paths over a range of temperature using the KMC method reveal the relative importance of the indirect and direct diffusion paths and are used to estimate the diffusion coefficient. From the temperature dependence of the diffusion coefficient an effective activation energy of 0.52 eV is obtained, significantly lower than the activation energy for the direct diffusion mechanism, 0.84 eV. The indirect diffusion mechanism can have significant consequences for the formation of dimers and larger Au islands on the surface. Since the adatoms travel long distances on top of dimer rows, the most probable site for the formation of a Au ad-dimer is on top of a dimer row, rather than in between dimer rows as one would predict from the location of the optimal binding sites.

ACKNOWLEDGMENTS

This project was funded by European Union's Horizon 2020 research and innovation programme under Grant Agreement No. 814416, and the Icelandic Research Fund. We thank Adam Foster for helpful discussions. The calculations were carried out at the Icelandic Research High Performance Computing (IRHPC) facility.

[1] X. Zhang, Y. L. Chen, R.-S. Liu, and D. P. Tsai, Plasmonic photocatalysis, Rep. Prog. Phys. **76**, 046401 (2013).
[2] S. Link and M. A. El-Sayed, Shape and size dependence of radiative, non-radiative and photothermal properties of gold nanocrystals, Int. Rev. Phys. Chem. **19**, 409 (2000).
[3] E. Roduner, Size matters: Why nanomaterials are different, Chem. Soc. Rev. **35**, 583 (2006).
[4] S. Bhaviripudi, E. Mile, S. A. Steiner, A. T. Zare, M. S. Dresselhaus, A. M. Belcher, and J. Kong, CVD synthesis of single-walled carbon nanotubes from gold nanoparticle catalysts, J. Am. Chem. Soc. **129**, 1516 (2007).
[5] J. Hannon, S. Kodambaka, F. Ross, and R. Tromp, The influence of the surface migration of gold on the growth of silicon nanowires, Nature (London) **440**, 69 (2006).
[6] H. Minoda and N. Yamamoto, Anomalous enhancement of light emission by Au adsorption on a Si(001) vicinal surface, J. Phys. Soc. Jpn. **74**, 1914 (2005).
[7] W. H. Choi, P. G. Kang, K. D. Ryang, and H. W. Yeom, Band-Structure Engineering of Gold Atomic Wires on Silicon by Controlled Doping, Phys. Rev. Lett. **100**, 126801 (2008).
[8] G. Leclerc, L. Paquin, and F. Baratay, Nonlinear silicon oxide growth patterns in a gold-silicon system, J. Mater. Res. **7**, 2458 (1992).
[9] S. Cheng and H. Chen, Effects of a thin Au interlayer on the formation of low-resistivity $CoSi_2$ on (001) Si substrate, Thin Solid Films **516**, 8797 (2008).
[10] E. H. Do, S. G. Kwon, M. H. Kang, and H. W. Yeom, Structural and electronic effects of adatoms on metallic atomic chains in Si(111)5 × 2-Au, Sci. Rep. **8**, 15537 (2018).
[11] C. Braun, C. Hogan, S. Chandola, N. Esser, S. Sanna, and W. G. Schmidt, Si(775)-Au atomic chains: Geometry, optical properties, and spin order, Phys. Rev. Materials **1**, 055002 (2017).
[12] C. Braun, S. Neufeld, U. Gerstmann, S. Sanna, J. Plaickner, E. Speiser, N. Esser, and W. G. Schmidt, Vibration-Driven Self-Doping of Dangling-Bond Wires on Si(553)-Au Surfaces, Phys. Rev. Lett. **124**, 146802 (2020).
[13] K. Kim, Y. Kim, N. Park, W. Cho, D. Choi, S. Kim, and C. Whang, Growth mode of Au layer on Si(001), Nucl. Instrum. Methods Phys. Res., Sect. B **117**, 289 (1996).
[14] E. Piscopiello, L. Tapfer, M. V. Antisari, P. Paiano, P. Prete, and N. Lovergine, Formation of epitaxial gold nanoislands on (100) silicon, Phys. Rev. B **78**, 035305 (2008).
[15] M. Wölz, Y-L. Huang, M. Seibt, and S. C. Erwin, Epitaxial growth of gold on Si(001), Surf. Sci. **624**, 15 (2014).
[16] F. Chiaravalloti, D. Riedel, G. Dujardin, H. Pinto, and A. S. Foster, STM topography and manipulation of single Au atoms on Si(100), Phys. Rev. B **79**, 245431 (2009).

[17] W. W. Ju, T. W. Li, J. H. You, Z. X. Tang, X. Y. Gong, H. Wang, Z. Q. Zhen, and Q. G. Zhang, Ab-initio study on adsorption and diffusion of Au atoms on clean Si (001) and H-Si(001) surface, Key Eng. Mater. **368-372**, 1699 (2008).

[18] G. Henkelman, B. P. Uberuaga, and H. Jónsson, A climbing image nudged elastic band method for finding saddle points and minimum energy paths, J. Chem. Phys. **113**, 9901 (2000).

[19] G. Henkelman and H. Jónsson, Improved tangent estimate in the nudged elastic band method for finding minimum energy paths and saddle points, J. Chem. Phys. **113**, 9978 (2000).

[20] V. Ásgeirsson and H. Jónsson, Exploring potential energy surfaces with saddle point searches, in *Handbook of Materials Modeling: Methods: Theory and Modeling*, edited by W. Andreoni and S. Yip (Springer, Cham, 2020), pp. 689–714.

[21] S. Smidstrup, A. Pedersen, K. Stokbro, and H. Jónsson, Improved initial guess for minimum energy path calculations, J. Chem. Phys. **140**, 214106 (2014).

[22] J. P. Perdew, A. Ruzsinszky, G. I. Csonka, O. A. Vydrov, G. E. Scuseria, L. A. Constantin, X. Zhou, and K. Burke, Restoring the Density-Gradient Expansion for Exchange in Solids and Surfaces, Phys. Rev. Lett. **100**, 136406 (2008).

[23] P. E. Blöchl, Projector augmented-wave method, Phys. Rev. B **50**, 17953 (1994).

[24] S. T. Chill, M. Welborn, R. Terrell, L. Zhang, J-C. Berthet, A. Pedersen, H. Jónsson, and G. Henkelman, EON: Software for long time simulations of atomic scale systems, Modell. Simul. Mater. Sci. Eng. **22**, 055002 (2014).

[25] G. Kresse and J. Hafner, *Ab initio* molecular dynamics for liquid metals, Phys. Rev. B **47**, 558(R) (1993); *Ab initio* molecular-dynamics simulation of the liquid-metal-amorphous-semiconductor transition in germanium, *ibid.* **49**, 14251 (1994); G. Kresse and J. Furthmüller, Efficiency of ab-initio total energy calculations for metals and semiconductors using a plane-wave basis set, Comput. Mater. Sci. **6**, 15 (1996); Efficient iterative schemes for *ab initio* total-energy calculations using a plane-wave basis set, Phys. Rev. B **54**, 11169 (1996).

[26] M. Stamatakis and D. G. Vlachos, A graph-theoretical kinetic Monte Carlo framework for on-lattice chemical kinetics, J. Chem. Phys. **134**, 214115 (2011).

[27] J. Nielsen, M. d'Avezac, J. Hetherington, and M. Stamatakis, Parallel kinetic Monte Carlo simulation framework incorporating accurate models of adsorbate lateral interactions, J. Chem. Phys. **139**, 224706 (2013).

[28] R. A. Wolkow, Direct Observation of an Increase in Buckled Dimers on Si(001) at Low Temperature, Phys. Rev. Lett. **68**, 2636 (1992).

[29] C.-S. Guo, K. Hermann, and Y. Zhao, Dynamics and energetics of reconstruction at the Si(100) surface, J. Phys. Chem. C **118**, 25614 (2014)

[30] H. Over, J. Wasserfall, W. Ranke, C. Ambiatello, R. Sawitzki, D. Wolf, and W. Moritz, Surface atomic geometry of Si(001)-2×1: A low-energy electron diffraction structure analysis, Phys. Rev. B **55**, 4731 (1997).

[31] A. P. Smith and H. Jónsson, Dimer and String Formation during Low Temperature Silicon Deposition on Si(100), Phys. Rev. Lett. **77**, 1326 (1996).

References

Akira, Y., Yasumasa, T., and Katsumichi, Y. (1992). Surface electromigration of au on si (001) studied by rem. *Surface science*, 264(1-2):55–64.

An, K. and Somorjai, G. A. (2012). Size and shape control of metal nanoparticles for reaction selectivity in catalysis. *ChemCatChem*, 4(10):1512–1524.

Atwater, H. A. and Polman, A. (2011). Plasmonics for improved photovoltaic devices. *Materials for sustainable energy: A collection of peer-reviewed research and review articles from nature publishing group*, pages 1–11.

Bartók, A. P. and Csányi, G. (2016). Erratum: Gaussian approximation potentials: A brief tutorial introduction. *International Journal of Quantum Chemistry*, 116(13):1049–1049.

Bartók, A. P., Kondor, R., and Csányi, G. (2017). Erratum: on representing chemical environments [phys. rev. b 87, 184115 (2013)]. *Physical Review B*, 96(1):019902.

Bartók, A. P., Payne, M. C., Kondor, R., and Csányi, G. (2010). Gaussian approximation potentials: The accuracy of quantum mechanics, without the electrons. *Physical review letters*, 104(13):136403.

Bassett, D. (1976). Migration of platinum adatom clusters on tungsten (110) surfaces. *Journal of Physics C: Solid State Physics*, 9(13):2491.

Bassett, D. and Parsley, M. (1969). The effect of an electric field on the surface diffusion of rhenium adsorbed on tungsten. *Journal of Physics D: Applied Physics*, 2(1):13.

Bassett, D. and Webber, P. (1978). Diffusion of single adatoms of platinum, iridium and gold on platinum surfaces. *Surface Science*, 70(1):520–531.

Berne, B. J., Ciccotti, G., and Coker, D. F. (1998). *Classical and quantum dynamics in condensed phase simulations: Proceedings of the International School of Physics*. World Scientific.

Bhaviripudi, S., Mile, E., Steiner, S. A., Zare, A. T., Dresselhaus, M. S., Belcher, A. M., and Kong, J. (2007). Cvd synthesis of single-walled carbon nanotubes from gold nanoparticle catalysts. *Journal of the American Chemical Society*, 129(6):1516–1517.

Bilalbegović, G., Ercolessi, F., and Tosatti, E. (1993). High-temperature morphology of stepped gold surfaces. *Surface science*, 280(3):335–348.

Blöchl, P. E. (1994). Projector augmented-wave method. *Physical review B*, 50(24):17953.

Bortz, A. B., Kalos, M. H., and Lebowitz, J. L. (1975). A new algorithm for monte carlo simulation of ising spin systems. *Journal of Computational Physics*, 17(1):10–18.

Bozzola, J. J. and Russell, L. D. (1999). *Electron microscopy: principles and techniques for biologists*. Jones & Bartlett Learning.

Bratlie, K. M., Lee, H., Komvopoulos, K., Yang, P., and Somorjai, G. A. (2007). Platinum nanoparticle shape effects on benzene hydrogenation selectivity. *Nano letters*, 7(10):3097–3101.

Breuer, K. S. (2005). *Microscale diagnostic techniques*. Springer.

Brune, H. (1998). Microscopic view of epitaxial metal growth: nucleation and aggregation. *Surface Science Reports*, 31(4-6):125–229.

Caro, M. A. (2019). Optimizing many-body atomic descriptors for enhanced computational performance of machine learning based interatomic potentials. *Physical Review B*, 100(2):024112.

Chen, H., Shao, L., Li, Q., and Wang, J. (2013). Gold nanorods and their plasmonic properties. *Chemical Society Reviews*, 42(7):2679–2724.

Cheng, S. and Chen, H. (2008). Effects of a thin au interlayer on the formation of low-resistivity cosi2 on (001) si substrate. *Thin solid films*, 516(23):8797–8803.

Cheong, S., Watt, J. D., and Tilley, R. D. (2010). Shape control of platinum and palladium nanoparticles for catalysis. *Nanoscale*, 2(10):2045–2053.

Chiaravalloti, F., Riedel, D., Dujardin, G., Pinto, H., and Foster, A. S. (2009). Stm topography and manipulation of single au atoms on si (100). *Physical Review B*, 79(24):245431.

Chill, S. T., Welborn, M., Terrell, R., Zhang, L., Berthet, J.-C., Pedersen, A., Jonsson, H., and Henkelman, G. (2014). Eon: software for long time simulations of atomic scale systems. *Modelling and Simulation in Materials Science and Engineering*, 22(5):055002.

Choi, J.-r., Oh, S. J., Ju, H., and Cheon, J. (2005). Massive fabrication of free-standing one-dimensional co/pt nanostructures and modulation of ferromagnetism via a programmable barcode layer effect. *Nano letters*, 5(11):2179–2183.

Choi, W. H., Kang, P. G., Ryang, K. D., and Yeom, H. W. (2008). Band-structure engineering of gold atomic wires on silicon by controlled doping. *Physical review letters*, 100(12):126801.

Daw, M. S. and Baskes, M. I. (1984). Embedded-atom method: Derivation and application to impurities, surfaces, and other defects in metals. *Physical Review B*, 29(12):6443.

Deringer, V. L., Bartók, A. P., Bernstein, N., Wilkins, D. M., Ceriotti, M., and Csányi, G. (2021). Gaussian process regression for materials and molecules. *Chemical Reviews*.

Deringer, V. L., Caro, M. A., and Csányi, G. (2019). Machine learning interatomic potentials as emerging tools for materials science. *Advanced Materials*, 31(46):1902765.

Desjonqueres, M.-C. and Spanjaard, D. (1996). *Concepts in Surface Physics: 2eme édition*, volume 30. Springer Science & Business Media.

Durán, N. and Marcato, P. D. (2012). Biotechnological routes to metallic nanoparticles production: mechanistic aspects, antimicrobial activity, toxicity and industrial applications. In *Nano-antimicrobials*, pages 337–374. Springer.

Ehrlich, G. and Hudda, F. G. (1966). Atomic view of surface self-diffusion: tungsten on tungsten. *The Journal of Chemical Physics*, 44(3):1039–1049.

Feibelman, P. J. (1998). Interlayer self-diffusion on stepped pt (111). *Physical review letters*, 81(1):168.

Feibelman, P. J. (1999). Self-diffusion along step bottoms on pt (111). *Physical Review B*, 60(7):4972.

Finnis, M. and Sinclair, J. (1984). A simple empirical n-body potential for transition metals. *Philosophical Magazine A*, 50(1):45–55.

Gillespie, D. T. (1976). A general method for numerically simulating the stochastic time evolution of coupled chemical reactions. *Journal of computational physics*,

22(4):403–434.

Graham, W. R. and Ehrlich, G. (1975). Surface self-diffusion of single atoms. *Thin Solid Films*, 25(1):85–96.

Gubin, S. P. (2009). *Magnetic nanoparticles*. John Wiley & Sons.

Guimarães, A. P. and Guimaraes, A. P. (2009). *Principles of nanomagnetism*, volume 7. Springer.

Haes, A. J. and Van Duyne, R. P. (2004). A unified view of propagating and localized surface plasmon resonance biosensors. *Analytical and bioanalytical chemistry*, 379(7):920–930.

Hafner, J. and Kresse, G. (1997). The vienna ab-initio simulation program vasp: An efficient and versatile tool for studying the structural, dynamic, and electronic properties of materials. In *Properties of Complex Inorganic Solids*, pages 69–82. Springer.

Hannon, a. J., Kodambaka, S., Ross, F., and Tromp, R. (2006). The influence of the surface migration of gold on the growth of silicon nanowires. *nature*, 440(7080):69–71.

Hansen, E. W. and Neurock, M. (2000). First-principles-based monte carlo simulation of ethylene hydrogenation kinetics on pd. *Journal of Catalysis*, 196(2):241–252.

Hansen, L., Stoltze, P., Jacobsen, K. W., and Nørskov, J. K. (1991). Self-diffusion on copper surfaces. *Physical Review B*, 44(12):6523.

Haruta, M. (2005). Gold rush. *Nature*, 437(7062):1098–1099.

Haruta, M., Yamada, N., Kobayashi, T., and Iijima, S. (1989). Gold catalysts prepared by coprecipitation for low-temperature oxidation of hydrogen and of carbon monoxide. *Journal of catalysis*, 115(2):301–309.

Haugstad, G. (2012). *Atomic force microscopy: understanding basic modes and advanced applications*. John Wiley & Sons.

Hawkes, P. (2003). Electron optics and electron microscopy: conference proceedings and abstracts as source material. *Advances in Imaging and Electron Physics*, 127:207–379.

Henkelman, G. and Jónsson, H. (1999). A dimer method for finding saddle points on high dimensional potential surfaces using only first derivatives. *The Journal of chemical physics*, 111(15):7010–7022.

Henkelman, G. and Jónsson, H. (2000). Improved tangent estimate in the nudged elastic band method for finding minimum energy paths and saddle points. *The Journal of chemical physics*, 113(22):9978–9985.

Henkelman, G. and Jónsson, H. (2001). Long time scale kinetic monte carlo simulations without lattice approximation and predefined event table. *The Journal of Chemical Physics*, 115(21):9657–9666.

Henkelman, G. and Jónsson, H. (2003). Multiple time scale simulations of metal crystal growth reveal the importance of multiatom surface processes. *Physical Review Letters*, 90(11):116101.

Henkelman, G., Uberuaga, B. P., and Jónsson, H. (2000). A climbing image nudged elastic band method for finding saddle points and minimum energy paths. *The Journal of chemical physics*, 113(22):9901–9904.

Heyden, A., Bell, A. T., and Keil, F. J. (2005). Efficient methods for finding transition states in chemical reactions: Comparison of improved dimer method and

partitioned rational function optimization method. *The Journal of chemical physics*, 123(22):224101.

Hofmann, S. (2012). *Auger-and X-ray photoelectron spectroscopy in materials science: a user-oriented guide*, volume 49. Springer Science & Business Media.

Hohenberg, P. and Kohn, W. (1964). Density functional theory (dft). *Phys. Rev*, 136:B864.

Hosokawa, M., Nogi, K., Naito, M., and Yokoyama, T. (2012). Structural control of nanoparticles. *Nanoparticle Technology Handbook (Second Edition). Elsevier, Amsterdam*, pages 51–112.

Jacobsen, J., Jacobsen, K., and Stoltze, P. (1994). Nucleation of the pt (111) reconstruction: a simulation study. *Surface science*, 317(1-2):8–14.

Jacobsen, K., Norskov, J., and Puska, M. J. (1987). Interatomic interactions in the effective-medium theory. *Physical Review B*, 35(14):7423.

Jonsson, H. (2000). Theoretical studies of atomic-scale processes relevant to crystal growth. *Annual review of physical chemistry*, 51(1):623–653.

Jónsson, H., Mills, G., and Jacobsen, K. W. (1998). Nudged elastic band method for finding minimum energy paths of transitions.

Ju, W. W., Li, T. W., You, J. H., Tang, Z. X., Gong, X. Y., Wang, H., Zhen, Z. Q., and Zhang, Q. G. (2008). Ab-initio study on adsorption and diffusion of au atoms on clean si (001) and h-si (001) surface. In *Key Engineering Materials*, volume 368, pages 1699–1701. Trans Tech Publ.

Jun, Y.-w., Choi, J.-s., and Cheon, J. (2007). Heterostructured magnetic nanoparticles: their versatility and high performance capabilities. *Chemical communications*, (12):1203–1214.

Jun, Y.-w., Seo, J.-w., and Cheon, J. (2008). Nanoscaling laws of magnetic nanoparticles and their applicabilities in biomedical sciences. *Accounts of chemical research*, 41(2):179–189.

Kästner, J. and Sherwood, P. (2008). Superlinearly converging dimer method for transition state search. *The Journal of chemical physics*, 128(1):014106.

Kelsall, R. W., Hamley, I. W., Geoghegan, M., et al. (2005). *Nanoscale science and technology*. Wiley Online Library.

Kim, K., Kim, Y., Park, N., Cho, W., Choi, D., Kim, S., and Whang, C. (1996). Growth mode of au layer on si (001). *Nuclear Instruments and Methods in Physics Research Section B: Beam Interactions with Materials and Atoms*, 117(3):289–294.

Kitagawa, H., Nakatani, A., Ogata, S., Saitoh, K.-I., and Maegawa, Y. (1997). Atomic diffusion near al grain boundary: Molecular dynamics analysis based on effective-medium theory. *JSME International Journal Series A Solid Mechanics and Material Engineering*, 40(3):203–210.

Kley, A., Ruggerone, P., and Scheffler, M. (1997). Novel diffusion mechanism on the gaas (001) surface: the role of adatom-dimer interaction. *Physical review letters*, 79(26):5278.

Kohn, W., Becke, A. D., and Parr, R. G. (1996). Density functional theory of electronic structure. *The Journal of Physical Chemistry*, 100(31):12974–12980.

Kresse, G. and Furthmüller, J. (1996). Efficient iterative schemes for ab initio total-energy calculations using a plane-wave basis set. *Physical review B*, 54(16):11169.

Kresse, G. and Joubert, D. (1999). From ultrasoft pseudopotentials to the projector

augmented-wave method. *Physical review b*, 59(3):1758.

Kunkel, R., Poelsema, B., Verheij, L. K., and Comsa, G. (1990). Reentrant layer-by-layer growth during molecular-beam epitaxy of metal-on-metal substrates. *Physical review letters*, 65(6):733.

Lannoo, M. and Friedel, P. (1991). Atomic and electronic structure of surfaces, springer series in surface sciences vol. 16.

Leclerc, G., Paquin, L., and Baratay, F. (1992). Nonlinear silicon oxide growth patterns in a gold-silicon system. *Journal of materials research*, 7(9):2458–2464.

Lewis, L. N. (1993). Chemical catalysis by colloids and clusters. *Chemical Reviews*, 93(8):2693–2730.

Li, Y. and Somorjai, G. A. (2010). Nanoscale advances in catalysis and energy applications. *Nano letters*, 10(7):2289–2295.

Link, S. and El-Sayed, M. A. (2000). Shape and size dependence of radiative, non-radiative and photothermal properties of gold nanocrystals. *International reviews in physical chemistry*, 19(3):409–453.

Liu, C., Cohen, J., Adams, J., and Voter, A. (1991). Eam study of surface self-diffusion of single adatoms of fcc metals ni, cu, al, ag, au, pd, and pt. *Surface science*, 253(1-3):334–344.

Lundgren, E., Stanka, B., Leonardelli, G., Schmid, M., and Varga, P. (1999). Interlayer diffusion of adatoms: a scanning-tunneling microscopy study. *Physical review letters*, 82(25):5068.

Malek, R. and Mousseau, N. (2000). Dynamics of lennard-jones clusters: A characterization of the activation-relaxation technique. *Physical Review E*, 62(6):7723.

Marcus, R. (1966). On the analytical mechanics of chemical reactions. quantum mechanics of linear collisions. *The Journal of Chemical Physics*, 45(12):4493–4499.

Mills, G., Jónsson, H., and Schenter, G. K. (1995). Reversible work transition state theory: application to dissociative adsorption of hydrogen. *Surface Science*, 324(2-3):305–337.

Minoda, H. and Yamamoto, N. (2005). Anomalous enhancement of light emission by au adsorption on a si (001) vicinal surface. *Journal of the Physical Society of Japan*, 74(7):1914–1917.

Mo, Y.-W., Kleiner, J., Webb, M., and Lagally, M. (1992). Surface self-diffusion of si on si (001). *Surface science*, 268(1-3):275–295.

Mulvaney, P. (2001). Not all that's gold does glitter. *MRS bulletin*, 26(12):1009–1014.

Niu, W. and Lu, X. (2015). Metallic nanostructures: Fundamentals. In *Metallic Nanostructures*, pages 1–47. Springer.

Nocedal, J. (1980). Updating quasi-newton matrices with limited storage. *Mathematics of computation*, 35(151):773–782.

Olsen, R., Kroes, G., Henkelman, G., Arnaldsson, A., and Jónsson, H. (2004). Comparison of methods for finding saddle points without knowledge of the final states. *The Journal of chemical physics*, 121(20):9776–9792.

Park, J.-I. and Cheon, J. (2001). Synthesis of "solid solution" and "core-shell" type cobalt- platinum magnetic nanoparticles via transmetalation reactions. *Journal of the American Chemical Society*, 123(24):5743–5746.

Park, J.-I., Kang, N.-J., Jun, Y.-W., Oh, S. J., Ri, H.-C., and Cheon, J. (2002). Superlattice and magnetism directed by the size and shape of nanocrystals. *ChemPhysChem*,

3(6):543–547.

Park, J.-I., Kim, M. G., Jun, Y.-w., Lee, J. S., Lee, W.-r., and Cheon, J. (2004). Characterization of superparamagnetic "core- shell" nanoparticles and monitoring their anisotropic phase transition to ferromagnetic "solid solution" nanoalloys. *Journal of the American Chemical Society*, 126(29):9072–9078.

Perdew, J. P., Burke, K., and Ernzerhof, M. (1996). Generalized gradient approximation made simple. *Physical review letters*, 77(18):3865.

Perdew, J. P., Ruzsinszky, A., Csonka, G. I., Vydrov, O. A., Scuseria, G. E., Constantin, L. A., Zhou, X., and Burke, K. (2008). Restoring the density-gradient expansion for exchange in solids and surfaces. *Physical review letters*, 100(13):136406.

Pimpinelli, A. and Villain, J. (1999). *Physics of crystal growth*.

Plimpton, S. (1995). Fast parallel algorithms for short-range molecular dynamics. *Journal of computational physics*, 117(1):1–19.

Poelsema, B. and Comsa, G. (1989). *Springer tracts in modern physics*, volume 115. Springer-Verlag.

Quate, C., Gerber, C., and Binnig, C. (1986). Atomic force microscope. *Phys. Rev. Lett*, 56(9):930–933.

Reimer, L. (2000). Scanning electron microscopy: physics of image formation and microanalysis.

Rietig, A., Langner, T., and Acker, J. (2020). Advanced insights into the stoichiometry and kinetics of the reaction of silicon in hf/hno3 and hf/hno3/h2sif6 mixtures. *SILICON FOR THE CHEMICAL AND SOLAR INDUSTRY XV*, 4:145.

Roduner, E. (2006). Size matters: why nanomaterials are different. *Chemical Society Reviews*, 35(7):583–592.

Rohra, S. (2006). Exact-exchange kohn-sham spin-current density-functional theory.

Rose, J. H., Ferrante, J., and Smith, J. R. (1981). Universal binding energy curves for metals and bimetallic interfaces. *Physical Review Letters*, 47(9):675.

Saravanan, R. and Rani, M. P. (2012). Charge density analysis from x-ray diffraction. In *Metal and Alloy Bonding-An Experimental Analysis*, pages 31–64. Springer.

Schmidt, B. and Wetzig, K. (2012). Ion beams in materials processing and analysis.

Schwoebel, R. L. and Shipsey, E. J. (1966). Step motion on crystal surfaces. *Journal of Applied Physics*, 37(10):3682–3686.

Sepúlveda, B., Angelomé, P. C., Lechuga, L. M., and Liz-Marzán, L. M. (2009). Lspr-based nanobiosensors. *nano today*, 4(3):244–251.

Sharma, S. K. (2004). *Atomic and nuclear physics*. Pearson Education India.

Sholl, D. and Steckel, J. A. (2011). *Density functional theory: a practical introduction*. John Wiley & Sons.

Singh, S. C., Zeng, H., Guo, C., and Cai, W. (2012). *Nanomaterials: processing and characterization with lasers*. John Wiley & Sons.

Starikov, S., Gordeev, I., Lysogorskiy, Y., Kolotova, L., and Makarov, S. (2020). Optimized interatomic potential for study of structure and phase transitions in si-au and si-al systems. *Computational Materials Science*, 184:109891.

Starikov, S., Lopanitsyna, N. Y., Smirnova, D., and Makarov, S. (2018). Atomistic simulation of si-au melt crystallization with novel interatomic potential. *Computational Materials Science*, 142:303–311.

Stillinger, F. H. and Weber, T. A. (1985). Computer simulation of local order in

condensed phases of silicon. *Physical review B*, 31(8):5262.

Stoltze, P. (1994). Simulation of surface defects. *Journal of Physics: Condensed Matter*, 6(45):9495.

Tersoff, J. (1988). New empirical approach for the structure and energy of covalent systems. *Physical review B*, 37(12):6991.

Tian, N., Zhou, Z.-Y., and Sun, S.-G. (2008). Platinum metal catalysts of high-index surfaces: from single-crystal planes to electrochemically shape-controlled nanoparticles. *The Journal of Physical Chemistry C*, 112(50):19801–19817.

Tian, N., Zhou, Z.-Y., Sun, S.-G., Ding, Y., and Wang, Z. L. (2007). Synthesis of tetrahexahedral platinum nanocrystals with high-index facets and high electro-oxidation activity. *science*, 316(5825):732–735.

Tong, X. C. (2011). *Advanced materials for thermal management of electronic packaging*, volume 30. Springer Science & Business Media.

Tsong, T., Cowan, P., and Kellogg, G. (1975). Atomic view of surface diffusion with and without a driving force, and atomic interactions. *Thin Solid Films*, 25(1):97–106.

Tsong, T. and Kellogg, G. (1975). Direct observation of the directional walk of single adatoms and the adatom polarizability. *Physical Review B*, 12(4):1343.

Tung, R. T. and Graham, W. R. (1980). Single atom self-diffusion on nickel surfaces. *Surface Science*, 97(1):73–87.

Ueno, K. and Misawa, H. (2013). Surface plasmon-enhanced photochemical reactions. *Journal of Photochemistry and Photobiology C: Photochemistry Reviews*, 15:31–52.

Vajtai, R. (2013). *Springer handbook of nanomaterials*. Springer Science & Business Media.

Van Hove, J., Lent, C., Pukite, P., and Cohen, P. (1983). Damped oscillations in reflection high energy electron diffraction during gaas mbe. *Journal of Vacuum Science & Technology B: Microelectronics Processing and Phenomena*, 1(3):741–746.

Villarba, M. and Jónsson, H. (1994). Diffusion mechanisms relevant to metal crystal growth: Pt/pt (111). *Surface science*, 317(1-2):15–36.

Vineyard, G. (1960). Vacancies and other point defects in metals and alloys a symposium organized by the institute of metals and held at the atomic energy research establishment, harwell, 10 december, 1957. the institute of metals, london, 1958. 238pp., 40s., 6.00. *Journal of Physics and Chemistry of Solids*, 16(1-2):164.

Vineyard, G. H. (1957). Frequency factors and isotope effects in solid state rate processes. *Journal of Physics and Chemistry of Solids*, 3(1-2):121–127.

Voter, A. and Chen, S. (1987). Computer simulation of grain boundaries in ni3al: the effect of grain boundary composition. In *Mat. Res. Soc. Symp. Proc.*, volume 82, pages 175–175.

Voter, A. F. (1986). Classically exact overlayer dynamics: Diffusion of rhodium clusters on rh (100). *Physical review B*, 34(10):6819.

Wang, S. and Ehrlich, G. (1989). Self-adsorption sites on a close-packed surface: Ir on ir (111). *Physical review letters*, 62(19):2297.

Wang, S. and Ehrlich, G. (1990). Structure, stability, and surface diffusion of clusters: Irx on ir (111). *Surface science*, 239(3):301–332.

Wang, S. and Ehrlich, G. (1991). Atom incorporation at surface clusters: An atomic view. *Physical review letters*, 67(18):2509.

Wert, C. and Zener, C. (1949). Interstitial atomic diffusion coefficients. *Physical Review*,

76(8):1169.

Willets, K. A. and Van Duyne, R. P. (2007). Localized surface plasmon resonance spectroscopy and sensing. *Annu. Rev. Phys. Chem.*, 58:267–297.

Williams, D. B. and Carter, C. B. (1996). The transmission electron microscope. In *Transmission electron microscopy*, pages 3–17. Springer.

Wolf, J., Vicenzi, B., and Ibach, H. (1991). Step roughness on vicinal ag (111). *Surface science*, 249(1-3):233–236.

Wu, J., Li, P., Pan, Y.-T. F., Warren, S., Yin, X., and Yang, H. (2012). Surface lattice-engineered bimetallic nanoparticles and their catalytic properties. *Chemical Society Reviews*, 41(24):8066–8074.

Xiong, Y., Wiley, B. J., and Xia, Y. (2007). Nanocrystals with unconventional shapes—a class of promising catalysts. *Angewandte Chemie International Edition*, 46(38):7157–7159.

Xu, L. and Henkelman, G. (2008). Adaptive kinetic monte carlo for first-principles accelerated dynamics. *The Journal of chemical physics*, 129(11):114104.

Yang, L. and DePristo, A. E. (1994). On the factors determining the isomers of metal clusters. *The Journal of chemical physics*, 100(1):725–728.

Zaera, F. (2013). Shape-controlled nanostructures in heterogeneous catalysis. *ChemSusChem*, 6(10):1797–1820.

Zhang, X., Chen, Y. L., Liu, R.-S., and Tsai, D. P. (2013). Plasmonic photocatalysis. *Reports on Progress in Physics*, 76(4):046401.

Zhao, J., Zhang, X., Yonzon, C. R., Haes, A. J., and Van Duyne, R. P. (2006). Localized surface plasmon resonance biosensors.

Zhou, Z.-Y., Tian, N., Huang, Z.-Z., Chen, D.-J., and Sun, S.-G. (2009). Nanoparticle catalysts with high energy surfaces and enhanced activity synthesized by electrochemical method. *Faraday discussions*, 140:81–92.

Zweben, C. (1998). Advances in composite materials for thermal management in electronic packaging. *Jom*, 50(6):47–51.